CZECH TECHNICAL UNIVERSITY IN PRAGUE

Faculty of Nuclear Sciences and Physical Engineering

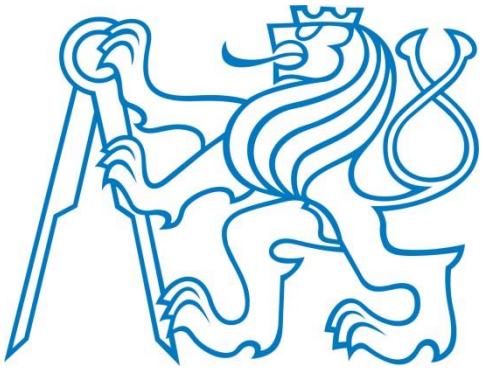

DISSERTATION

Biofunctionalization of luminescent nanocomposites

Prague, 2020 **Ing. Kseniya Popovich**

Declaration of authorship

I hereby declare that the thesis I am submitting is entirely my own original work and has been generated by me as the result of my own original research except otherwise indicated in the text. I played a major role in the preparation and execution of the experiments, and the data analysis and interpretation are entirely my own work. Any contributions, such as measured data and diagrams, from colleagues in the collaboration or from students under my direct supervision and guidance are explicitly referenced in the text. All direct and indirect sources used are acknowledged as references.

In Prague, ……. ……..

Ing. Kseniya Popovich

Acknowledgement

I would like to thank to thesis supervisor, doc. Ing. Václav Čuba, Ph.D., for his support and guidance during my study and research.

I would also like to express my thanks to my colleagues from the Department of Nuclear Chemistry (Ing. Jan Bárta, PhD., Ing. Lenka Procházková, PhD., Ing. Michaela Škodová, PhD., Ing. Kateřina Tomanová, Ing. Barbora Neužilová, Ing. Iveta Terezie Pelikánová) for their constant help, support and pleasant working environment.

The completion of this dissertation could not have been possible without the participation and assistance of external laboratories. I am extremely thankful to doc. RNDr. Eva Mihóková, CSc., doc. Ing. Martin Nikl, CSc. and Ing. Vítězslav Jarý, PhD. (Institute of Physics, AS CR) for their help with luminescence measurements and data analysis; to Ing. Ivo Jakubec, CSc. (Institute of Inorganic Chemistry, AS CR) for SEM/TEM measurements; to Ing. Filip Dominec, PhD. (Institute of Physics, AS CR) and Mgr. Ondřej Lalinský (Institute of Scientific Instruments, AS CR) for cathodoluminescence imaging; to Ing. Libor Kobera, PhD. (Institute of the Macromolecular Chemistry, AS CR) for ss-NMR measurements; to Ing. Karel Klepárník, CSc. and Ing. Vojtěch Ledvina (Institute of Analytical Chemistry, AS CR) for their collaboration in development of the nanocomposite for bioimaging.

I am also obliged to acknowledge students (Michaela Šípková and Bc. Jindřich Fleišmann) for their outstanding results and benefits to this work.

Last but not the least, I would like to thank my family for their constant source of motivation and support for me.

This work was supported in part by the Czech Science Foundation under projects No. GA17-06479S and No. GA20-06374S; in part by the Grant Agency of the Czech Technical University in Prague under grants No. SGS17/195/OHK4/3T14 and No. SGS20/185/OHK4/3T/14; and in part by the Ministry of Education Youth and Sports under grant No. CZ.02.1.01/0.0/0.0/16_019/0000778.

Bibliografický záznam

Autorka	Ing. Kseniya Popovich České vysoké učení technické v Praze, Fakulta jaderná a fyzikálně inženýrská, Katedra jaderné chemie
Název práce	Biofunkcionalizace luminiscenčních nanokompozitů
Studijní program	Aplikace přírodních věd
Studijní obor	Jaderná chemie
Školitel	doc. Ing. Václav Čuba, Ph.D. České vysoké učení technické v Praze, Fakulta jaderná a fyzikálně inženýrská, Katedra jaderné chemie
Akademický rok	2019/2020
Počet stran	102
Klíčová slova	katodoluminiscence, biofunkcionalizace, biozobrazování, nanokompozit, nanočástice, PDTX, sol-gel, rentgenové záření

Bibliographic Entry

Author	Ing. Kseniya Popovich Czech Technical University in Prague, Faculty of Nuclear Sciences and Physical Engineering, Department of Nuclear Chemistry
Title of Dissertation	Biofunctionalization of Luminescent Nanocomposites
Degree Programme	Application of Natural Sciences
Field of Study	Nuclear Chemistry
Supervisor	doc. Ing. Václav Čuba, Ph.D. Czech Technical University in Prague, Faculty of Nuclear Sciences and Physical Engineering, Department of Nuclear Chemistry
Academic Year	2019/2020
Number of Pages	102
Keywords	cathodoluminescence, biofunctionalization, bioimaging, nanocomposite, nanoparticle, PDTX, sol-gel, X-ray

Abstrakt

Hlavními cíli práce byl návrh struktury, syntéza a stanovení vlastností multimodálních luminiscenčních nanokompozitních materiálů. Luminiscenční nanokompozitní materiály obsahují scintilující jádro, které bylo připravené buď fotoindukovanou metodou nebo technikou sol-gel. Jádro je obaleno amorfní vrstvou oxidu křemičitého pro zvýšení reaktivity povrchu nanočástic a následně konjugované s biomolekulou v závislosti na modalitě nanokompozitu. Protoporfyrin IX byl navázán pro aplikace v rentgenem buzené fotodynamické terapii (PDTX), protilátka anti-FasL byla zvolena pro použití nanokompozitního materiálu pro katodoluminiscenční biozobrazování. Byl testován koncept zajištění biokompatibility připravených materiálů pomocí konjugace molekul polyethylenglykolu (PEG) na povrch nanokompozitu.

Výsledky měření luminiscenčních spektrálních charakteristik nanokompozitu LuAG:Pr^{3+}@SiO_2-PpIX ukazují, že dochází k radiačnímu přenosu energie z jádra LuAG:Pr^{3+} na vnější vrstvu protoporfyrinu IX, což je nezbytnou podmínkou pro generování singletního kyslíku v PDTX. Produkce singletního kyslíku byla monitorována pomocí měření fotoluminiscenčních emisních spekter s přídavkem chemické sondy APF citlivé na přítomnost $^1O_2$ a NaN_3 jako inhibitoru OH radikálů.

Byl testován koncept využitelnosti luminiscenčních nanokompozitních materiálů pro biozobrazování v katodoluminiscenčním svazku. Katodoluminiscenční biozobrazování bylo testováno na kvasinkách *Sacharomyces cerevisiae* a na leukocytech. Bylo zjištěno, že luminiscenční nanomateriály jsou schopné se navázat na buněčnou membránu buď pomocí sorpce (nanočástice LuAG:Ce^{3+}), nebo cílením (nanokompozit LuAG:Ce^{3+}@SiO_2-anti-FasL) na transmembránový protein. Připravený nanokompozit navíc vykazuje dobrou stabilitu po excitaci 10 keV elektronovým svazkem.

Abstract

The main aims of this work were the design of the structure, synthesis, and evaluation of properties of multimodal luminescent nanocomposite materials. Luminescent nanocomposite materials consist of a scintillating core, which was prepared either by photo-induced method or by sol-gel technique. The core is coated with an amorphous silica layer and subsequently conjugated with a biomolecule, which was chosen depending on the modality of the nanocomposite. Protoporphyrin IX was bound for application in X-ray induced photodynamic therapy (PDTX), and anti-FasL antibody was chosen for application of the nanocomposite material in cathodoluminescence bioimaging. The concept of biocompatibilization of the prepared materials by conjugation with polyethylene glycol (PEG) molecules was also tested.

The results of the luminescence spectral characteristics measurements of the LuAG:Pr^{3+}@SiO_2-PpIX nanocomposite show existence of radiative energy transfer from the LuAG:Pr^{3+} core to PpIX outer layer, which is a necessary condition for singlet oxygen generation in PDTX. Production of singlet oxygen was monitored by measuring of photoluminescence emission spectra with addition of APF chemical probe, sensitive to $^1O_2$, and NaN_3, as an inhibitor of OH radicals.

Proof-of-concept of bioimaging in cathodoluminescence beam was developed. Cathodoluminescence bioimaging was tested on yeast cells *Saccharomyces cerevisiae* and leucocytes. It was found, that luminescent nanomaterials are able to attach to the cells via sorption (LuAG:Ce^{3+} nanoparticles) or by targeting (LuAG:Ce^{3+}@SiO_2-anti-FasL nanocomposite) trans-membrane protein. Moreover, the prepared nanocomposite shows stable luminescence under 10 keV electron irradiation.

List of Abbreviations

Ab	Antibody
Ag	Antigen
APF	Aminophenyl Fluorescein
APTES	(3-aminopropyl)triethoxy-silane
AS CR	Academy of Sciences of the Czech Republic
BET	Brunauer–Emmett–Teller equation
BSA	Bovine Serum Albumin
BSE	Backscattered Electrons
CL	Cathodoluminescence
CN	Coordination Number
CP	Cross-polarization
CTAB	Cetyltrimethylammonium bromide
DAPI	4',6-diamidino-2-phenylindole
DLS	Dynamic Light Scattering
DNA	Deoxyribonucleic acid
DSC	Differential Scanning Calorimetry
DTA	Differential Thermal Analysis
DTT	Dithiothreitol
EBSD	Electron Backscattered Diffraction
EDC	N-(3-dimethylamino-propyl)-N'-ethylcarbodiimide
EDS	Energy-dispersive X-Ray Spectroscopy
EPR	Enhanced Permeability and Retention
Fab	Fragment of antigen binding
FasL	anti-Fas ligand
Fc	Fragment crystallizable region
FRET	Förster Resonance Energy Transfer
FWHM	Full Width at Half of Maximum
ICDD	International Center for Diffraction Data
Ig	Immunoglobulin
IR	Infrared spectral region
ISC	Intersystem Crossing
LSO	Lutetium oxyorthosilicate, Lu_2SiO_5
LuAG	Lutetium-aluminum garnet, $Lu_3Al_5O_{12}$
LY	Light Yield
MAS	Magic-Angle Spinning
MEA	Mercaptoethylamine

MES	2-(N-morpholino)-ethanesulfonic acid
NP	Nanoparticle
PCL	Polycaprolactone
PDF-2	Powder Diffraction File structural database
PDT	Photodynamic Therapy
PDTX	X-ray induced photodynamic therapy
PDXL-2	X-ray powder diffraction analysis software
PEG	Polyethylene glycol
PEO	Polyethylene oxide
PL	Photoluminescence
PMMA	Polymethyl methacrylate
PMT	Photomultiplier
PpIX	Protoporphyrin IX
PS	Photosensitizer
PVA	Polyvinyl alcohol
PVT	Polyvinyl toluene
QY	Quantum Yield
RCF	Relative Centrifugal Force
RE	Rare-Earth element
RL	Radioluminescence
RNA	Ribonucleic acid
ROS	Reactive Oxygen Species
RPM	Revolutions per Minute
RT	Room Temperature
SAED	Selected Area Electron Diffraction
SE	Secondary Electrons
SEM	Scanning Electron Microscope
SOSG	Singlet Oxygen Sensor Green
ss-NMR	Solid-state Nuclear Magnetic Resonance
SSA	Specific Surface Area
sulfo-NHS	N-hydroxysulfosuccinimide
TAT	Transactivator of Transcription
TEM	Transmission Electron Microscope
TEOS	Tetraethyl orthosilicate
TG	Thermogravimetry
THF	Tetrahydrofuran
TSC	Trisodium citrate
UV	Ultraviolet spectral region
VIS	Visible spectral region
VUV	Vacuum-ultraviolet
XRD	X-ray Diffraction
YSO	yttrium oxyorthosilicate, Y_2SiO_5

Table of Contents

1. Introduction

Luminescent nanomaterials offer great opportunities for application in many fields, including microelectronics (Son et al., 2011), high energy physics (Sahi et al., 2018), environmental pollution prevention (Masciangioli and Zhang, 2003), or biotechnology and medicine (Salata, 2004). As shown in Fig. 1, for the recent fifteen years, increased attention has been focused on the development of multimodal drugs based on luminescent nanocomposites.

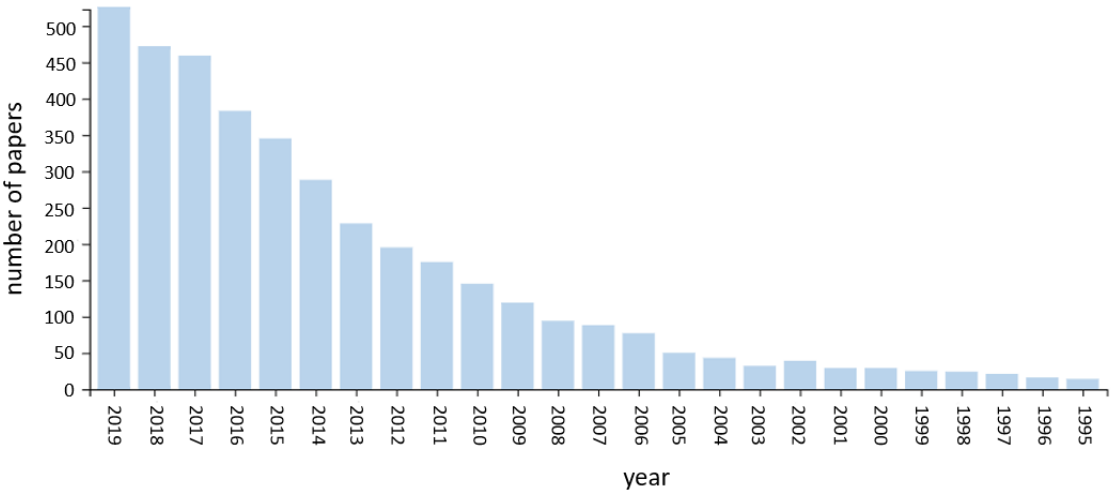

Fig. 1: Publications related to multimodal drugs per year since 1995.

Multimodal drug is an agent that combines different functions (modalities), which usually allows to provide e.g. simultaneous imaging, drug delivery and therapy. Multimodal drug may be presented in a form of a multilayered nanocomposite material, in which each layer carries out its own function. Multimodality of the nanocomposites is then determined by its chemical components. For example, application of the same nanocomposite for bioimaging, drug delivery or therapy is possible by replacement of conjugated biomolecules on its peripheral surface. The main idea behind development of the nanocomposite materials is to use building blocks with dimensions in nanometer range to create new materials with desired physical and chemical properties and with unprecedented flexibility for applications.

Synthesis of the nanocomposite materials capable to provide various modalities is generally a quite complicated process, which can be influenced by several factors. Firstly, it is rather difficult to predict physical and chemical behavior of the particles in nanoscale. Most of surface coating and biomolecules conjugation methods are usually

applicable for nanoparticles about units of nanometers in size. Secondly, the composition of such nanocomposite material is complex and consisting of a number of different organic and inorganic layers, bringing the challenge in design and chemical processing to link-up each subsequent layer with the layer beneath. In addition, luminescent intensity of the core nanoparticle must not be quenched after its surface functionalization. Another problem of the nanocomposites design is a proof of presence of chemical bonds between the constituent layers and occurrence of the physical processes, e.g. energy transfer required for X-ray induced photodynamic therapy (PDTX) drug. Methods for properties evaluation are not direct and include combination of several instrumental and analytical methods.

The main aims of this work include design, preparation, characterization and testing of the luminescent nanocomposites for different modalities, such as medical treatment (PDTX) and bioimaging (cathodoluminescence). Design and preparation of the luminescent nanocomposites consisted of synthesis of the luminescent nanoparticle core, such as rare-earth doped multicomponent garnet (lutetium aluminum garnet – $Lu_3Al_5O_{12}$; LuAG) and lutetium/yttrium oxyorthosilicates (Lu_2SiO_5 and Y_2SiO_5; LSO and YSO) with subsequent surface modification with amorphous silica shell, conjugation with biomolecules (protoporphyrin IX and anti-FasL antibody) and concept of biocompatibilization by polyethylene glycol (PEG) molecules attachment.

Parts of this work were performed by students under my direct supervision and guidance: Michaela Šípková (LSO:Ce^{3+} synthesis and TG/DTA analysis), Ing. Kateřina Tomanová (dense-liquid and combination of dense-liquid with sol-gel technique for surface modification of the nanoparticles) and Bc. Jindřich Fleišmann (conjugation of PEG molecules with nanocomposites).

My own contribution to this work is:

- development and design of the luminescent nanocomposites for PDTX and cathodoluminescence bioimaging modalities;
- sol-gel method for LSO/YSO:Ce^{3+} powders synthesis;
- synthesis of the nanocomposites for PDTX and cathodoluminescence bioimaging;
- successful surface modification and biofunctionalization of the nanoparticles with average size higher than 25 nm;

- concept of biocompatibilization of the nanocomposites;
- analysis of measured data and characterization of the prepared materials;
- study of radiative energy transfer between nanocomposites core and photosensitizer layer with subsequent singlet oxygen production.

2. Theory

2.1. Nanocomposite materials

2.1.1. Basic principles

Nanocomposites are multicomponent materials comprising multiple different phase domains in which at least one type of phase domain is a continuous phase and in which at least one of the phases has at least one dimension of the order of nanometers (Chen et al., 2008). The main idea of the nanocomposite is to offer significant advantages as compared to conventional bulk formulations, which is achieved by synergy between individual components (Omanović-Mikličanin et al., 2020). Chemical reactivity and physical properties of the nanocomposite materials differ from the bulk composite materials of the same chemical composition due to nanomaterials incorporated into the structure. These differences are determined by two primary nano-scale factors:

1. *quantum size effect* – the size of the nanoparticle (NP) is too small to be comparable to de Broglie wavelength of the conductive electrons, that results in the confinement of their movement ("particle in a box" model) (Roduner, 2006). The quantum confinement leads to the formation of discrete energy levels, unlike the continuous energy levels in bulk counterparts (Saravanan, 2016). Due to this reason, nanomaterials possess unique optical properties, such as blue shift in absorption or emission spectra of nanoparticles, which is sensitive to changes in their size and shape, novel electrical and magnetic behaviors (Siegel, 1993).
2. *surface effect* – as a particle decreases in size, a greater proportion of atoms is found at the surface compared to the total number of atoms. Higher surface-to-volume ratio compared to bulk materials have significant effect on the nanomaterials properties, e. g. reduced melting point, high mechanical strength and enhanced catalytic activity (Christian et al., 2008; Saravanan, 2016).

Nanocomposite materials can either combine NPs with other NPs or NPs combined with bulk materials (e.g. polymer- or metal-based) or more complicated structures, such as a metal-organic frameworks (Jeevanandam et al., 2018). Based on the principle of the

nanoparticles incorporation, nanocomposite materials can be divided into two basic categories: nanolayered materials, nanocomposites with nanoparticles dispersed in bulk matrix and core-shell nanocomposites (Fig. 2). Controlling of size, morphology and defects of the different components of the nanocomposite can help to adjust mechanical, optical, electrical and catalytic activity of the nanomaterial (Wang et al., 2014).

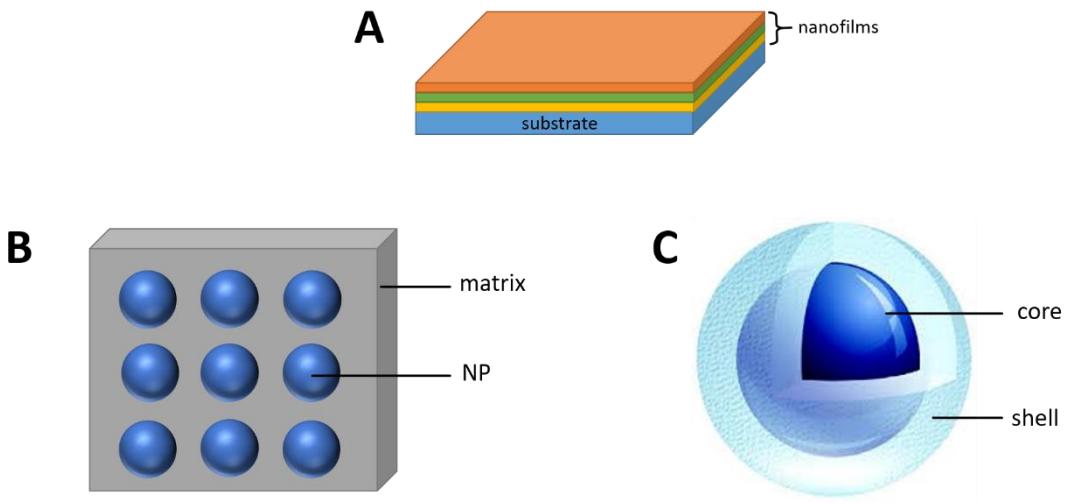

Fig. 2: Schematic representation of different morphologies of nanocomposites: nanolayered materials (A), matrix-dispersed nanoparticles (B) and core/shell systems (C).

Nanolayered materials are nanocomposite materials formed by planar layer-by-layer deposition of solid films to surface of organic or inorganic substrate with a thickness ranging from several nanometers to several dozen of nanometers. The nanolayers are usually produced by electron-beam and laser evaporation, magnetron deposition or molecular beam epitaxy (Balasubramanyam et al., 2020; Iler, 1996).

Matrix-dispersed nanoparticles is a type of nanocomposites, where, in the ideal case, nanoparticles are finely dispersed in dense bulk materials. As a matrix material, both organic and inorganic compounds can be used, but usually polymers, ceramics and metal matrices are utilized. Polymers are a commonly used organic matrix. For example, ZnO:Ga nanoparticles in powder form were embedded in polystyrene matrix forming ZnO:Ga-polystyrene nanocomposite material (Burešová et al., 2016). Synergic effect of interaction between ZnO:Ga and polystyrene was observed. Other most commonly used polymers are polyvinyl toluene (PVT) (Chai et al., 2013), polymethyl methacrylate (PMMA) (Sen et al., 2017), polyvinyl alcohol (PVA) (Pucci et al., 2008) and many others.

The disadvantage of organic matrices is lower radiation and temperature stability as compared to inorganic ones.

Core/shell structures, also referred as composite nanoparticles or surface-modified nanoparticles, represent the third type of nanocomposite morphology (Vollath and Szabó, 1999). Core/shell structure is formed by coating of a nanoparticle by a nanoshell with desired properties. When these nanoparticles contain an inorganic core and an organic shell one may speak about hybrid nanoparticles. In this case the inorganic core may be a metal or a metal oxide, and the organic shell either a polymerized monomer, a chromophore, a detergent or surfactant, carbon, or some organic molecule (Hanemann and Szabó, 2010).

Amorphous cross-linked SiO_2, which is also considered as an inorganic polymer, is the most frequently used inorganic shell for coating all sorts of core nanomaterials. Silica is an excellent candidate as a shell material due to its chemical inertness, controlled porosity, high processability and optical transparency. Encapsulation in amorphous silica shell is mainly used to improve colloidal stability of the nanoparticles, especially in water-based media (Ansari, 2018; Hu and Gao, 2011), to heal surface defects and enhance luminescence intensity of the nanoparticles (Procházková et al., 2019), and to reduce particles aggregation during heat treatment of nanomaterials (Raevskaya et al., 2014). Furthermore, silica shell allows core nanoparticle to be easily bioconjugated with functional groups (NH_2–, SH–), which are necessary for further coupling with bioactive molecules for biomedical, diagnostic and therapeutic applications of nanomaterials (Guerrero-Martínez et al., 2010; Kong et al., 2007).

Another type of the nanocomposite with core/shell morphology is a system, consisting of a nanoparticle as a core, which is covered by shell made of material with the similar lattice constant to avoid the formation of defects at the core–shell interface. The system allows to heal defects on the boundary between the core and the shell, and, as a consequence, to reduce influence of surface defect on the luminescent properties of the core. In this structure, the distance between the light-emitting ions in the core and the surface quenchers is increased, thus the non-radiative pathways are reduced and the quantum yield of nanomaterials is increased (Li and Lin, 2010). For example, the emission intensity and lifetime of the $CeF_3:Tb^{3+}/LaF_3$ (core/shell) nanoparticles increased with respect to those of $CeF_3:Tb^{3+}$ core particles (Wang et al., 2006).

$CePO_4$:Tb@$LaPO_4$ core/shell NPs with a total quantum yield (QY) of 80%, which was quite close to the value of the bulk material was also obtained (Kömpe et al., 2003).

2.1.2. Luminescent nanocomposites

A luminescent nanocomposite is a nanocomposite material with nano-scale luminescent particles as a major component. Luminescent nanoparticles convert different types of absorbed energy into the form electromagnetic radiation. After interaction of luminescent material with ionizing radiation or high energy particles, the process of scintillation occurs (Blasse and Grabmaier, 1994). The process of scintillation is divided into three steps: conversion, transport and luminescence (Fig. 3). During conversion step, interactions of ionizing radiation with the lattice occur and many

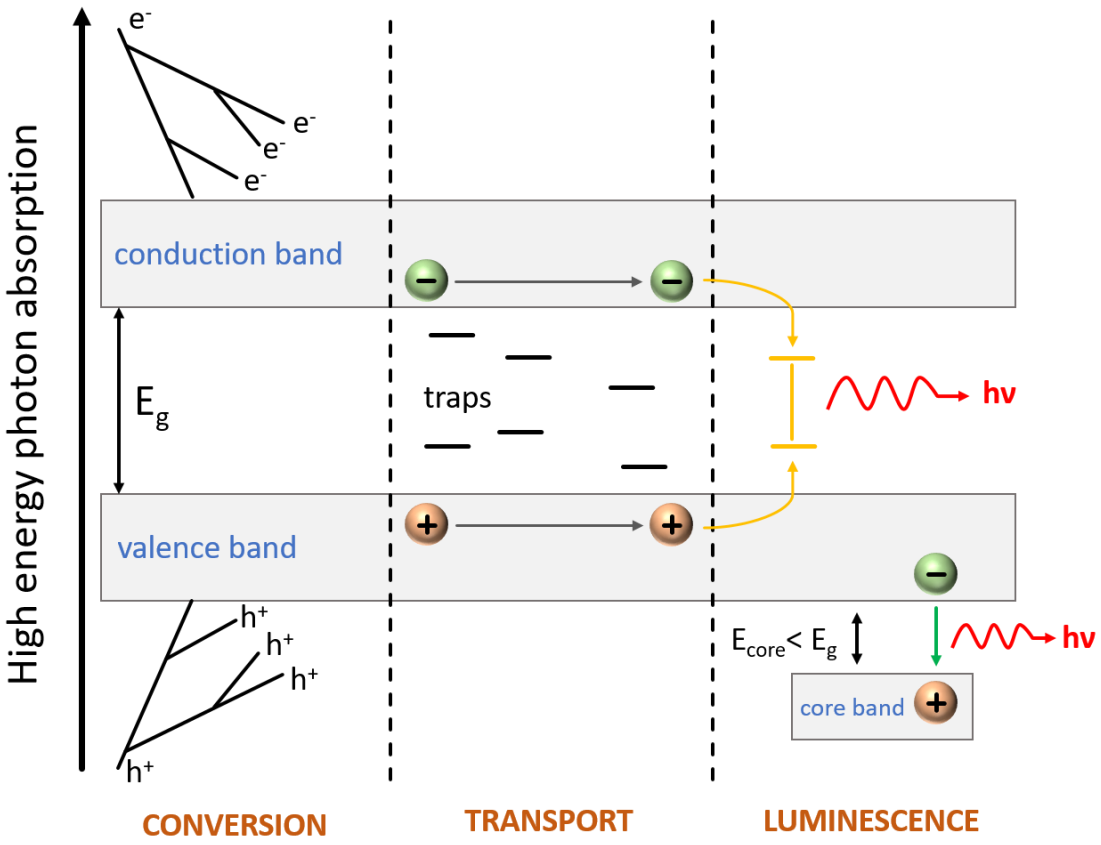

Fig. 3: Schematic illustration of the scintillator conversion mechanism (Nikl, 2006).

electron-hole pairs are formed in the valence band and conduction band, respectively. In the transport process, electrons and holes migrate through the material and could be trapped that leads to non-radiative recombination and energy loss. In the final luminescence step, the electrons and holes are trapped in the luminescence center with

subsequent radiative recombination (Nikl, 2006). Specific process of cross-luminescence may also occur after radiative transition between core band and the valence band (Jansons et al., 1992).

Basic concept of luminescent nanocomposite materials development is improvement and optimization of the physical and chemical properties when compared to the characteristics of the large-volume crystals of the same chemical composition. Furthermore, these new nanocomposite materials have advantages of being low cost and easily formed into practically any shape or size (McKigney et al., 2007; Stange et al., 2008), which in some situations can be very useful indeed (Wilson et al., 2020).

Due to the aforementioned properties, luminescent nanocomposites have been attracting more attention in lighting and sensors applications (Qiao et al., 2019; Schäferling, 2012), detection of ionizing radiation (Sahi and Chen, 2013) and biomedical fields (Montalti et al., 2014; Yao et al., 2014). Examples include PMMA-based nanocomposite with embedded Yb_2O_3/Er_2O_3 nanoparticles used as waveguide optical amplifier (Quang et al., 2006); transparent gadolinium oxide-polymer nanocomposite for application in gamma-ray spectroscopy was synthesized, and it was shown, that luminescence quenching and opacity were successfully avoided, as compared to the bulk materials used for spectroscopic detection in the past (Cai et al., 2013); CeF_3/ZnO core/shell nanocomposite with efficient energy transfer from CeF_3 core to ZnO and enhanced intensity of photoluminescence compared to ZnO nanoparticles only, making the material promising for applications not only in radiation detection, but also in solid state lighting, biological sensing and solar cell enhancement (Sahi and Chen, 2013).

2.1.3. Multimodal nanocomposites

Many luminescent nanocomposite materials were developed for biomedical applications, both for therapy and imaging modalities. Recently, increased attention has been focused on creation of multimodal drugs based on nanoscale materials for various applications in biological and medical fields (Lee et al., 2012; Trequesser et al., 2013; Chen et al., 2014). The multimodal drug usually allows simultaneous diagnostics (imaging), drug delivery and therapy (Li et al., 2016; Key and Leary, 2014; Cui et al., 2019).

Multimodality of the luminescent nanocomposite material is provided by selecting an appropriate outer shell depending on the area of application, which can be as follows:

- *X-ray induced photodynamic therapy (PDTX)*: outer shell of the luminescent nanocomposite contains molecules of the photosensitizer and biomolecules to make the nanocomposite agent biocompatible and avoid interferences with the metabolism or immune system of the human body;
- *bioimaging*: nanocomposite consisting of the luminescent core and conjugated with antibodies for specific bonding to cell membranes can be used for high-resolution cathodoluminescence (CL) bioimaging;
- *targeting*: proteins, capable of specific bonding to the membranes of certain type of cells (e.g. tumor cells), can be bound to the outer shell;
- *radiodiagnostics*: biocompatible targeted nanocomposites can be enhanced by adding radionuclides for simultaneous immunofluorescence, radiation therapy or radiodiagnostics.

For any biological applications, the multimodal agent must comply with a number of conditions:

1) nontoxicity for organism and chemical stability of the nanocomposite inclusive in a biological environment;
2) availability of the chemical procedures for nanoparticle surface coating and conjugation of biomolecules required for a particular application (Hu et al., 2009);
3) drugs should be able to reach the specific sites in the body via active (ligand-receptor interactions) or passive (enhanced permeability and retention effect) targeting (Bamrungsap et al., 2012);
4) nanocomposites must be biocompatible to avoid unwanted immune response and interactions with physiological environment and metabolism (Liu et al., 2010).

2.2. X-ray induced photodynamic therapy

Alternative application of luminescent nanocomposite materials based on scintillating nanoparticles in medical field focuses on their application in medical

therapy. X-ray induced photodynamic therapy (PDTX) is a non-invasive method of cancer treatment, which uses scintillating nanoparticles conjugated with photosensitizer (PS) molecules, as a tumor-destroying agent. Such nanocomposite agent accumulates preferentially in the target cells; subsequently, external X-ray irradiation leads to the excitation of the luminescent core resulting in the emission of the secondary radiation (scintillation) and subsequent radiative energy transfer (ET) to the photosensitizer in ground state (S_0), which is able to promote peripheral PS molecules to the singlet excited state (S_1) and then to the triplet excited state (T_1) through intersystem crossing (ISC) (DeRosa and Crutchley, 2002; Bulin et al., 2013; Bulin et al., 2015; Retif et al., 2015). Deexcitation of the photosensitizers triplet state in an oxygen environment via non-radiative ET leads to the production of the reactive oxygen species (ROS), where the singlet oxygen ($^1O_2$) is widely believed to be the most cytotoxic one (Weishaupt et al., 1976; Skovsen et al., 2005). General mechanism of the singlet oxygen generation during PDTX is schematically illustrated in Fig. 4.

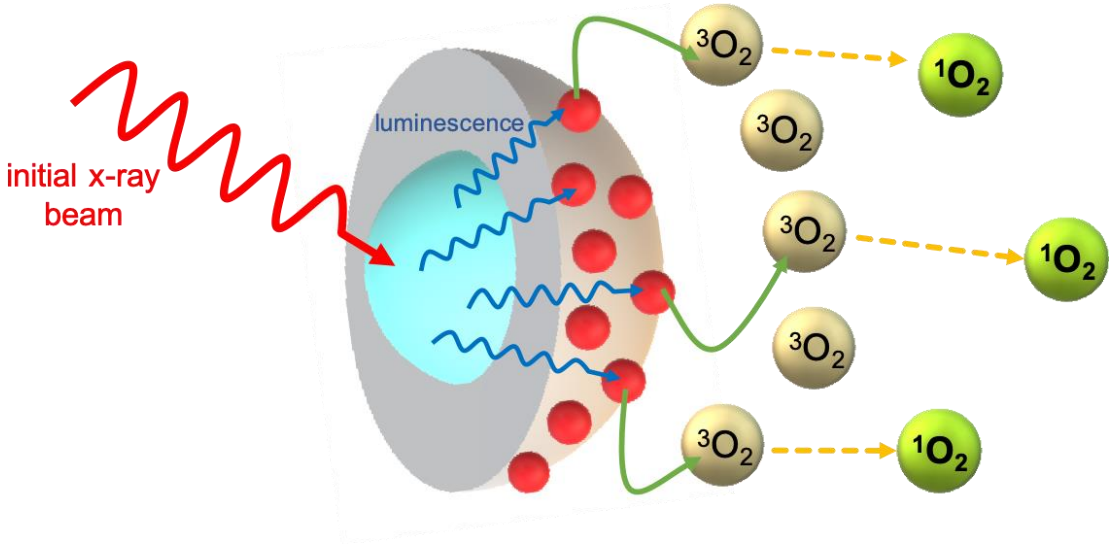

Fig. 4: Schematic illustration of the PDTX principle and singlet oxygen generation process using core/shell luminescent nanocomposite coupled with the photosensitizer molecules as a PDTX agent.

Deexcitation of the PS may occur through two types of reactions. In the first *type I* reactions, the PS oxidizes cellular substrate (biomolecules) forming different radical species, which can further react with oxygen molecules forming other ROS. In *type II* reactions, the excited PS relaxes through triplet-triplet annihilation (collisions) with $^3O_2$ molecules forming $^1O_2$ according to the equations:

$$PS(S_0) \xrightarrow{h\upsilon} PS(S_1) \xrightarrow{ISC} PS(T_1) \quad (1)$$

$$PS(T_1) + {}^3O_2 \xrightarrow{\substack{non-radiative \\ ET}} PS(S_0) + {}^1O_2 \quad (2)$$

Above described processes of the PS excited states generation and ROS production are schematically illustrated in Jablonski diagram shown in Fig. 5.

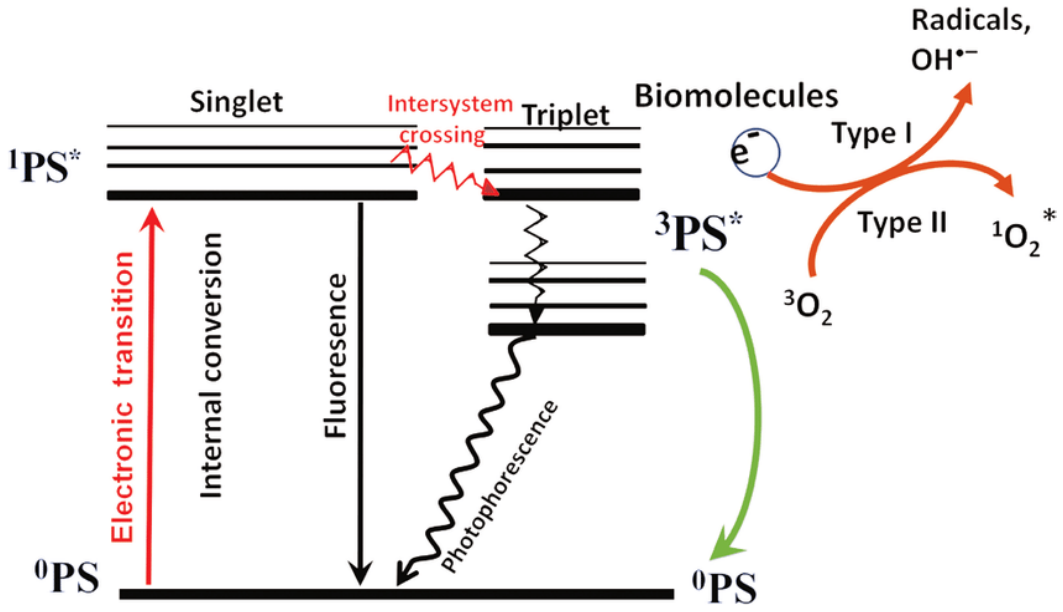

Fig. 5: Jablonski diagram illustrating generation of the photosensitizers' excited singlet and triplet states and ROS production (Sadasivam et al., 2013).

Result of PDTX is dictated by the second type of the reactions and amount of singlet oxygen generated; but in hypoxic environment type I reactions can also play the key role (Chen, 2008a; Baptista et al., 2017). ROS causes cellular damage via necrosis or apoptosis processes through type I and type II reactions, respectively (Kochevar et al., 2000).

The principal advantage of PDTX with respect to the conventional photodynamic therapy (PDT) (Chen and Zhang, 2006; Colombeau et al., 2016) is that deeply residing tumors can also be treated (Liu et al., 2008a; Liu et al., 2008b), while keeping surrounding tissues at the low level of radiation. PDTX combines advantages of both PDT and radiation therapy to achieve the most efficient treatment, because the synergistic effect in PDTX can be reportedly expected (Bulin et al., 2019). W. Chen also assumed, that PDTX can be more efficient than conventional PDT by a factor of about 100 (Chen, 2008b).

The efficiency of PDTX is determined especially by highly effective energy transfer associated with optical characteristics of both nanoscintillators and photosensitizers, which are taken into account during nanocomposites design. Firstly, to effectively trigger photodynamic effect under X-ray irradiation, the scintillators should have a strong absorption capacity for irradiation, and strong X-ray-excited optical luminescence with high scintillation light yield (LY). Secondly, to achieve efficient energy transfer from scintillators to photosensitizers, the emission of the nanoscintillators should have maximum overlap with the absorption band of the photosensitizer (Sun et al., 2020). Also, an appropriate distance between scintillators and photosensitizers is required. Generally, in order to have efficient energy transfer, the distance between the donor and the acceptor should be less than 10 nm (Chen and Zhang, 2006).

2.3. Cathodoluminescence bioimaging

Cathodoluminescence microscopy is a new promising non-destructive tool in biological imaging with nanoscale and higher spatial resolution than fluorescence microscopy imaging. Cathodoluminescence (CL) is electromagnetic radiation ranging from ultraviolet (UV) to infrared spectral region, which is emitted from the material that was excited by high-energy accelerated electrons (cathode rays) of an electron beam (Blasse and Grabmaier, 1994).

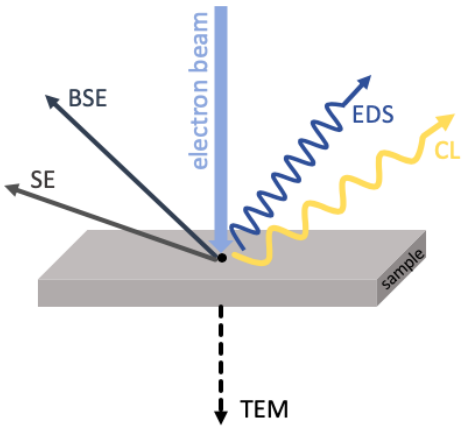

Fig. 6: Processes occurring after interaction of high-energy electron beam with the material.

After interaction of the electron beam with the sample, a number of processes occurs (Fig. 6), which belongs to the large group of scanning electron microscopy (SEM) techniques. The most commonly used techniques are secondary electrons (SE) and backscattered electrons (BSE) detection, electron backscattered diffraction (EBSD) and energy-dispersive X-ray spectroscopy (EDS). These methods are often utilized to obtain various types of the information about the material, such as surface topography, material contrast, crystal structure quantitative elemental analysis of the

sample (Prior et al., 1999). Cathodoluminescence detection technique provides information complementary to the above mentioned methods and additionally used to characterize optical properties (e.g. map of the optical activity, electronic band gap structure) at the nanoscale. Furthermore, many trace elements or dopants, can be detected with CL because they have different optical transitions than the bulk materials they are embedded in (Edwards and Martin, 2011).

CL technique has been extensively used for applications in biological imaging for many years. This bioimaging technique may be used for studying the structure and composition of cells and tissues: with cathodoluminescence generated by an electron beam, it is possible to obtain luminescence data with a much higher spatial resolution than is attainable in a conventional optical microscope. In addition, organic dyes commonly used in bioimaging techniques have limitations of their effectiveness due to narrow excitation bands and broad emission bands with red spectral tail leading to overlaps and problems with detection. In addition, such materials have low resistance to photodegradation (Lu et al., 2004). In contrast, CL bioimaging commonly uses rare-earth (RE) doped luminescent nanoparticles as fluorescent dyes because of their low toxicity, high luminescence intensity, larger Stokes shift as compared to organic labels, and possibility of tuning their emission spectral ranges by various doping (Labrador-Páez et al., 2018). Brightness and short emission lifetimes are also critical parameters of luminescent nanoparticles characteristics for application in this field (Zhang et al., 2014). However, the major drawback of CL bioimaging is its destructivity. The electron beam used for the excitation of the luminescent probes is potentially damaging to the biological samples and the labels themselves. Thus, the additional requirement to luminescent probe properties is outstanding stability under high energy electron beam excitation. As an example, multicolor CL nanobioimaging using RE-doped Y_2O_3 nanoparticles as fluorescent probes was presented in Furukawa et al. work (Furukawa et al., 2015).

Many NPs can be easily introduced into cells and tissues and can be even targeted to the specific sites. Basic mechanism used in bioimaging for intracellular fluorophore uptake is endocytosis. Using this process, the cells are able to retrieve materials from their surface or from the extracellular space and transport them through endosomal compartments to lysosomes, working as a “recycling center” in the cell

(Chandler and Roberson, 2009). Endocytosis allows to introduce nanophosphors into cells to demonstrate intracellular architecture and components in high resolution.

Another approach is based on a site-specific receptor-targeted fluorolabeling. The concept assumes conjugation of luminescent nanocomposite to the receptor on the cell membrane forming ligand-receptor bonds involved in the specific interactions between antigens (Ag) and antibodies (Ab). Such receptor-targeted bioimaging could help to identify specific proteins and receptors on the cells membrane. Architecture of the nanocomposite material for receptor targeting is composed of the luminescent core (nanoparticle) surrounded by layers of protective shell to avoid reduction of luminescence intensity via non-radiative processes at the surface, molecules of surface modifiers that provide their colloidal stability, minimal toxicity and targeting abilities (Labrador-Páez et al., 2018). A number of papers dealing with core-shell materials for bioimaging was published. Bentzen et al. demonstrated preparation of hybrid structure based CdSe/ZnS core/shell coated with amphiphilic poly(acrylic acid), which was able to non-specifically bind to human epithelial kidney cells (Bentzen et al., 2005). Wilhelm et al. prepared $NaYF_4$:Yb,Er (Yb,Tm)-based nanocomposite covered with silica shell and subsequently conjugated it with a polyethylene glycol spacer carrying N-hydroxysuccinimide groups (Wilhelm et al., 2013). The resulting particles form stable dispersions in aqueous solution and have high affinity to proteins such as streptavidin and bovine serum albumin, making the nanocomposite attractive for application in bioimaging.

2.4. Nanocomposites design

As it was mentioned in Section 2.1.3., there are at least four different functional modalities, which could be provided by luminescent nanocomposite agent. Despite the differences in the principle of their action, the fundamental idea of their preparation is similar. Procedure of the luminescent nanocomposite design for biomedical applications typically includes four main steps. In the first step, the scintillating nanoparticle core of the nanocomposite with suitable chemical, morphological and luminescence characteristics is prepared. In the next step, the surface of the core is modified by outer shell, which helps to improve chemical and colloidal stability, physical properties and to grow functional groups on the surface for further attachment of biomolecules. Surface

modification is then followed by the third process of biofunctionalization, which is based on the conjugation of different biomolecules, such as photosensitizers, antibodies and other proteins, depending on the area of application. In the final step, biocompatibility of the biofunctionalized luminescent nanocomposite is ensured to suppress undesirable cytotoxic, immunogenic and thrombogenic effects (Sperling and Parak, 2010; Conde et al., 2014). Fig. 7 presents a basic concept of the multimodal drug structure for application in bioimaging and PDTX.

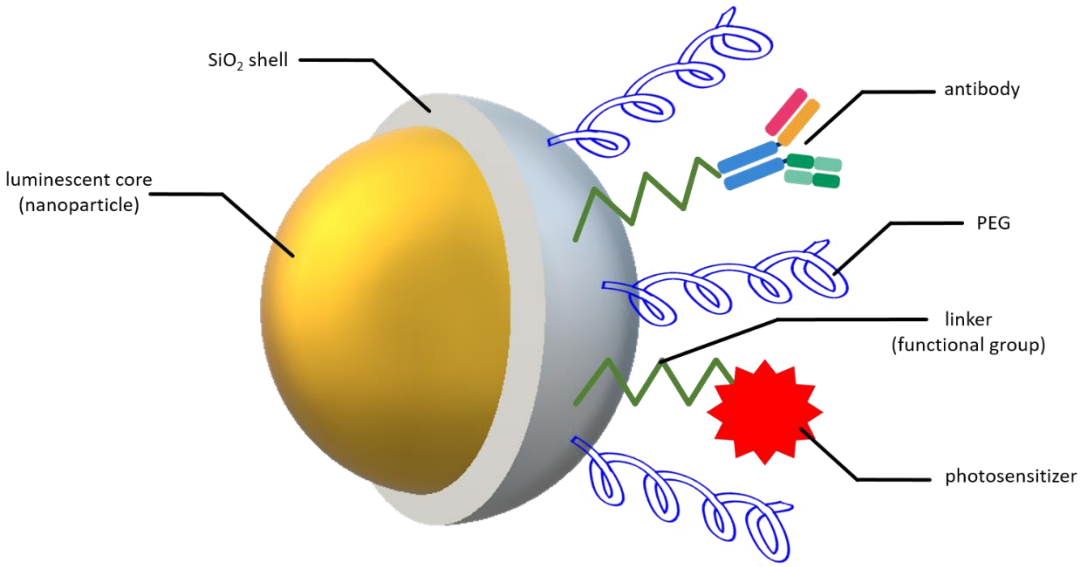

Fig. 7: Concept of structure of the nanocomposite material. Luminescent core is covered with silica shell and subsequently conjugated with a photosensitizer molecule, antibody and PEG molecules for application in PDTX, bioimaging and biocompatibilization, respectively.

In the following sections, each step of nanocomposite design, including description of the techniques and approaches used in this work, will be discussed in details.

2.4.1. Nanoparticle core

Requirements for biomedical applications of nanomaterials involve using of core made of chemically stable, non-toxic nanoparticles with low reactivity, high effective atomic number (Z_{eff}) and average size in the range of a few to hundreds nanometers (Cheng and Lo, 2011; Misawa and Takahashi, 2011). Excitation of nanoparticles must result in high luminescence efficiency. If scintillating nanoparticles are used, the excitation is performed by radiation, and the nanoparticle must emit strongly after

irradiation by X-rays. Moreover, for application of the nanocomposite in PDTX treatment, radioluminescence emission spectra of the core must overlap with the absorption spectrum of chosen photosensitizer molecules for effective activation of the photosensitizer (Chen, 2008a).

From these point of view, RE-doped synthetic garnets, such as lutetium aluminum garnet (Lu_3Al5O_{12}:RE, LuAG:RE), RE-doped yttrium oxyorthosilicate (Y_2SiO_5:RE, YSO:RE) and lutetium oxyorthosilicate (Lu_2SiO_5:RE, LSO:RE) seem to be highly prospective. Their structure and properties will be elucidated in following sections.

2.4.1.1. Lutetium aluminum garnet (LuAG)

Synthetic garnets are oxides with general formula $RE_3^{III}M_2^{III}(X^{III}O_4)_3$, where RE is a rare earth ion, M and X are usually Fe, Al or Ga. Lutetium aluminum garnet ($Lu_3Al_5O_{12}$, LuAG) is one of the synthetic garnets. Structurally, the garnets correspond to the naturally occurring $R_3^{II}M_2^{III}(SiO_4)_3$ silicates with cubic crystal system and $Ia\bar{3}d$ space group. The unit cell of the LuAG encompasses three lattice sites: tetrahedral AlO_4, octahedral AlO_6 and dodecahedral LuO_8 (Fig. 8).

Nanocrystalline LuAG exhibits extremely high degree of mechanical and chemical stability, thermal stability up to 2000 °C, cubic structure, which could prevent mechanical damage of the tissue. It is also characterized by high density (6.73 g/cm^3), high effective atomic number (Z_{eff} = 58.9) and radiation stability (Bárta et al., 2012; Xu et al., 2013).

Due to the closed-shell $4f^{14}$ electronic configuration of Lu^{3+} ion, it is expected that high quality undoped LuAG crystals will have no emission lines in the spectrum. Nevertheless, presence of unwanted host luminescence in the range of 280 – 340 nm in undoped LuAG was observed (Babin et al., 2005; Ogino et al., 2009). The phenomenon was caused by Lu_{Al} anti-site defect due to occupation of some octahedral Al sites by Lu atoms. Another type of unwanted luminescence in LuAG host may be caused by impurities embedded in precursor materials, such as Cr^{3+} (strong red luminescence) (Hehir et al., 1974), trivalent RE ions with 5d – 4f (Ce^{3+}), 4f – 4f (e.g. Tm^{3+}, Eu^{3+}, Nd^{3+}) or both 5d – 4f and 4f – 4f transitions (Pr^{3+}) (Sugiyama et al., 2011). Thus, the preparation of LuAG host matrix suitable for other dopants requires high purity of starting materials (~99.999%).

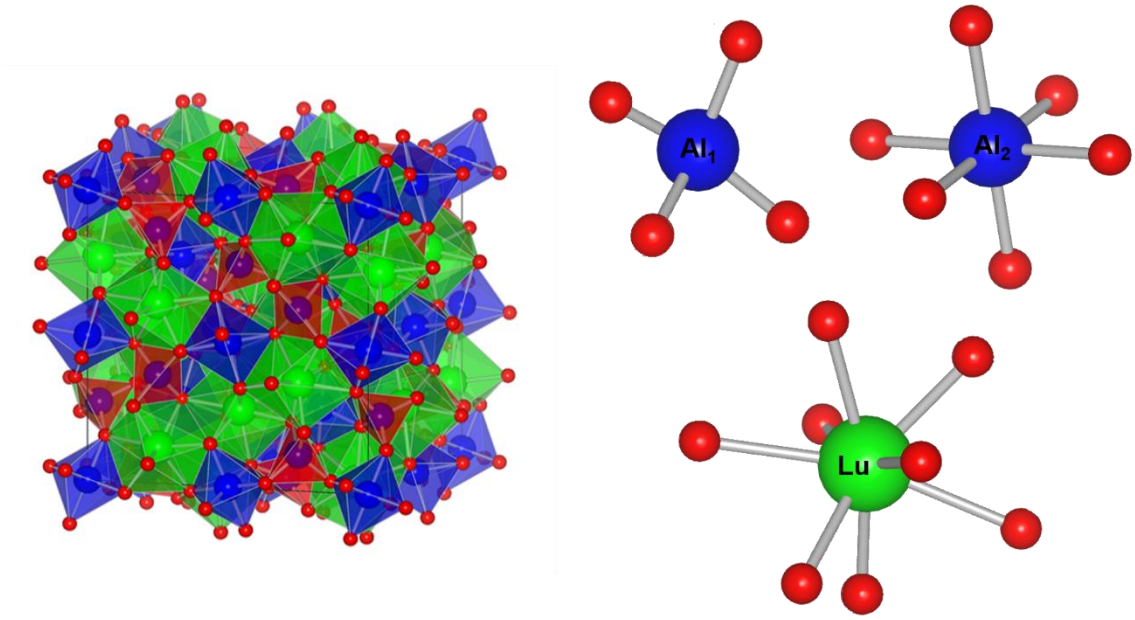

Fig. 8: Structure and lattice sites in the unit cell of LuAG crystal with green Lu^{3+}, blue Al^{3+} and red O^{2-} ions.

LuAG structure is a good candidate as a matrix for various RE dopants with both 5d – 4f and 4f – 4f transitions. One of the most important examples of RE-doped lutetium aluminum oxide is LuAG:Ce^{3+}. This scintillating material with an efficient luminescence provides fast light decay (60 – 80 ns) on account of the parity-allowed 5d – 4f transitions in Ce^{3+} characterized by broad emission band in the range between 450 nm and 650 nm with maximum at 520 nm with a light yield of about 12000 - 14000 photons/MeV (Mares et al., 2004).

Doping with Pr^{3+} ions also provides high luminescence intensity due to 5d – 4f transitions with faster decay time (20 – 21 ns) compared to Ce^{3+}-doping of LuAG host. The emission band is extended in the near UV spectral region from 280 – 410 nm with maximum at 310 nm. (Ogiegło et al., 2013; Ogino et al., 2006). Beyond 5d – 4f transitions, Pr^{3+} ions in LuAG:Pr^{3+} exhibit 4f – 4f emission transitions from $^3P_0$ and $^1D_2$ levels to the $^3H_4$ and $^3H_6$ ground states (Vondrášková et al., 2016), which appear with number of sharp peaks in visible spectral part. The intensity of these 4f – 4f transitions is comparatively weak and emission produces long decay times of several milliseconds, because these transitions are spin and parity forbidden (Blasse and Grabmaier, 1994).

Nanoscale LuAG:RE particles may be prepared by several conventional methods. Xing et al., demonstrated synthesis of LuAG nanoparticles via one-step solvothermal route using aluminum nitrate and lutetium nitrate as raw materials and

ethylenediamine solution as the reaction medium (Xing et al., 2018). In Uhlich et al. work, co-precipitation method was employed for preparation Eu^{3+}-doped LuAG nanopowder (Uhlich et al., 2007). Many other chemical routes, e.g. sol-gel (Boukerika and Guerbous, 2015) and solid state reaction method (Wu et al., 2014), have been also utilized. However, for the most of these methods, strict control of the reaction conditions (e.g., pH, temperature) is required, and the reactions often lead to the formation of products with poor crystallinity or large particle size distribution due to agglomeration.

LuAG:RE nanoparticles can be also prepared using photo-induced method of synthesis. The technique is based on the irradiation of aqueous solutions containing reactants with UV radiation, subsequent absorption of UV quantum and excitation of target molecules leading to photochemical reactions (e.g. dissociation, charge transfer and rearrangement). Formic acid is usually added as a scavenger to form a precipitate of carbonate precursors with general chemical formula $M_x(OH)_y(CO_3)_z$, so that the calcination of the precursor to obtain final product is needed (Bárta et al., 2015).

In contrast to the conventionally used methods, the photochemical preparation technique has a number of advantages: the ongoing processes are almost independent of temperature, the reactions proceed with a very high yield and the final products have high chemical purity and a narrow particle size distribution (Bárta et al., 2012).

2.4.1.2. Yttrium/lutetium oxyorthosilicate (YSO/LSO)

Yttrium oxyorthosilicate (Y_2SiO_5, YSO) and lutetium oxyorthosilicate (Lu_2SiO_5, LSO) are monoclinic oxyorthosilicate compounds belonging to the C_{2h}^6 space group. Two lattice sites are found in the unit cell: tetrahedral SiO_4 and octahedral $(Y/Lu)O_6$ (Fig. 9).

X1-type YSO and A-LSO are transitional phases that are metastable and after heating up to crystal transition temperature, they transform irreversibly to X2-YSO and B-LSO, respectively. Both crystallographic types, for both YSO and LSO, are monoclinic, contain two distinct rare-earth sites and slightly differ in the coordination sphere around these sites. In A-LSO, Lu_1 has coordination number 8 (CN = 8) and average bond length of 2.38 Å, Lu_2 has CN = 7 and average bond length 2.31 Å. In B-LSO, Lu_1 has CN = 7 with average bond length 2.32 Å; Lu_2 has CN = 6 with average bond length 2.23 Å (Mueller-Bunz and Schleid, 1999; Gustafsson et al, 2001). X1- and X2-YSO have similar differences

(Table 1). The scheme, showing local coordination sphere of Lu sites in both LSO forms is shown in Fig. 10.

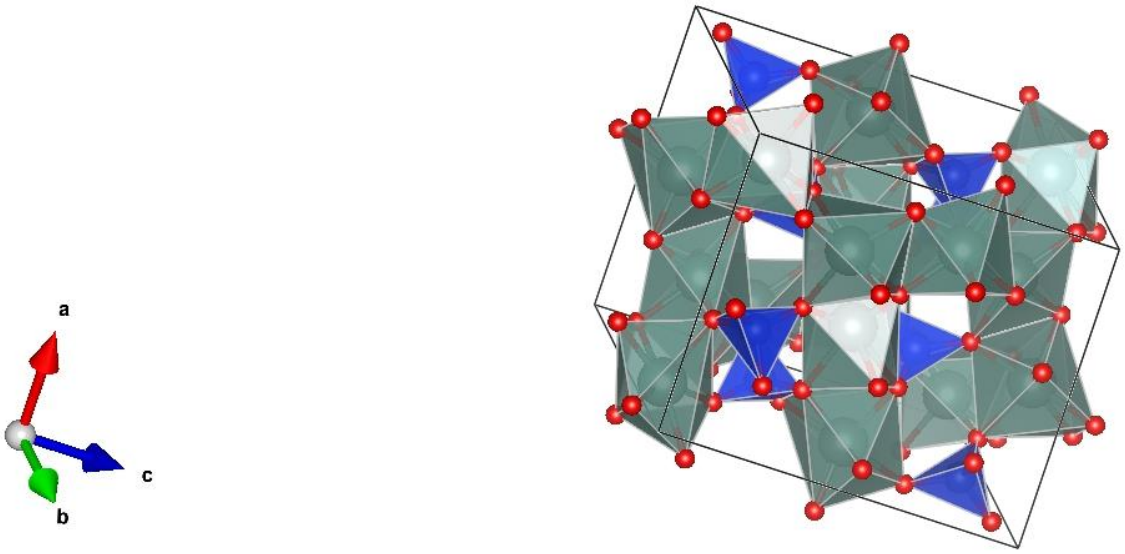

Fig. 9: Structure of YSO/LSO crystal with green Y^{3+}/Lu^{3+}, blue Si^{4+} and red O^{2-} ions.

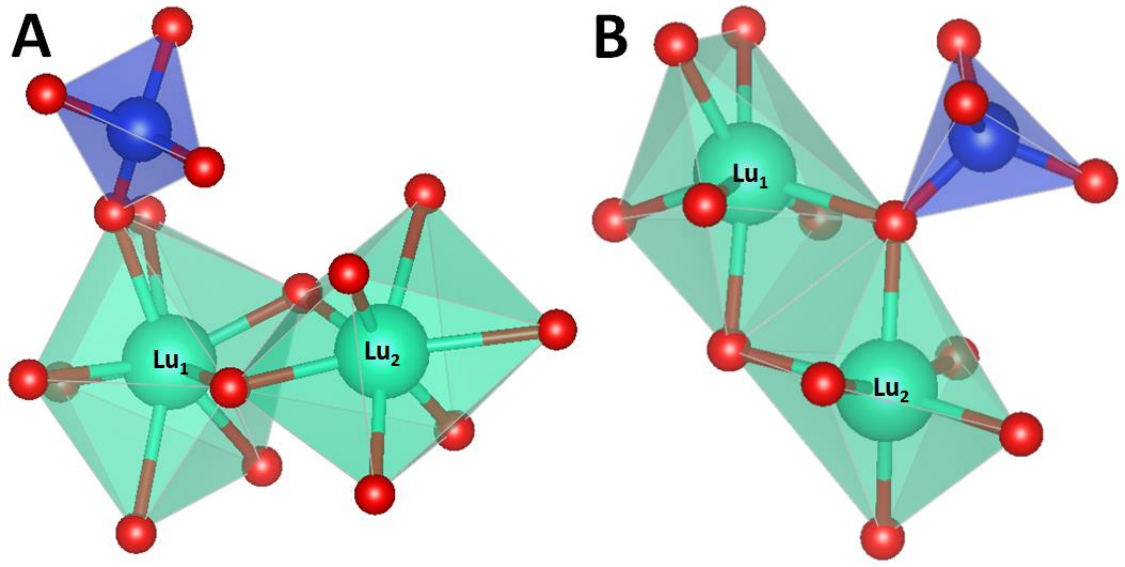

Fig. 10: Local coordination sphere of Lu sites in A-LSO (A) and B-LSO (B) with green Lu^{3+}, blue Si^{4+} and red O^{2-} ions. Both crystallographic types are monoclinic, contain two distinct rare-earth sites and slightly differ in the coordination sphere around these sites.

Table 1: Comparison of the lattice parameters for X1- and X2-type YSO (Wang et al., 2001; McMurdie et al., 1986) and A- and B-LSO (Mueller-Bunz and Schleid, 1999; Gustafsson et al., 2001).

	a [Å]	b [Å]	c [Å]	β [°]
X1-YSO	9.014	6.928	6.643	106.68
X2-YSO	12.501	6.728	10.422	102.68
A-LSO	6.987	6.706	6.595	104.18
B-LSO	14.277	6.64	10.246	122.22

Similarly to pure LuAG matrix, the YSO or LSO itself are optically transparent; however, desired luminescent properties may be also achieved by doping with RE^{3+} ions. RE ions substitute for the Y^{3+}/Lu^{3+} ions which occupy two crystallographic sites of C_1 symmetry. For example, Ce^{3+}-doped YSO shows intense wide-band emission in the range of 350 - 650 nm with a maximum at 420 nm (Muresan et al., 2016).

RE-doped YSO and LSO are usually available as bulk single crystals and crystal layers grown by Czochralski (Melcher and Schweitzer, 1992) or liquid phase epitaxy methods (Zorenko et al., 2013). Due to their properties, such as high density and Z_{eff}, high light yield and luminescence timing characteristics (Table 2), it is used as a component of detection systems in diverse applications, including high energy physics, security and medical physics. Crystal growth is usually a very expensive technique because of high temperature and very expensive crucible needed. YSO/LSO materials could be also prepared using sol-gel method. The process is based on hydrolysis with subsequent polycondensation reactions of alkoxides leading to formation of colloidal aggregates, which are finally dried. The method is proceeded under room temperature and allows preparation of pure powder materials with good structural and luminescent characteristics (Chiriu et al., 2016; Peterson, 2014). Considering their properties mentioned above, YSO:Ce and LSO:Ce powder materials prepared via sol-gel route could be prospective materials as a core of nanocomposite for application in biomedicine.

Table 2: Main characteristics of YSO:Ce and LSO:Ce bulk single crystal scintillators (Knoll, 2010).

	density [g/cm³]	Z_{eff}	$\lambda_{max.emission}$ [nm]	decay time [ns]	LY [ph./keV]
YSO:Ce	4.5	39	420	50 - 70	10
LSO:Ce	7.4	75	420	40	30

2.4.2. Surface modification

Surface modification process includes a number of methods, which help to avoid aggregation of nanoparticles, improve their colloidal stability, chemical and physical properties. The most commonly used techniques are ligand substitution, polymer coating and surface functionalization with amorphous silica shell.

To improve stability and provide desired functional groups on the surface of the nanoparticles for further biofunctionalization reactions, post-synthetic surface ligand exchange or polymer coating is performed. For example, citrate ions, absorbed on the NP surface during synthesis, can be replaced by sulphonated phosphines and thioglycolic acid, which bind stronger to the particle surface. This strategy is used to conjugate thiol-modified DNA molecules to the nanoparticles: firstly, phosphines substitute citrates, then thiol-containing ligand is added to replace phosphines (Sperling and Parak, 2010). Oleate can be substituted by PEG-phosphate, which makes nanoparticles water-dispersible (Boyer et al., 2010). To make nanoparticles water-dispersible, nanoparticles are covered by amphiphilic polymers, and as a result, the charge on the surface is induced by several layers of polyions (Tan, 2012).

The techniques applied for nanoparticles production mostly result in the formation of defects on the NP surface and poor isolation of RE^{3+} ions at the surface from the environment. Both consequences are then connected with increment of non-radiative processes and luminescence efficiency loss (Labrador-Páez et al., 2018). Surface silanization is a versatile process of surface modification, which can be used simultaneously for surface defects reduction and chemical functional groups introduction for further conjugation with other molecules. Amorphous silica shell can be deposited on the surface by sol-gel and dense-liquid methods.

2.4.2.1. Sol-gel

Sol-gel technique is a simple and widely used technique of amorphous silica layer deposition on inorganic particles surface, which includes transition from a liquid (sol) into a solid multiphase gel. The most commonly used groups of compounds for surface silanization are alkoxysilanes and organoalkoxysilanes. Silane molecules are very reactive toward inorganic substrates and able to form covalent linkages with other molecules and surfaces (Issa et al., 2019).

Typical sol-gel reaction consists of three steps (Fig. 11). The first step is hydrolysis of alkoxy groups and formation of highly reactive silanol intermediate. In the second step, the silanols are binding to each other via hydrogen bonding with subsequent silanol condensation and creation of polymer matrix in the solution with –Si–O–Si– bonds. Finally, the matrix interacts with –OH groups on the nanoparticles surface and the formation covalently bonds to inorganic substrate (Hermanson, 2013).

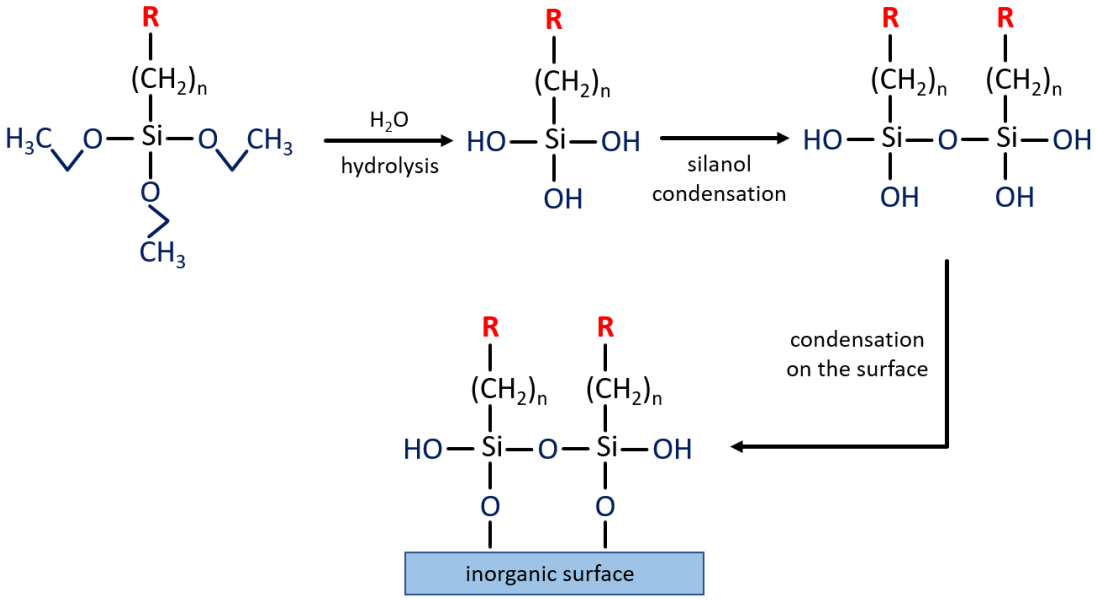

Fig. 11: Schematic illustration of reactions during sol-gel process involving coating of inorganic surface with amorphous silica shell.

Sol-gel processes are usually performed in aqueous solutions and can be proceed either at room temperature or elevated temperatures, which can help to accelerate the process of covalent –Si–O–Si– bond formation. Modification of pH is necessary to catalyze the hydrolysis step. Moreover, pH influences gelation step: acidic pH induces slow gelation, whereas alkaline conditions lead to its acceleration (Wright and Sommerdijk, 2001).

Result of sol-gel coating is a thick polymer layer of silica on the nanoparticle surface. Thickness of the silica shell depends on the amount of water and concentration of alkoxysilanes in the reaction solution. However, the growth of thin and uniform silane shell on a nanocrystal is still non-trivial (Li and Lin, 2010). Organoalkoxysilanes used for surface modification also contain reactive functional group at the end of the organic spacer. These reactive organic components stick out from the silica layer and can be used for further conjugation with biomolecules (e.g. antibodies, proteins,

oligonucleotides, etc.), containing appropriate chemical group for the reaction (Hermanson, 2013).

Sol-gel method allows creation of mesoporous silica shell with highly regular pore structures and high specific pore volumes, which can be used for drugs loading and releasing (Zhao et al., 2005; Arruebo et al., 2006). Kim et al. used CTAB as a stabilizing surfactant and as a template for the formation of mesopores during sol-gel reaction. After SiO_2-layer formation, CTAB was removed by reaction in acidic conditions and at high temperature. Moreover, NP-core was extracted by decreasing pH value and hollow mesoporous silica particles were formed. Its hollow core can be potentially used as a contrast agent or drug delivery vehicle (Kim et al., 2008).

2.4.2.2. Dense-liquid

Dense liquid coating is a method of amorphous SiO_2 layer deposition on the surface of nanoparticle from its supersaturated solution. SiO_2 could be dissolved in water only in strongly alkaline conditions. The addition of a strong alkaline silica solution to the suspension of nanoparticles at supersaturation level (elevated temperature, pH ≥ 9) leads to the condensation of silica shell on the surface (Liu et al., 1998).

Dense-liquid is a complex process consisting of consisting of three components: heterogeneous coating, homogeneous coating and formation of SiO_2 nuclei. For the silica layer deposition on the NP, the first and the second processes are important. During heterogeneous coating, SiO_2 is deposited on inorganic substrate; after that, condensation of SiO_2 on the formed SiO_2 layer occurs by prevailing homogeneous nucleation process. The result is random, island-like silica deposition.

The third process of SiO_2 nuclei formation is undesirable and occurs at high concentration of water glass and low pH level. Nuclei formation and its subsequent homogeneous coating can be avoided by slow water-glass addition and control of pH conditions (Caruso, 2001).

In Liu et al. work it was shown, that uniform silica layer can be formed by two-step coating process: sol-gel followed by dense liquid, or vice versa. In the first step, non-uniform, porous layer of silica is formed by sol-gel process; subsequently, sticking out epoxy groups can by hydrolyzed under supersaturation conditions (Liu et al., 1998); thus,

the pores are closed by dense-liquid process (Fig. 12). This method can provide uniform surface encapsulation for toxicity reduction of the core and for further functionalization.

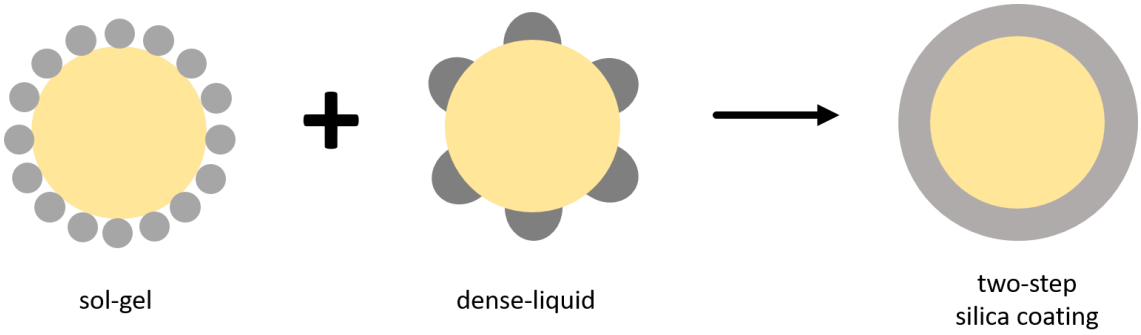

Fig. 12: Silica coating using sol-gel technique, dense-liquid process and combination of two methods leading to uniform modification of NP surface. Adapted from Liu et al. (Liu et al., 1998).

2.4.3. Biofunctionalization

2.4.3.1. Photosensitizers for PDTX

Photosensitizers for application in PDTX are chosen among the photosensitizers standardly used in conventional PDX based upon several criteria, such as low dark toxicity to mammalian cells, existence of easy chemical route of their conjugation with surface-modified NPs and optical absorption properties overlapping with emission of luminescent NP for effective energy transfer and inducing photodynamic effect. The most commonly used photosensitizers are porphyrins and its derivatives (Gallardo-Villagrán et al., 2019).

Protoporphyrin IX (PpIX) is the most frequently used photosensitizing agent, its molecular structure is shown in Fig. 13A. PpIX is naturally presented in living cells in small amounts as a precursor of heme, which is of vital importance in cellular metabolism, gas transport and catalysis of many reactions. PpIX has four weak absorption Q-bands centered at 506 (Q_{IV}), 540 (Q_{III}), 575 (Q_{II}) and 630 nm (Q_{I}) and intensive band of maximal absorption (Soret band) at 405 nm (Fig. 13B). Q-bands can be activated by visible spectrum light, making PpIX suitable for application in conventional PDT. 5d – 4f emission of LuAG:Pr^{3+} nanoparticles matches Soret band of PpIX; thus, effective energy transfer from the NP core to the photosensitizer molecules is expected, making PpIX a good candidate for PDTX nanocomposite preparation.

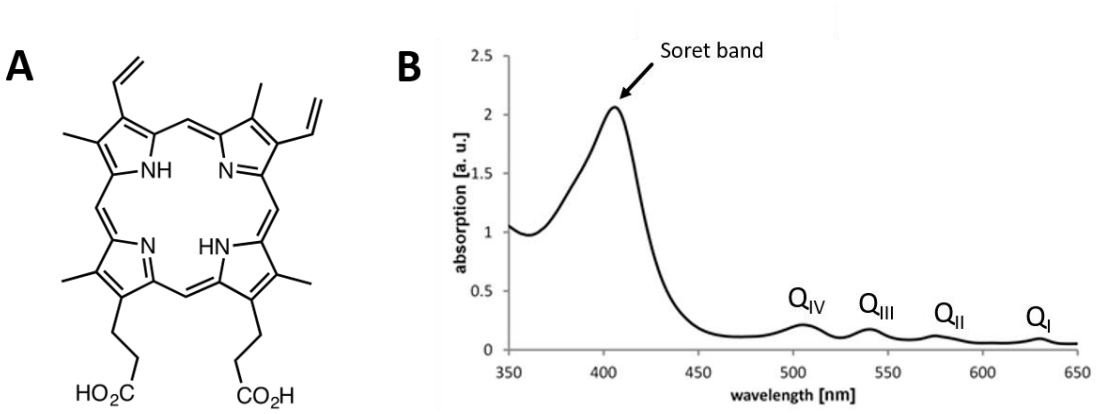

Fig. 13: Molecular structure of PpIX (A) and its UV/VIS absorption spectrum (B). The spectrum exhibits the Soret band peaked at 405 nm and four Q-bands arising at 506 nm (Q_{IV}), 540 nm (Q_{III}), 575 nm (Q_{II}) and 630 nm (Q_I).

Many methods of NPs and photosensitizers linkage are presented in literature. Recently it was shown, that PpIX can be covalently coupled with CeF_3:Tb^{3+}@SiO_2 nanoparticles using Schotten-Baumann reaction (Li, 2002). After X-ray excitation, emission of PpIX was observed, suggesting energy transfer from Ce^{3+} to Tb^{3+} and then to PpIX molecules (Popovich et al., 2016). Nowostawska et al. shown another approach of PpIX conjugation: amide-coupling reaction was performed between PpIX and APTES, after that, magnetite nanoparticles treated with sodium silicate were reacted with modified PpIX through hydrolysis process (Nowostawska et al., 2011). Unfortunately, experiments with the prepared porphyrin-magnetite nanocomposite on cell cultures shown photobleaching of the PpIX upon exposure to light under a fluorescent microscope. Clement et al. in their work conjugated CeF_3 nanoparticles with verteporfin (Clement et al., 2016). The production was measured with addition of singlet oxygen sensor green (SOSG) chemical probe. It was found, that pure CeF_3 nanoparticles are also able to produce single oxygen, but in smaller amount, as compared to formation with verteporfin.

Yefimova et al. described preparation of PDTX agent with photosensitizer adsorbed in the surface of NPs via Coulombic interactions (Yefimova et al., 2017). $GdVO_4$:Eu^{3+} was used as a donor and methylene blue as an acceptor for FRET. But despite the fact, that emission intensity of the donor strongly decreased, no FRET was observed, that was explained by number of factors, such as small amount of particles adsorbed on the NPs surface and low fluorescence quantum yield of the photosensitizer. Adsorption by electrostatic interaction of 5-aminolevulinic acid, a precursor of PpIX, on

gold nanoparticles was also presented in Mohammadi et al. work (Mohammadi et al., 2017). It was experimentally proven, that efficacy of PDTX with conjugate is greater, than for 5-aminolevulinic acid alone. Chen et al. shown another approach and loaded Merocyanine 540 to the pores formed by amorphous silica shell on $SrAl_2O_4:Eu^{2+}$ nanoparticles (Chen et al., 2015). The measurements shown absence of $^1O_2$ production for nanoparticles and photosensitizer alone, whereas was observed for the nanocomposite; thus, the energy transfer was also confirmed.

Abliz et al. tried to prepare nanocomposite material for PDTX treatment by conjugation of Photofrin II with $Gd_2O_2S:Tb^{3+}$ nanoparticles (Abliz et al., 2011). During studies it was observed, that fine Photofrin II accumulates preferentially in mitochondria, while the conjugate diffuses into lysosomes that decreased PDTX efficiency. Therefore, authors proposed to introduce separately free Photofrin II in addition to nanoparticles. The strategy shown good results in reduction of metabolic activity of human glioblastoma cells.

2.4.3.2. Antibody conjugation for biomedical applications

Conjugation of nanoparticles with different biomolecules, such as proteins, aptamers (DNA, RNA), plasmids, antibodies (Ab) and low molecular weight ligands (folic acid), provides them enhanced properties. Most of these biomoieties are often used in cellular drug delivery, they are selective and able to pass through molecular membrane. However, they have a number of drawbacks. For example, TAT-peptide can be transported through membrane independently on receptor-mediated endocytosis, but on the other hand it has short vascular circulation lifetime may be denatured by proteases. Another example is aptamers, but their usage in large quantities is rather expensive, as compared to antibodies, and they also may be degradable by enzymatic activity. In contrast to the majority of biomolecules used for biofunctionalization, antibodies combines improvement in cellular targeting via specific and selective recognition ability to the antigens and advantage of good intracellular stability (Arruebo et al., 2009).

Antibody, also called immunoglobulin (Ig), is a Y-form (Fig. 14) glycoprotein produced by immune system in presence of foreign substance, called antigen (Ag). Each antibody consists of two identical domains for antigen recognition, so-called Fab

fragments, and two identical Fc fragments for communication with other components of immune system (effector function). Antibody-antigen interaction occurs on the principle of lock and key: the Ab-paratope (lock) interacts with Ag-epitope (key) allowing the structures to bind together via weak interactions, such as van der Waals forces, hydrogen bonds and electrostatic interactions, making the formed Ab – Ag bond reversible.

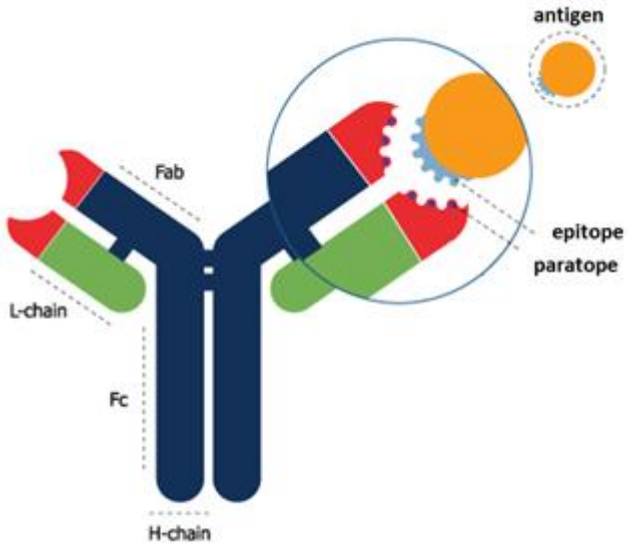

Fig. 14: Structure of antibody. Y-form is composed of two heavy chains and two light chains which are bind together by disulfide interchains.

Concept of nanoparticle-antibody conjugation assumes their application in two biomedical fields: targeted drug delivery in therapy and receptor-targeted bioimaging. Selective targeting systems involve active or passive targeting. Passive targeting is based on the enhanced permeability and retention (EPR) effect caused by enhanced vascular permeability of the tumor for macromolecular drugs, by which nanoparticles generally of sizes between 80 – 200 nm accumulate in solid tumors much more intensively than they do in the normal tissues (Maeda, 2001). Active targeting is based on the overexpression of epitopes or receptors on the tumor cells. Moreover, active targeting using physical properties, e.g. magnetism, of nanoparticles is also possible (Arruebo et al., 2007; Arruebo et al., 2009).

Three main strategies of antibody-nanoparticle coupling reactions are listed below:

1) *formation of antibody fragments*: first group of the reactions involve the cleavage of disulfide bridges with reducing agents, such as mercaptoethylamine (MEA) or dithiothreitol (DTT), to create two half-antibody molecules. Alternatively, $F(ab)_2$ fragments lacking of Fc region can be prepared by enzyme digestion with subsequent reduction to form Fab' fragments. In both cases, the prepared molecules contain –SH groups which can be used for conjugation with thiol-reactive crosslinkers (Hermanson, 2013; Crivianu-Gaita, 2015).
2) *aldehyde groups generating*: heavy chains of Ab are glycosylated in Fc fragment. Polysaccharides in this region may be oxidized used $NaIO_4$ to obtain aldehyde groups. Using this method crosslinkers holding functional groups with affinity to –CHO group, such as hydrazide or aminooxy groups, may be attached (Hermanson, 2013).
3) *covalent EDC – NHS conjugation*: simple method, which is typically used for nanoparticles with carboxyl-functionalized surface. 1-Ethyl-3-(3-dimethylaminopropyl)carbodiimide (EDC) and N-hydroxysulfosuccinimide (sulfo-NHS) reactive groups are used for amide bond formation, linking the carboxylic acid on the nanoparticle to primary amines in the lysine residues of the antibody or protein (Asiaei et al., 2015).

2.4.4. Biocompatibility

In order to achieve biocompatibility, it is necessary to have an appropriate particle size, to obtain neutral charge and hydrophilicity of the particle surface. These conditions can be fulfilled by binding of neutral hydrophilic molecules on the particles (Kobayashi et al., 2014). Such surface functionalization also prevents aggregation of nanoparticles and opsonisation, leading to phagocytosis followed by the removal of nanoparticles from the bloodstream (Estephan et al., 2010). Polyethylene glycol (PEG) and its derivatives (Kim et al., 2008; Thierry et al., 2008), polycaprolactone (PCL) (Catauro et al., 2018), dextran (Adamiano et al., 2018) and zwitterions are often used as suitable molecules for biocompatibilization.

PEG, a polyethylene oxide (PEO) with molecular weights less than 20 000 g/mol, is a polymer, which is used in diverse applications. Due to its chemical stability, low toxicity, solubility in water and most of organic solvents, it is also widely used in

medicine (Webster et al., 2009). The technique, so-called "PEGylation", is a process in which PEG is bonded to another molecules and nanoparticles through crosslinkers. Prior to PEGylation, PEG must be activated by substitution of terminal –OH by a functional group that could react with an appropriate site in the molecule to be conjugated, maintaining its biological activity. PEG-NHS ester is one of the activated PEGs derivative used in practice for amine conjugation (Giorgi et al., 2014). Electrophilic functional group of the activated PEG further reacts with nucleophilic one ($–NH_2$) forming an amide cross-link (Fig. 15).

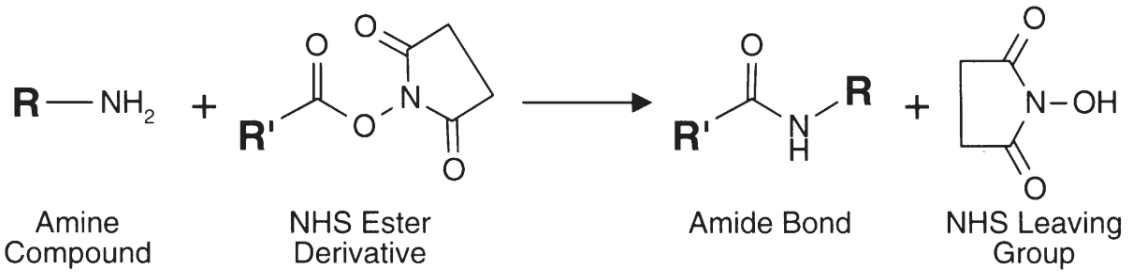

Fig. 15: General scheme of PEGylation. NHS or sulfo-NHS ester-containing reagents react with nucleophiles with release of the NHS or sulfo-NHS leaving group to form an acylated product (Hermanson, 2013).

2.5. Choice of the materials for nanocomposites design

From a wide range of the scintillating powder materials, LuAG:RE, YSO:RE and LSO:RE were chosen as a core of the nanocomposites for PDTX and bioimaging applications due to their chemical inertness, low toxicity, good luminescent properties, which can be tuned by various RE^{3+} dopants, and existence of the simple synthesis method (photo-induced precipitation, sol-gel).

Pr^{3+}-doping of LuAG host seems to be convenient for PDTX applications, because Pr^{3+} emission spectrum overlaps with absorption spectrum of PpIX both at Soret band (410 nm) and Q-bands; thus, important condition for effective energy transfer from donor (LuAG:Pr^{3+} core) to acceptor (PpIX) with subsequent PpIX excitation and $^1O_2$ production is capable of fulfillment. Ce^{3+} ions were used for doping of the LuAG and YSO/LSO hosts primary for cathodoluminescence bioimaging due to intensive luminescence of Ce^{3+} centers in green spectral region.

Prior to biofunctionalization, the surface of the nanoparticles was coated with amorphous silica shell to enhance chemical reactivity of the surface. This method of nanoparticles surface modification is simple and the most frequently used.

For the PDTX functionality, PpIX, widely used in conventional PDT and commercially available photosensitizer, was chosen as a photosensitizing agent for conjugation with surface-modified nanoparticles. For cathodoluminescence bioimaging, nanoparticles were conjugated with anti-FasL antibody to achieve specific binding to the trans-membrane proteins.

PEG was chosen as a material for providing biocompatibility of the prepared nanocomposites because of its chemical stability, low toxicity and presence of the simple technique for conjugation with the nanocomposite surface.

3. Experimental Part

3.1. Instruments and methods

3.1.1. X-ray diffraction (XRD)

X-ray diffraction (XRD) was used for identification of phase composition, structural characterization and crystallites size determination of the prepared samples.

XRD analysis is based on the constructive interference of monochromatic X-rays applying to a crystalline sample. Atoms in a crystal are arranged in a regular pattern and there is a smallest volume element (a unit cell) that fully describes the crystal by translation in three dimensions. The unit cell can be described by the length of three sides or vectors (*a*, *b*, *c*) and the angles between them (α, β, γ), which together represent the so-called lattice parameters.

In XRD method, X-rays are "reflected" from a set of parallel planes inside the crystal, which are located at a distance d_{hkl} (interplanar spacing) and uniquely determined by three integer indexes: h, k and l (Miller indices). The interfering waves will be in phase and constructive interference is produced only in few directions, determined by the Bragg's law:

$$n\lambda = 2d_{hkl}\sin\theta_{hkl} \quad (3)$$

where λ is the wavelength of primary X-ray beam, n is any positive integer, d_{hkl} is interplanar spacing and θ_{hkl} is the angle between the diffracted ray and the diffracting set of crystal planes. θ_{hkl}-value depends on the unit cell dimensions that are unique for every crystalline material. Therefore, XRD analysis allows identification of phases in the sample using crystallographic databases.

Among phase identification and characterization of powders and solids, XRD enables determination of average crystallite size, which is one of the reasons of the broadened peaks in the diffractograms. By application the Scherrer equation (4), the average nanoparticles crystallite size (*l*) can be determined as follows:

$$l = \frac{K\lambda}{\beta\sin\theta_{hkl}} \quad (4)$$

where β is a peak broadening as full width at half of maximum (FWHM) of intensity considering the Halder-Wagner approach (Halder and Wagner, 1966), and K is a shape factor that depends on the shape of crystallites. The Scherrer constant used for the calculations was K = 0.94 for spherical crystallites with cubic symmetry (Langford and Wilson, 1978). This method is applicable only for nanoparticles with crystallite size in the order of units of nanometers up to approximately 200 nm (Miranda and Sasaki, 2018).

The XRD measurements were performed using Rigaku MiniFlex 600 diffractometer (Fig. 16) equipped with Cu X-ray tube (average wavelength $K_{\alpha 1,2}$ = 0.15418 nm). High voltage and current settings used were 40 kV and 15 mA, respectively. The measurement was performed in continuous mode in the range of 10° – 80° 2θ with a collection speed 2°/min. The measured range was divided into intervals for data collection with a width equal to 0.02°. The collected data were evaluated in the PDXL2 program using International Center for Diffraction Data (ICDD) PDF-2 database, version 2013, and compared to the database standards data.

Fig. 16: Rigaku MiniFlex 600 diffractometer.

3.1.2. Dynamic light scattering (DLS)

Dynamic light scattering (DLS) is a non-invasive, well-established technique for measuring molecules and particles size distribution profile typically in the submicron region in a suspension. The Brownian motion of particles or molecules in suspension causes laser light to be scattered at different intensities. Analysis of these intensity fluctuations yields the velocity of the Brownian motion and hence the particle size using the Stokes-Einstein relationship. The method involves, that the size of the measured particles is of the same order as the wavelength of the scattered light.

DLS technique was used for determining the particles size of the prepared nanoparticles. DLS measurements were performed at room temperature with a Zetasizer Nano ZS (Malvern Instruments, Malvern, UK). The measurements were done in a glass cuvette with an optical path of 10 mm. The sample volume was approximately 1 mL. Cyclohexane was used as a medium for preparation of the suspensions.

The measurement was performed by Ing. Vojtěch Ledvina at the Department of Bioanalytical Instrumentation, Institute of Analytical Chemistry, Academy of Sciences of the Czech Republic.

3.1.3. Specific surface area (SSA) measurement

Specific surface area (SSA) measurements of the surface-modified nanoparticles were carried out using Monosorb MS-22 (Quantachrome Instruments, USA) rapid surface area analyzer (Fig. 17). The apparatus utilizes a modified BET equation for extremely rapid, single point determinations of surface area.

Fig. 17: Monosorb MS-22 surface area analyzer.

As a carrier gas, a mixture containing 30% of nitrogen and 70% of helium was used. The instrument provides the absolute value of the surface area of the sample as

the area of the desorption peak after sorption of the gas mixture on the surface at the temperature of 77 K provided by liquid nitrogen.

3.1.4. Thermal treatment

Thermal analysis of the samples was carried out using thermo-analyzer LABSYS Evo (SETARAM Inc., Caluire, France; Fig. 18A), which enables a simultaneous execution of thermogravimetry (TG) and differential thermal analysis (DTA) or differential scanning calorimetry (DSC). Thermal analysis can be performed under controlled vacuum, in air, reducing or inert atmosphere with maximum achievable temperature of heat treatment up to 1600°C (900 °C in reducing atmosphere). The measurements were carried out in a corundum crucible.

A vacuum furnace 0415 VAK (Clasic s. r. o.; Fig. 18B) was used for thermal processing of powdered materials. The furnace is equipped with the Clare 4.0 regulator, which enables to set a temperature, time of calcination and temperature gradient. The furnace is capable of incorporating a mild vacuum and calcination in inert or reducing atmosphere, which is allowed by the vacuum pumping system and gas input.

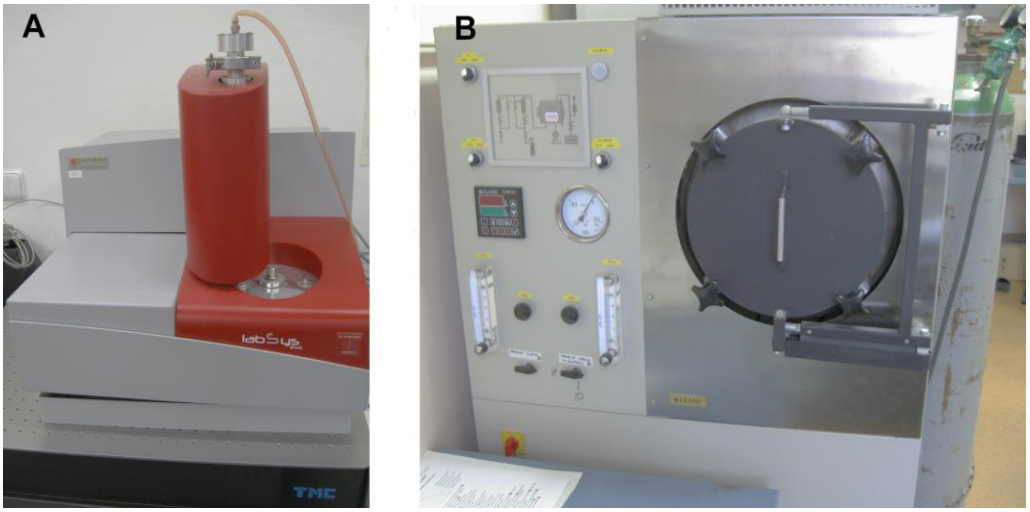

Fig. 18: LABSYS Evo thermal analysis platform (A) and 0415 VAK vacuum furnace (B).

3.1.5. Microscopy

To study morphological properties and topography of the samples surface, transmission electron microscopy (TEM) technique was used. TEM images of the prepared samples were obtained by the transmission electron microscope JEOL

JEM-3010 (JEOL Ltd., Tokyo, Japan) equipped with EDX detector (Oxford Instruments); high voltage acceleration is available up to 300 kV. TEM imaging of the powder samples was carried out by Ing. Ivo Jakubec, CSc at the Institute of Inorganic Chemistry, Academy of Sciences of the Czech Republic in Řež.

SEM imaging of the prepared powder samples under high energy CL beam excitation was performed by Mgr. Ondřej Lalinský at the Institute of Scientific Instruments, Academy of Sciences of the Czech Republic, using scanning electron microscope Magellan 400L (Thermo Fisher Scientific, USA). The microscope is equipped with Schottky emission gun and MonoCL4 Plus cathodoluminescence detector (Gatan, UK), which is able to capture ultraviolet (UV), visible and infrared (IR) light.

Cathodoluminescence bioimaging was acquired by Ing. Karel Klepárník CSc. and Ing. Vojtěch Ledvina at the Department of Bioanalytical Instrumentation, Institute of Analytical Chemistry, Academy of Sciences of the Czech Republic using Tescan MIRA3 and MAIA (Tescan, Brno, Czech Republic) scanning electron microscopes (SEM), and by Ing. Filip Dominec, PhD. at the at the Department of Optical Materials, Institute of Analytical Chemistry, Academy of Sciences of the Czech Republic using Philips/FEI XL30 (FEI Czech Republic, Brno, Czech Republic) SEM, equipped with a panchromatic cathodoluminescence (CL) detector. The accelerating voltage used for the acquisition was 10 kV. Due to sufficient conductivity of the measured materials, metal coating for the elimination of the charging artifacts was unnecessary.

Some of the prepared samples were also tested for immunolabeling at the fluorescence microscope by Ing. Karel Klepárník CSc. and Ing. Vojtěch Ledvina at the Department of Bioanalytical Instrumentation, Institute of Analytical Chemistry, Academy of Sciences of the Czech Republic. The nanocomposite-labeled cells (T-lymphocytes) were observed on the IX71 inverted fluorescence microscope (Olympus, Tokyo, Japan) using 100× magnification oil immersion objective and 460 – 495 nm excitation filter.

3.1.6. Luminescence measurements

Measurements of luminescent properties for the majority of the prepared samples was carried out by Ing. Lenka Procházková, PhD. and Ing. Vítězslav Jarý, PhD. at the Department of Optical materials, Institute of Physics of The Academy of Sciences of

the Czech Republic. Room temperature (RT) radioluminescence (RL), photoluminescence (PL) emission and decay curves were measured using the Mo X-ray tube (RL spectra; Seifert, 40 kV,15 mA), steady-state deuterium lamp (PL spectra) and nanosecond pulse nanoLED (PL decay curves) with emission wavelengths 281 nm, 339 nm, 370 nm, 389 nm and 455 nm as excitation sources. The detection part of the set-up was ensured by 5000M spectrofluorometer (Horiba Jobin Yvon, Palaiseau, France) equipped with a single grating monochromator and photon counting detector TBX-04. Both, RT RL and RT PL collected spectra, were corrected for the spectral dependence of detection sensitivity.

Photoluminescent excitation and emission spectra of the LuAG:Ce^{3+} nanopowder were acquired using a spectrofluorometer FluoroMax4 (Horiba Jobin Yvon, Palaiseau, France) equipped with PMT (photomultiplier) detector and steady-state xenon lamp as an excitation source (Fig. 19). The spectra were measured under excitation at 430 nm and emission at 500 nm.

Fig. 19: Horiba Jobin Yvon FluoroMax4 spectrofluorometer.

3.1.7. Solid-state nuclear magnetic resonance

Solid-state nuclear magnetic resonance (ss-NMR) spectra were measured at 11.7 T using a Bruker Avance III HD 500 US/WB (Bruker Corporation, Billerica, USA) NMR spectrometer equipped with a double-resonance 4-mm MAS (magic-angle spinning) probehead. The ^{29}Si cross polarization magic-angle spinning (CP/MAS) NMR spectra at

$\nu(^{29}\text{Si})$ = 99.325 MHz were acquired; spinning frequency was $\omega_r/2\pi$ = 5 kHz; contact time was 5 ms and number of scans was 8600 with a recycling delay of 1 s.

The ss-NMR spectra were collected by Ing. Libor Kobera, PhD. using equipment at the Institute of the Macromolecular Chemistry, Academy of Sciences of the Czech Republic.

3.1.8. UV irradiation

As a source of ultraviolet radiation for photochemical reactions, mercury low-pressure and medium-pressure gas-discharge lamps were used.

Four low-pressure mercury lamps (UV Technic Meyer, Germany) with 25 W power input were used for most of the experiments. The lamp provides monochromatic light with 253.7 nm emission wavelength (emission line around 184.9 nm does not pass through quartz glass lamp bulb). The low-pressure mercury lamps are a part of a photochemical set-up (Fig. 20), including 2 L cylindrical flask as a reactor, and a magnetic stirrer.

The photon flow for the medium-pressure mercury lamps set up was measured using ferrioxalate actinometry (Kuhn et al., 2004) and was evaluated to be $0.75 \cdot 10^{19}$ hv/s (Procházková, 2018).

Fig. 20: Photochemical set-up for irradiation using low-pressure mercury lamps.

The medium-pressure mercury lamp UVH 1016-S6 (UV Technic Meyer, Germany) was utilized for the second, continuously water-cooled photochemical reactor (2.5L sulfonation flask), shown in Fig. 21A. The medium pressure lamp has maximal power input 400 W and light output 115 W in UV region. The lamp is regulated via electrical ballast device (Fig. 21B), which enables regulation of the power input in the range from 120 W to 400 W (360 W was usually set).

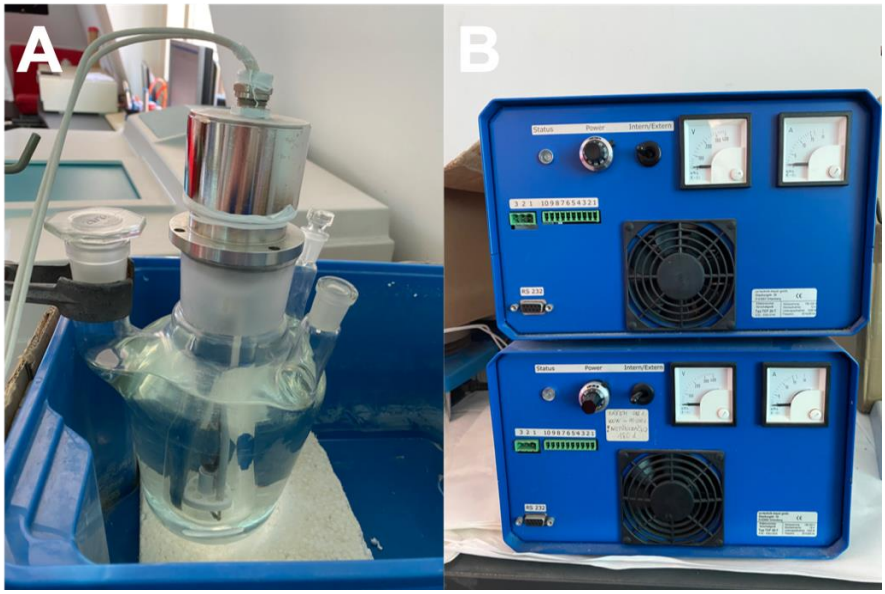

Fig. 21: Photochemical reactor with medium-pressure mercury lamp (A) and electrical ballast device for power input settings (B).

3.2. List of chemicals

For synthesis of nanomaterials, surface modification and biofunctionalization processes, the following chemical compounds listed in Table 3 were used as received. For solutions and suspensions preparation, common organic solvents, such as absolute ethanol, chloroform, tetrahydrofuran (THF) were utilized.

Table 3: List of chemicals.

chemical name	chemical formula	supplier	purity	molecular mass
lutetium nitrate hydrate	$Lu(NO_3)_3 \cdot xH_2O$	Sigma-Aldrich	99.999%	450.98*
aluminum nitrate nonahydrate	$Al(NO_3)_3 \cdot 9H_2O$	Sigma-Aldrich	99.997%	375.13
yttrium oxide	Y_2O_3	Sigma-Aldrich	99.999%	225.81
ammonium formate	$HCOONH_4$	Sigma-Aldrich	≥99.995%	63.06

cerium nitrate hexahydrate	$Ce(NO_3)_3 \cdot 6H_2O$	Sigma-Aldrich	≥99.99%	434.22
praseodymium (III, IV) oxide	PrO_{2-y}**	Koch-Light Laboratories	≥99.999%	-
tetraethyl orthosilicate (TEOS)	$Si(OC_2H_5)_4$	Sigma-Aldrich	≥99.0% (GC)	208.33
(3-aminopropyl)triethoxysilane (APTES)	$H_2N(CH_2)_3Si(OC_2H_5)_3$	Sigma-Aldrich	≥98.0%	221.37
sodium silicate solution	$Na_2O \cdot SiO_2$	Sigma-Aldrich	reagent grade	154.07
ammonium hydroxide solution	NH_4OH	PENTA	25 – 29%	35.04
ethyl acetate	$CH_3COOCH_2CH_3$	PENTA	p.a.	88.11
sodium hydroxide	NaOH	PENTA	p.a.	40.00
sodium chloride	NaCl	Carl Roth	≥99.5%	58.44
potassium chloride	KCl	PENTA	p.a.	74.56
disodium phosphate	$Na_2HPO_4 \cdot 2H_2O$	Sigma-Aldrich	p.a., buffer substance	177.99
monopotassium phosphate	KH_2PO_4	Sigma-Aldrich	≥99.0%	136.09
protoporphyrin IX (PpIX)	$C_{34}H_{34}N_4O_4$	Sigma-Aldrich	≥95.0%	562.66
triethylamine	$C_6H_{15}N$	PENTA	p.a.	101.20
carboxyethylsilanetriol disodium salt	$C_3H_6Na_2O_5Si$	Gelest Inc.	25% in water	196.14
2-(N-morpholino)ethanesulfonic acid (MES)	$C_6H_{13}NO_4S$	Sigma-Aldrich	≥99.0%	195.24
N-hydroxysulfosuccinimide sodium salt	$C_4H_4NNaO_6S$	Sigma-Aldrich	≥98.0% (HPLC)	217.13
N-(3-dimethylaminopropyl)-N'-ethylcarbodiimide (EDC)	$C_8H_{17}N_3$	Sigma-Aldrich	≥97.0%	155.24
monoclonal anti-FasL antibody	-	Sigma-Aldrich	purified Ig, buffered aqueous solution	-
tris-hydrochloride	$NH_2C(CH_2OH)_3 \cdot HCl$	Sigma-Aldrich	>99.0%	157.60

bovine serum albumin (BSA)	-	Sigma-Aldrich	≥98.0% Ig free	~66000
cetyltrimethylammonium bromide (CTAB)	-	Sigma-Aldrich	>99.0%	364.45
α, ω-di-succinimidyl(polyethylene-glycol) glutarate	-	Rapp Polymere	-	1218.16

** hydration x = 5 was assumed*

*** y is being uncertain*

3.3. YSO:Ce^{3+} and LSO:Ce^{3+} synthesis

YSO:Ce^{3+}(1%) and LSO:Ce^{3+}(1%) powder materials were prepared using room-temperature alkali-catalyzed sol-gel route. In a typical procedure, 5 mmol of $Y(NO_3)_3$ (for LSO preparation, $Lu(NO_3)_3 \cdot xH_2O$ was used as a precursor) and 0.1 mmol of $Ce(NO_3)_3 \cdot 6H_2O$ were dissolved in 50 mL of deionized water. $Y(NO_3)_3$ was prepared by dissolution of Y_2O_3 in an excess of concentrated nitric acid and subsequent evaporation of the reaction mixture and crystallization at room temperature.

Separately, ethanolic solution containing 50 mL of ethanol, and stoichiometric amount of TEOS with respect to Y^{3+} (5 mmol; 1.12 mL) was prepared. In the next step, both solutions were mixed and the excess (~10 mL) of NH_4OH stock solution was added by drops. The prepared suspension was stirred for approximately 24 hours (Fig. 22A). After that, the solution was centrifuged and the obtained product was dried in air at 40 °C to form a solid precursor of YSO:Ce or LSO:Ce (Fig. 22B).

The precursor was powdered in an agate mortar and a part of the sample was thermally treated up to 1400 °C using LABSYS Evo thermoanalyzer and, subsequently, changes in phase behavior with temperature were analyzed.

Finally, the product was obtained after calcination of the prepared precursor in air for 2 hours (10 °C/min) in a 0415 VAK vacuum furnace (Clasic) at the temperature determined from the measured thermogravimetric analysis.

The size of YSO:Ce or LSO:Ce particles was reduced by grinding in a ball mill and fractionalization. The fraction of small particles was obtained by dispersion of the grinded powder in ethanol, sedimentation, separation of the top phase, centrifugation at 5000 RPM (14.6 cm rotor radius, 4075 g RCF) and drying in air at 40 °C for 5 hours.

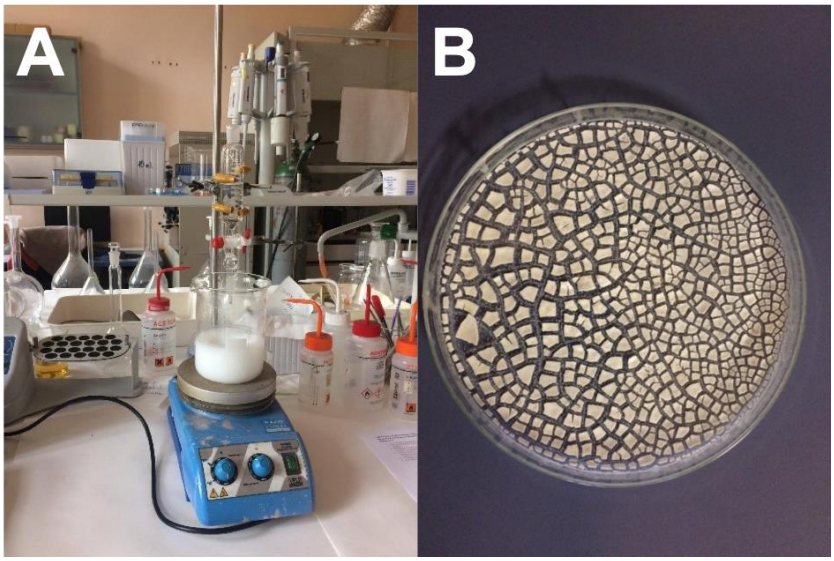

Fig. 22: Experimental set-up for YSO:Ce and LSO:Ce sol-gel synthesis (A) and precursor obtained after desiccation in air (B).

3.4. LuAG:Re^{3+} (RE = Pr^{3+}, Ce^{3+}) synthesis

LuAG:RE^{3+} (RE^{3+} = Pr^{3+}, Ce^{3+}) nanopowder was prepared using photo-induced method described earlier by Bárta et al. (Bárta et al., 2012). A dopant was chosen depending on the field of application.

An initial solution containing $3 \cdot 10^{-3}$ mol/L of lutetium nitrate hydrate, $5 \cdot 10^{-3}$ mol /L of aluminum nitrate nonahydrate, 0.1 mol/L of ammonium formate and $6 \cdot 10^{-6}$ mol /L of cerium nitrate hexahydrate, which corresponds to 0.2% concentration of Ce^{3+} ions, was prepared in deionized water in 2L volumetric flask. The solution was continuously stirred and irradiated for 4 hours in a water-cooled photochemical reactor. As a light source, a medium-pressure mercury lamp was used. The power input of the lamp was set to 360 W.

LuAG:Pr^{3+}(1%) nanoparticles were prepared via the same method as described above. UV irradiation was performed for 3.5 hours using four low-pressure mercury lamps. Final concentration of Pr^{3+} ions in the initial solution was $3 \cdot 10^{-5}$ mol /L. For Pr^{3+} doping, $Pr(NO_3)_3$ stock solution was prepared by dissolving of PrO_{2-x} in excess of concentrated nitric acid. The reaction proceeds according to the equation (5):

$$PrO_{2-x} + (4 - 2x)HNO_3 \rightarrow 2xPr^{3+} + (1 - 2x)Pr^{4+} + (2 + 2x)NO_3^- \quad (5)$$

The produced Pr^{4+} ions are unstable in the aqueous environment and subsequently transform to Pr^{3+} oxidation state. The resulting solution was diluted with distilled water in a volumetric flask.

After irradiation, the obtained gelatinous suspension was cooled down to room temperature and subsequently filtered from the reaction solution by microfiltration using 0.45 μm HAWP membrane filter. The prepared amorphous precursor was dried in air for 24 hours and then resuspended in ethanol in an ultrasonic bath for 3 hours. Finally, LuAG:Ce^{3+} (0.2%) or LuAG:Pr^{3+}(1%) nanopowders were obtained by calcination in 0415 VAK furnace at 1200 °C and 1000 °C, respectively. Thermal treatment of LuAG:Ce^{3+} precursor was performed in vacuum in order to avoid oxidation of Ce^{3+} to Ce^{4+}.

3.5. Surface modification by SiO_2 layer

3.5.1. Sol-gel method

The prepared LuAG:Pr^{3+} nanoparticles were coated by amorphous silica shell using modified sol-gel method described by Liu et al. (Liu et al., 1998). Calculations of the reactants' amount were made in order to obtain monomolecular layer of SiO_2 on the nanoparticle's surface. Prior to synthesis, 175 mg of LuAG:Pr^{3+} nanopowder was heated in vacuum furnace at 120 °C for 1 hour. After cooling down to room temperature in desiccator, the dried nanopowder was suspended in 40 mL of absolute ethanol in the ultrasonic bath for 1 hour.

The prepared suspension was placed on a magnetic stirrer and 20 μL of TEOS was added. After that, 6 mL of ammonium hydroxide solution (25 – 29%) was slowly added to the reaction mixture in a dropwise manner. The solution was left to react overnight under stirring to ensure maximum hydrolysis of TEOS, which is necessary to form amorphous silica shell.

After reaction, the silica-coated LuAG:Pr^{3+} nanoparticles (LuAG:Pr^{3+}@SiO_2) were rinsed 3× in deionized water and subsequently resuspended in ethanol in ultrasonic bath for 1 hour. The suspension of nanoparticles was left to dry in air at 40 °C for 24 hours.

3.5.2. Dense-liquid method

The technique used for surface modification by dense-liquid technique is a modified method used in Liu et al. work (Liu et al., 1998). 100 mg of LuAG:Pr^{3+} nanoparticles were dispergated in 90 mL of deionized water in ultrasonic bath for 1 hour. After that, pH of the suspension was adjusted to 9.5 using 1 mol/L NaOH solution, and the reaction solution was heated up to 90 °C on a heating plate. Separately, working water glass solution was prepared by addition of 44 μL of water glass stock solution (7.8 – 8.5% of Na_2O, 25.8 – 28.5% of SiO_2), corresponding to monomolecular layer of SiO_2, to 10 mL of deionized water. The prepared water glass solution was added drop-wise to the reaction mixture under vigorous stirring and holding the pH level at 9.5 within 1 hour. For the next 1 hour, the suspension was left to react at 90 °C and finally was cooled down to the room temperature. Silica-coated LuAG:Pr^{3+} nanoparticles (LuAG:Pr^{3+}@dl-SiO_2) were rinsed 2 – 3× in deionized water and dried in air at 40 °C. Quality of washing procedure was controlled by measuring pH (neutral) using pH indicators.

3.5.3. Combination of sol-gel and dense-liquid methods

Modification of nanoparticles surface by combination of sol-gel and dense-liquid methods was achieved by procedures described in sections 3.3.1. and 3.3.2., which were carried out in sequences.

In the first step, the surface of LuAG:Pr^{3+} nanoparticles was coated via sol-gel method using half of the initial amount of TEOS proportional to the weight of nanopowder. The obtained suspension was dried in air as usual. In the second step, dense-liquid was applied with the half of the initial amount of water glass working solution prepared by approach in section 3.3.2. To obtain final product, suspension containing LuAG:Pr^{3+}@sgdl-SiO_2 nanoparticles was dried in air for 24 hours.

3.5.4. Silica coating with surface carboxylation

The 25 mg of LuAG:Ce^{3+} nanoparticles were dispergated in 1 mL of $1 \cdot 10^{-2}$ mol /L phosphate buffer saline* (PBS; pH = 7.4). In the next step, 20 μL of carboxyethylsilanetriol disodium salt was added to the reaction suspension under

stirring. The reaction was proceeded for 4 hours at room temperature. Finally, functionalized LuAG:Ce^{3+}@SiO_2-COOH nanoparticles were washed in PBS through repeated cycles of centrifuging (12 000 g RCF, 5 min) and redispersion in PBS solution.

**Phosphate buffer saline (PBS) preparation:*

PBS solution was prepared by dissolving of 8.0 g of NaCl, 0.2 g of KCl, 1.781 g of $Na_2HPO_4 \cdot 2H_2O$ and 0.240 g of KH_2PO_4 in 800 mL of deionized water in 1 L volumetric flask. During dissolution, pH was controlled using pH meter (Jenway 3540). Before stirring was complete, the pH value was set to 7.4 by addition of NaOH water solution. Finally, the volumetric flask was filled to the mark with deionized water.

3.5.5. Mesoporous silica coating

To obtain mesoporous silica shell on the LuAG:Ce^{3+} nanoparticles surface, functionalization was performed using the modified procedure described earlier (Kim et al., 2008). The 100 mg of LuAG:Ce^{3+} nanoparticles were dispersed in 5 mL of chloroform, and 50 mL of 0.055 mol/L solution of CTAB were added under stirring. The mixture was reacted for 30 min. For evaporating chloroform, the temperature was increased to 60°C. The resulting solution was added to 450 mL of deionized water with addition of 3 mL of 2 mol/L NaOH solution and the mixture was heated up to 70 °C. In the next step, 5 mL of TEOS, 25 mL of ethyl acetate and 500 µL of APTES were put into reaction solution in a dropwise manner. After 2 hours of reaction, the obtained surface-modified nanoparticles were 3× washed with ethanol to remove the unreacted species and then redispersed in 20 mL of ethanol.

To remove CTAB molecules from the pores, the nanoparticles were reacted for 3 hours with 400 µL of concentrated HCl. In the end, LuAG:Ce^{3+}@mesoSiO_2 nanoparticles were washed with ethanol several times and dried in air.

3.6. Biofunctionalization

3.6.1. Protoporphyrin IX conjugation

Silica-coated LuAG:Pr^{3+}@SiO_2 nanoparticles were conjugated with protoporphyrin IX (PpIX) molecules using modified procedure described earlier by

Nowostawska et al. (Novostawska et al., 2011). In this method, the functional amino groups are first attached to PpIX and then the $(NH_2)_n$-PpIX molecules are conjugated with the surface of silica-modified nanoparticles (Fig. 23).

100 mg of PpIX were dissolved in 20 mL of tetrahydrofuran (THF). Subsequently, 132 µL of N-(3-dimethylaminopropyl)-N'-ethylcarbodiimide (EDC) were added, and the solution was stirred for 3 hours at 0 °C in a cooling bath under N_2 inert atmosphere. Then, 83 µL of APTES in 10 mL of THF were added to the mixture at 0 °C, and the reaction proceeded for the next 8 hours at room temperature.

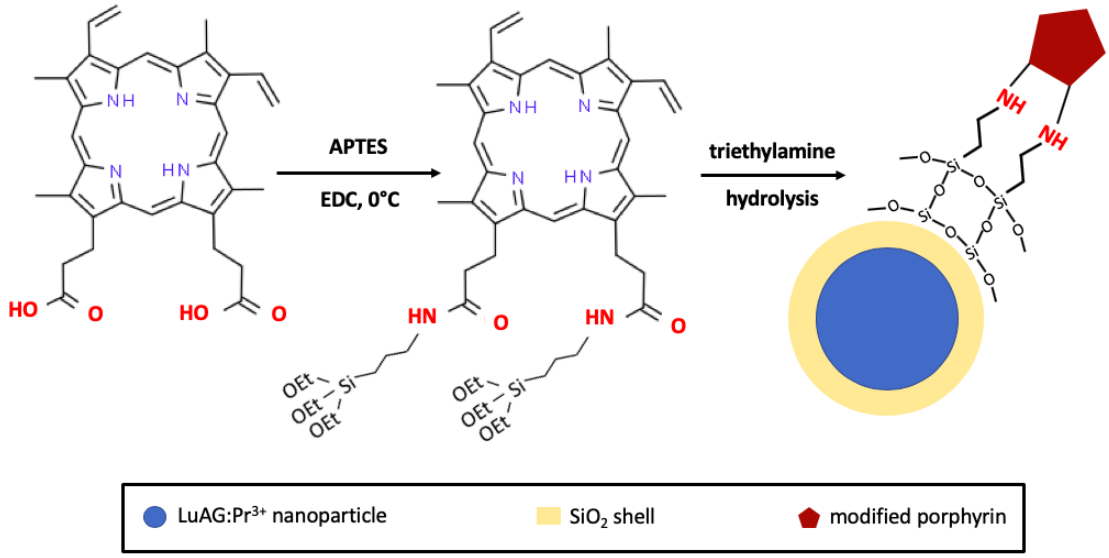

Fig. 23: Schematic illustration of principle of the nanoparticles conjugation with protoporphyrin IX molecules.

100 mg of LuAG:Pr^{3+}@SiO_2 nanopowder and 300 µL of triethylamine were added to the prepared solution and the suspension was left to react under stirring for 24 hours. The product was obtained after 10 min centrifugation at 5000 RPM (14.6 rotor radius, 4075 g RCF) and several washing processes with THF to remove unreacted PpIX. Finally, LuAG:Pr^{3+}@SiO_2-PpIX biofunctionalized nanoparticles were dried in air at 40 °C.

3.6.2. anti-FasL antibody conjugation

A 100 µL of LuAG:Ce^{3+}@SiO_2-COOH nanoparticles suspension was centrifuged (12 000 g RCF, 5 min), washed in deionized water and resuspended in 1 mL of 0.1 mol/L MES buffer (pH = 5.5). Then, 0.5 mL of solution, containing $1 \cdot 10^{-2}$ mol /L of

N-hydroxysulfosuccinimide sodium salt, $4 \cdot 10^{-3}$ mol /L of EDC in 0.1 mol/L MES buffer, was added to the nanoparticles suspension and incubation proceeded at the room temperature during stirring for 15 min.

After centrifugation and several washing processes with $1 \cdot 10^{-2}$ mol /L PBS, the nanoparticles were again resuspended in 1.5 mL of PBS. Subsequently, 50 μL of monoclonal anti-FasL antibody solution with a concentration of 1 mg/mL was added. The reaction solution was stirred for 2 hours at room temperature, then centrifuged and washed with PBS. For blocking the free carboxyl groups, the antibody-biofunctionalized nanoparticles were reacted for 1 hour with a solution of $40 \cdot 10^{-3}$ mol /L tris-hydrochloride with the addition of 0.05% of bovine serum albumin (BSA). Final nanocomposite LuAG:Ce^{3+}@SiO_2-anti-FasL was obtained after multiple washing steps in the solution of PBS with 1% of BSA. The suspension of biofunctionalized nanoparticles was stored in a fridge at 4 °C.

3.6.3. Biocompatibilization with polyethylene glycol

To provide biocompatibility of LuAG:Ce^{3+}@mesoSiO$_2$ nanoparticles, the silica-coated nanoparticles were conjugated with polyethylene glycol (PEG) polymer molecules. 30 mg of α,ω-di-succinimidyl(polyethylenglycol) glutarate was added to the 20 mL of ethanolic suspension containing 21 mg LuAG:Ce^{3+}@mesoSiO$_2$ nanoparticles, and the reaction proceeded at 40 °C for 3 hours. For removing the excess of PEG-precursor, LuAG:Ce^{3+}@mesoSiO$_2$-PEG nanocomposites were washed in sequence with ethanol and deionized water. Finally, the nanopowder was obtained after drying in air for 16 hours.

3.7. Singlet oxygen detection

Aminophenyl fluorescein (APF; Invitrogen™) commercial probe was used for the singlet oxygen generation detection. 100 μL of APF was added into 2 mL of ethanol suspension containing 15 mg of LuAG:Pr^{3+}@SiO_2-PpIX nanoparticles. X-ray tube with Cu-anode (40 kV voltage, 15 mA current, $K_{\alpha 1,2}$ = 0.15418 nm average wavelength) was used for irradiation. The samples were irradiated in polypropylene cuvette for 1 hour and 2 hours. Because APF probe reacts both with singlet oxygen and OH radicals

(Price et al., 2009), the measurement with addition of 2.5 mL of $10 \cdot 10^{-3}$ mol/L ethanolic solution of NaN_3 as a specific $^1O_2$-quencher (Bancirova, 2011) was performed. Subsequently, their photoluminescence spectra were collected in a quartz cuvette.

3.8. Sample preparation for fluorescence microscopy

T-lymphocytes in phosphate buffer were mixed with nanoparticles and antibody bioconjugate (LuAG:Ce^{3+}@SiO_2-anti-FasL)and incubated overnight at 4 °C. The next day, the cells were repeatedly centrifuged (2000 RCF, 5 min) and washed with PBS to remove the unbound nanoparticles and eventually fixed with 4% formaldehyde in PBS and washed again with PBS. After that, the labeled cells were observed in the fluorescence microscope.

4. Results and Discussion

4.1. YSO:Ce^{3+} and LSO:Ce^{3+} powders

YSO:Ce^{3+} and LSO:Ce^{3+} powders were prepared as potential materials for core of the nanocomposites for both PDTX and bioimaging applications, because their bulk counterparts show desired optical properties, such as high luminescence intensity with wide emission band between 350 – 550 nm (Knoll, 2010), which is able to match with the Soret band of PpIX.

4.1.1. Structural properties

Precursors for YSO:Ce^{3+} and LSO:Ce^{3+} powders were prepared using sol-gel method carried out at room temperature conditions. Simultaneous thermogravimetry (TG) and differential thermal analysis (DTA) were performed to determine temperature conditions leading to crystallization of YSO or LSO phases. Both DTA curves in Fig. 24 and Fig. 25 show an exothermic peak at about 300 °C, which corresponds to the decomposition of residual ammonium nitrate. Complete removal of nitrates was detected near 400 °C. A band occurring around 550 °C (Fig. 24) is caused by an unidentified exothermic process, presumably due to crystallization of an intermediate product.

In Fig. 24, initial information of the YSO phase was observed at 1040 °C and subsequently at 1300 °C. The observed temperatures correspond to the formation of monoclinic X1-type and monoclinic X2-type YSO, respectively (Ito and Johnson, 1968). The DTA curve for LSO (Fig. 25) shows crystallization of A-LSO at 1050 °C, followed by a phase transition to B-LSO, which was formed at 1150 °C (Yun et al., 2009). Detailed visualization of crystallographic types of A-LSO and B-LSO, and comparison of the lattice parameters for both modifications of YSO and LSO was mentioned in Section 2.4.1.2.

Structural properties of the prepared powders were determined using XRD analysis. Fig. 26 presents diffractograms of the prepared YSO:Ce (A), A-LSO:Ce (B) and B-LSO:Ce (C). Diffraction patterns of the YSO:Ce sample are in good agreement with the ICDD PDF-2 record of Y_2SiO_5 (card No. 36-1476), which belongs to a monoclinic crystal structure with C2/c space group. Diffraction patterns of A-LSO:Ce and B-LSO:Ce powders correspond to the ICDD PDF-2 records of low-temperature Lu_2SiO_5 (card

No. 70-3281; $P2_1/c$ space group) and high-temperature Lu_2SiO_5 (card No. 70-9485; C2/c space group) modifications, respectively. In the B-LSO sample, a separate phase of bixbyite-type Lu_2O_3 was observed that could be caused by an excess of Lu with respect to its solubility in the LSO phase (Wang et al., 2009).

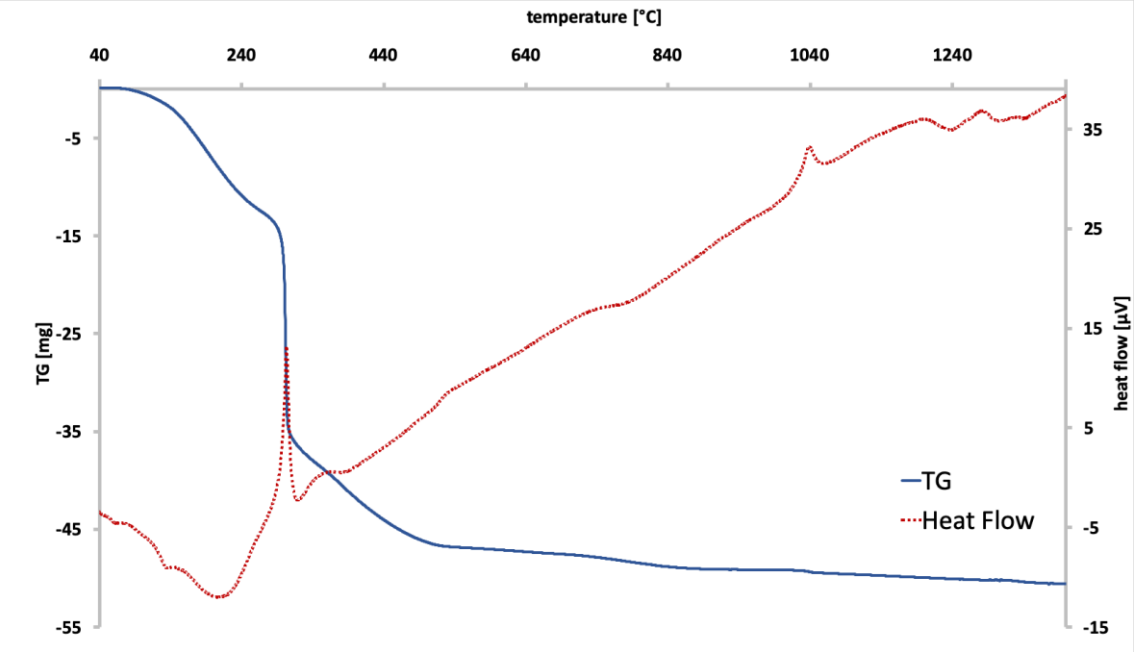

Fig. 24: Thermogravimetry (TG) and differential thermal analysis (DTA) curves of the solid precursor for YSO:Ce.

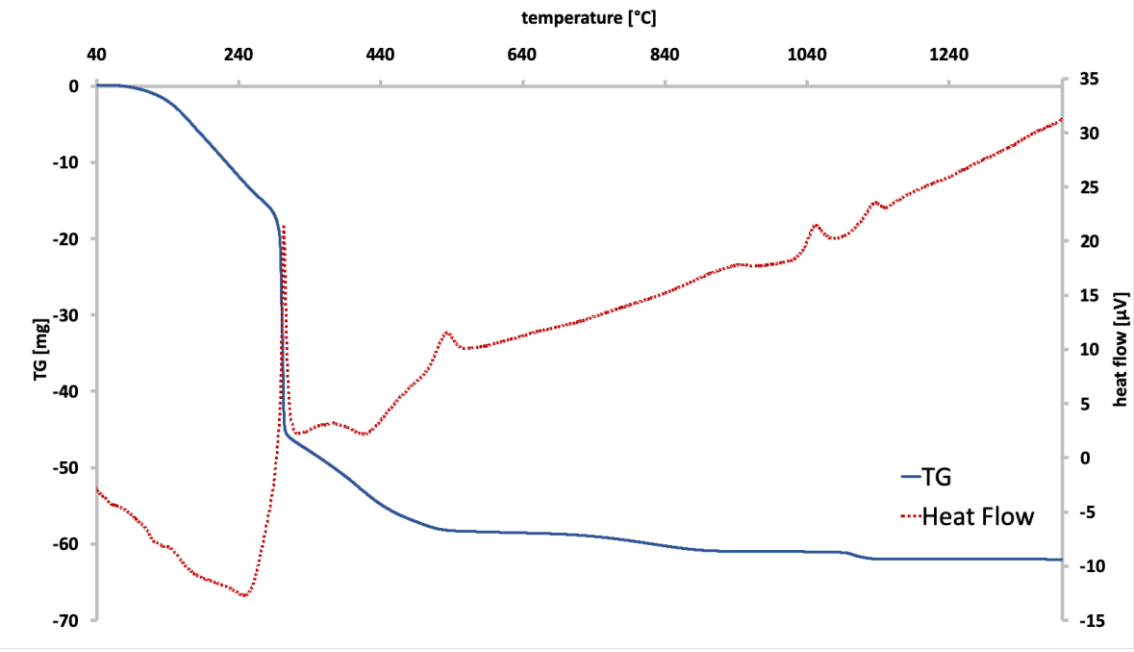

Fig. 25: Thermogravimetry (TG) and differential thermal analysis (DTA) curves of the solid precursor for LSO:Ce.

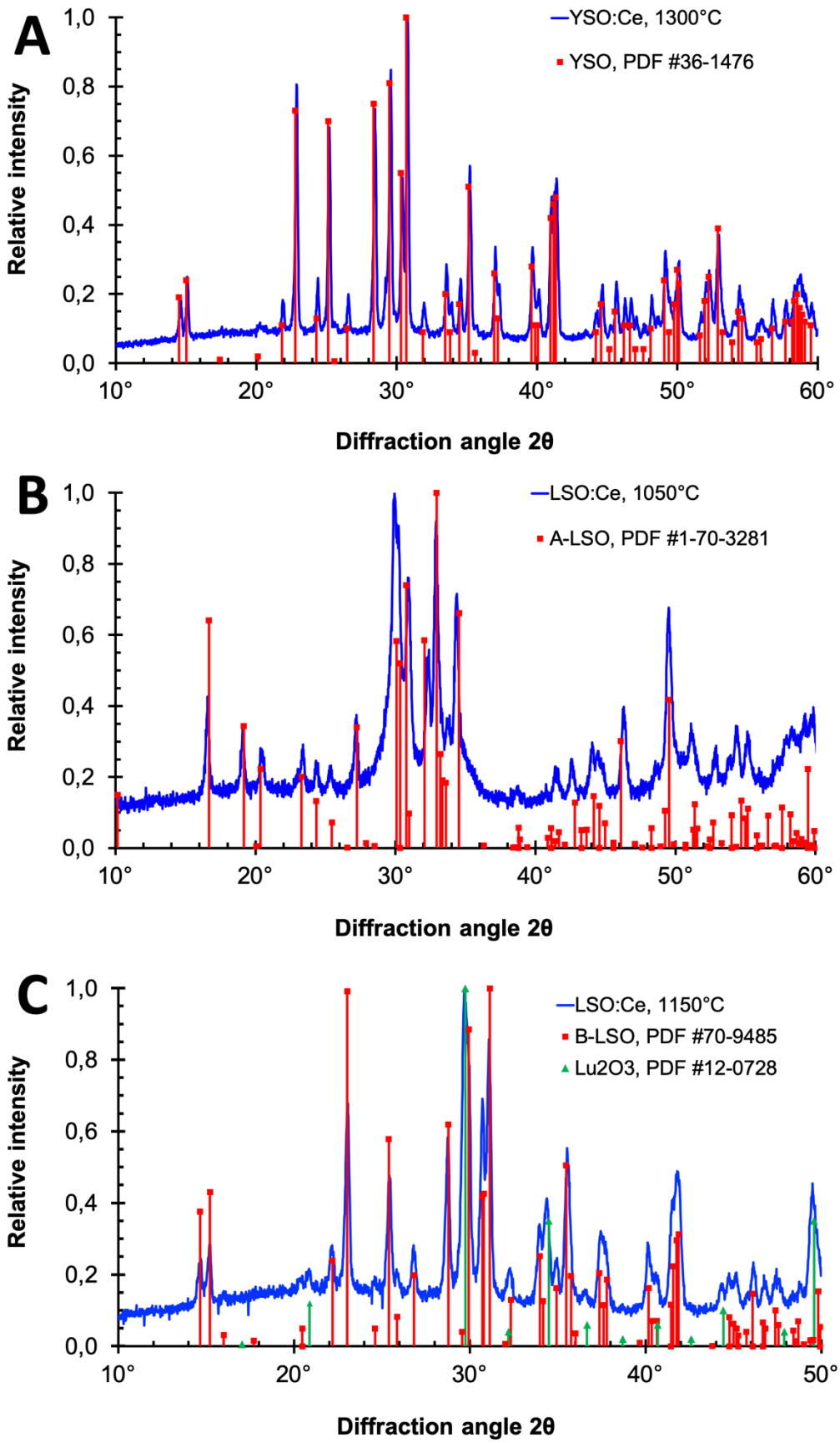

Fig. 26: Diffractograms of X2-type YSO:Ce (A), A-LSO:Ce (B) and B-LSO:Ce (C) compared to the records from the ICDD PDF-2 database.

The size of high-temperature modification of YSO:Ce^{3+} microcrystals was determined in the range of 100 – 1000 nm from TEM images, presented in Fig. 27. SAED diffraction patterns in Fig. 27D confirm the presence of crystalline oxyorthosilicates.

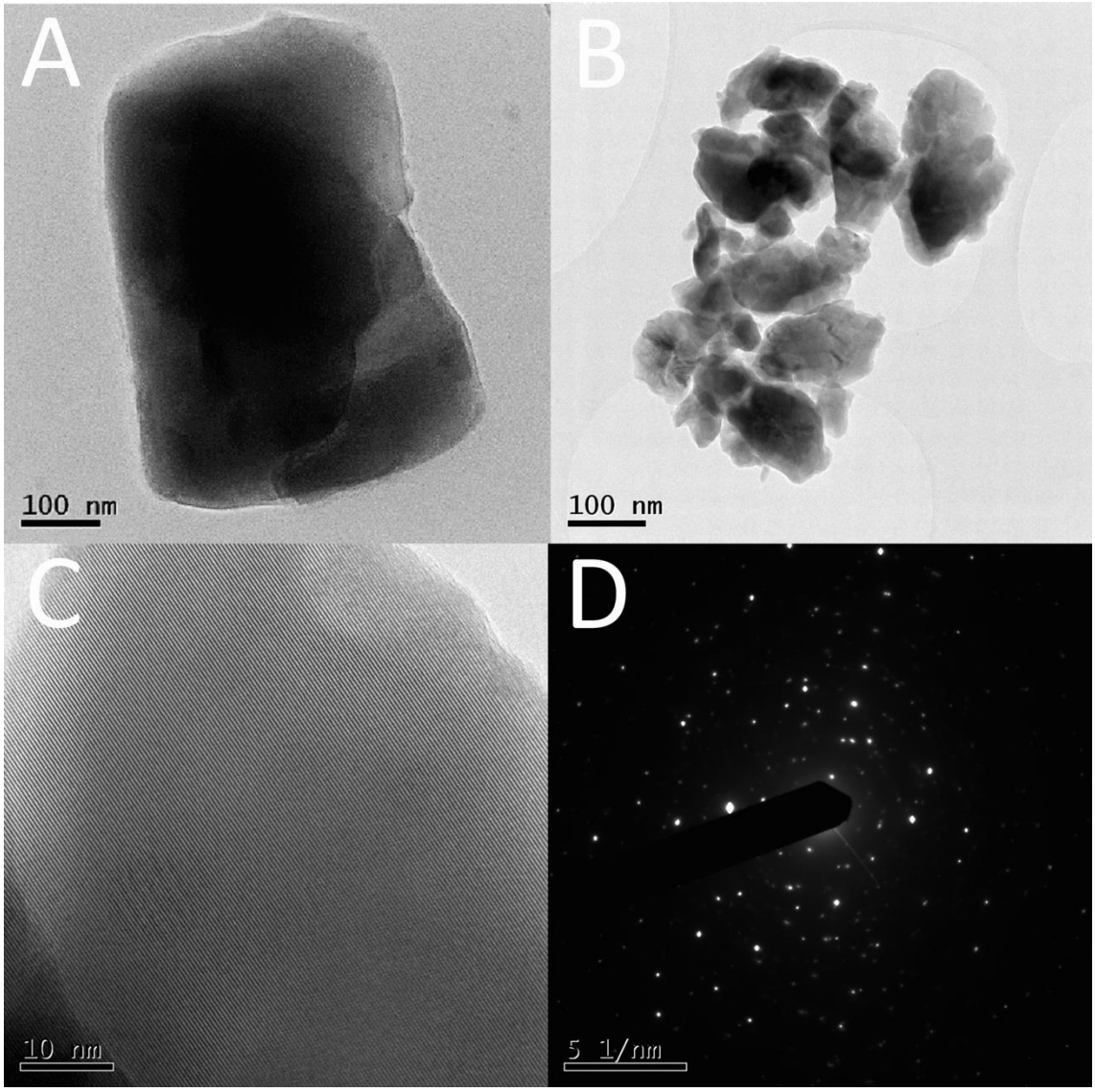

Fig. 27: TEM (A, B, C) and SAED (D) micrographs of the prepared X2-type YSO:Ce^{3+} sample treated at 1300 °C.

4.1.2. Luminescent properties

Room temperature (RT) radioluminescence (RL) spectra of the prepared samples presented in Fig. 28 and Fig. 29 show a typical broad emission band in the range of 350 – 600 nm caused by 5d – 4f transitions of Ce^{3+} ions. Both YSO:Ce^{3+} and LSO:Ce^{3+} samples show higher emission intensity, as compared to the powder $Bi_4Ge_3O_{12}$ (BGO) standard. Contrary to the prepared powder samples, BGO powder was not size-selected and was

used as a reference scintillator (due to its stability, low afterglow and average value of light yield). The BGO powder was measured in identical experimental conditions as the samples to quantitatively asses the steady-state luminescence intensity of different samples. The use of BGO powder in contrast to a single-crystalline BGO reflects the increased light scattering in powder samples and the need to have as comparable standard as possible. The radioluminescence measurements were made under identical conditions for all the samples including BGO; therefore, measured spectra can be matched to each other.

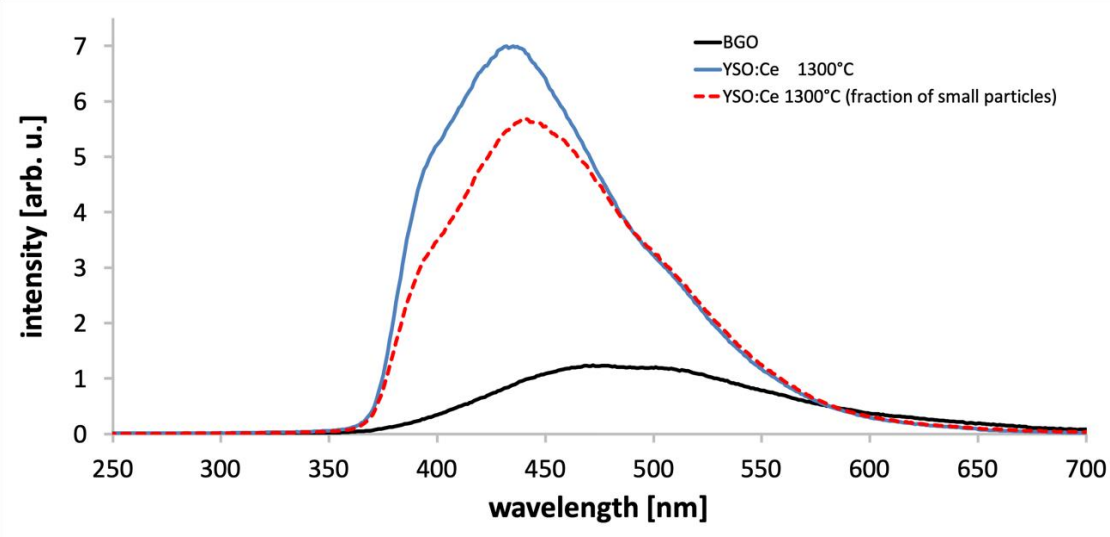

Fig. 28: RT RL of the as-prepared YSO:Ce^{3+} sample calcined at 1300 °C and the same sample after size reduction (fraction of small particles) compared to BGO powder standard.

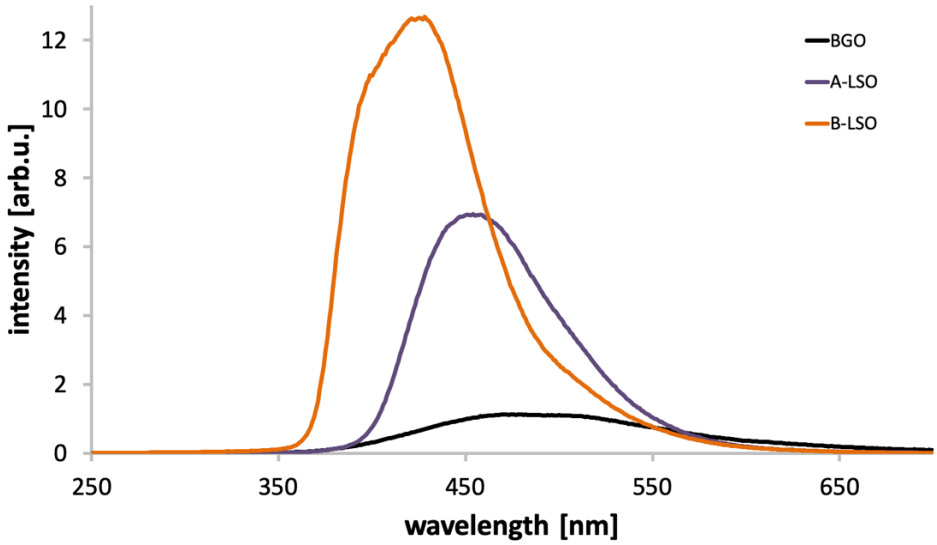

Fig. 29: RT RL spectra of the A-LSO:Ce^{3+} and B-LSO:Ce^{3+} samples compared to BGO powder standard.

Phase transition of A-LSO to B-LSO leads to an increase in luminescence intensity and shift of emission maximum to higher energies (Fig. 29), which is expected due to the changes in the Ce^{3+} coordination sphere resulting from different space groups ($P2_1/c$ and C2/c) (Blasse and Grabmaier, 1994). The increase in intensity is probably caused by the healing of defects at higher calcination temperatures.

Influence of particle size reduction by mill grinding method on the luminescence properties of the material was studied on the YSO:Ce^{3+} sample. Analysis of the RT RL spectra in Fig. 28 indicates that the emission intensity of small-particle fraction is almost not influenced by the size reduction process, as compared to the as-prepared YSO:Ce^{3+} material. The results were also correlated with photoluminescence (PL) decay curves measured under direct excitation in the 5d – 4f absorption transition of Ce^{3+} ions at 370 nm with monitoring of the decay at 430 nm. Both decay curves are well-approximated by a double exponential function with decay times 7.1 ns and 19.6 ns (as-prepared YSO:Ce; Fig. 30), and 6.2 ns and 23.2 ns (fraction of small particles; Fig. 31). The percentage contribution of each decay to the decay curve was calculated using following equation:

$$\%(t_1) = \frac{A_1 t_1}{A_1 t_1 + A_2 t_2} \quad (6)$$

where $\Sigma A_i \cdot \exp(-t/t_i)$ is the fit of the decay curve shown in Fig. 30 and Fig. 31. Taking into account a percentage contribution of the fast component for each sample (7.1 ns – 17%; 6.2 ns – 23%), it can be concluded, that the grinding process leads to the acceleration of the faster decay component. In addition, the measured results are inconsistent with YSO decays reported earlier by Auffray et al. for the bulk single crystals (50 – 70 ns; Auffray et al., 2015). The difference in decay times compared to bulk crystal may be caused by luminescence quenching due to defects on the surface of the prepared YSO:Ce^{3+} microparticles. This effect may be also caused by the calcination of the materials in air at high temperatures, which was shown to oxidize Ce^{3+} ions into Ce^{4+}. Ce^{4+} has been recently considered as a basis of alternate scintillation mechanism that should be faster than the usual Ce^{3+} emission (Blahuta et al., 2013).

Fig. 32 and Fig. 33 demonstrate changes in the decay time characteristics caused by the phase transition of LSO:Ce at higher temperatures of annealing. A-LSO decay curve (Fig. 32) exhibits both fast (2.2 ns – 34%) and slow (29.5 ns) components; in the

B-LSO decay (Fig. 33) two components (4.6 ns – 8%; 34.1 ns) were also found. However, direct comparison between decay curves of A-LSO and B-LSO is impossible, because the crystal structure of both materials is different (Gustaffson et al., 2001; Mueller-Bunz and Schleid, 1999). However, the determined decays are different from the 40 ns decays in LSO:Ce^{3+} single crystal (Pepin et al., 2004), which is assumed to be caused by the same mechanism mentioned for the YSO:Ce powder above.

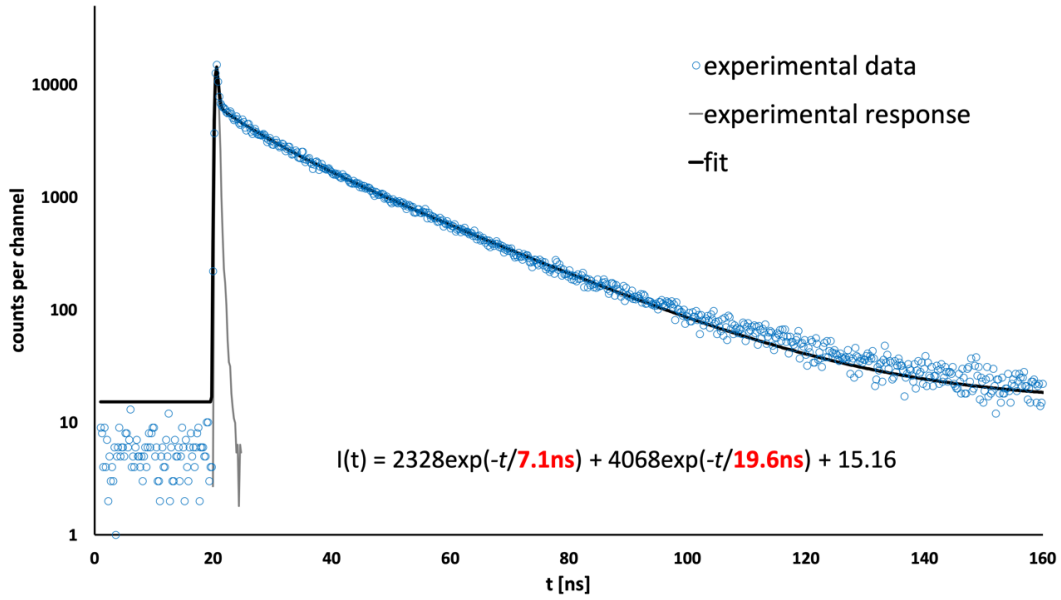

Fig. 30: RT PL decay of the 430 nm emission in as-prepared YSO:Ce^{3+} after excitation at 370 nm. Experimental data are approximated by a function I(t) given in the figure.

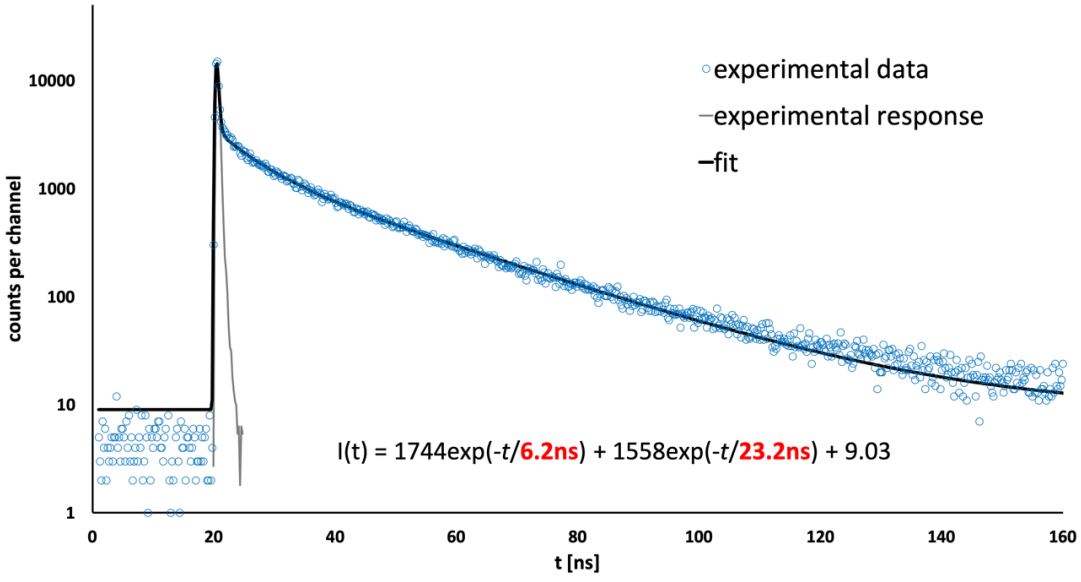

Fig. 31: RT PL decay of the 430 nm emission in a fraction of small particles of YSO:Ce^{3+} after excitation at 370 nm. Experimental data are approximated by a function I(t) given in the figure.

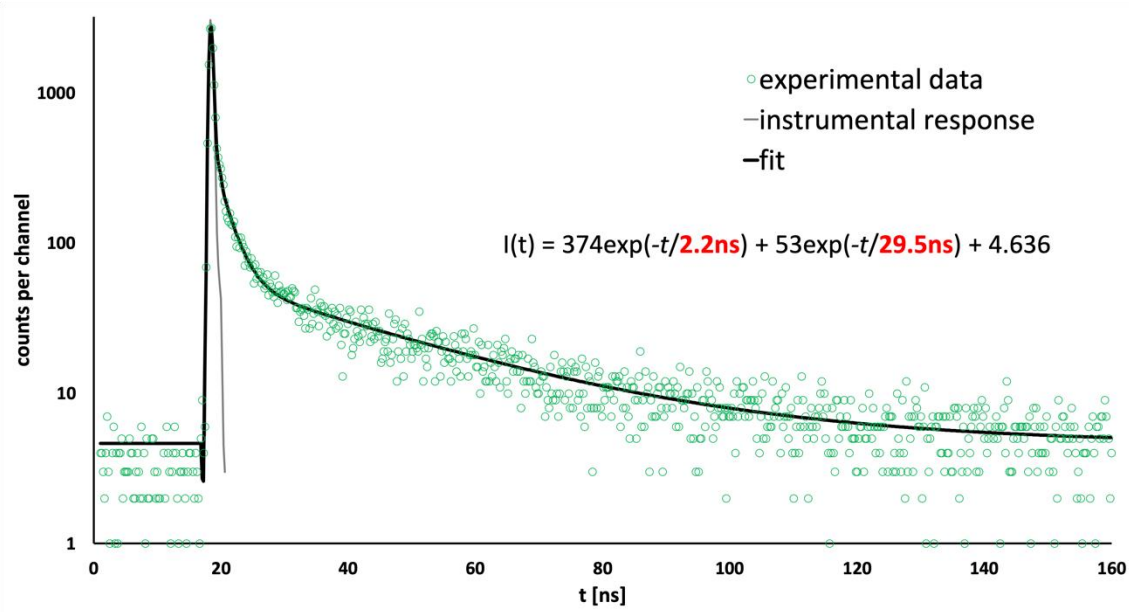

Fig. 32: RT PL decays of the 430 nm emission in A-LSO:Ce^{3+} after excitation at 339 nm. Experimental data are approximated by a function I(t) given in the figure.

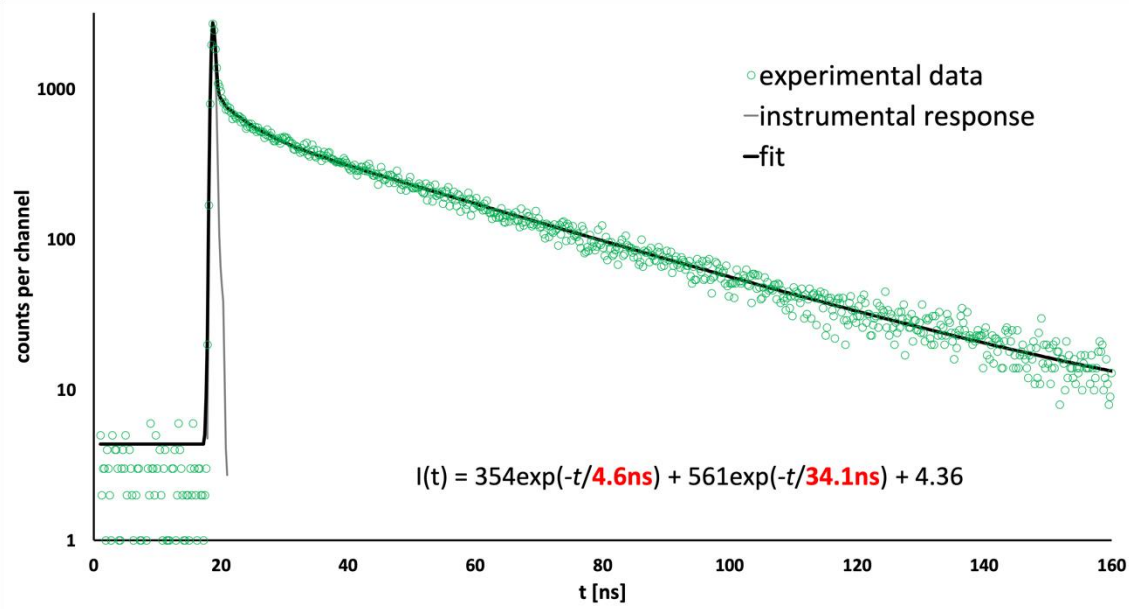

Fig. 33: RT PL decays of the 430 nm emission in B-LSO:Ce^{3+} after excitation at 339 nm. Experimental data are approximated by a function I(t) given in the figure.

Radioluminescence emission spectra of the prepared YSO:Ce and LSO:Ce materials show high intensity luminescence and good of emission band overlap with the Soret band in absorption spectra of the commonly used photosensitizers, making these scintillating materials good candidates as a core of luminescent nanocomposites for biomedical applications. However, for any *in vivo* application non-biodegradable

microparticles are unwanted due to their possible accumulation in the spleen and kidneys because of the size exclusion capability of those organs (Arruebo et al., 2009). On the other hand, observed reduction of the decay times, as compared to the bulk materials, provides an opportunity for their fast-timing applications. Ceramization process of the YSO:Ce^{3+}/LSO:Ce^{3+} powders or embedding of these materials in a suitable matrix can possibly make them good candidates for detector applications. Therefore, future detailed studies of properties of the YSO:Ce^{3+} and LSO:Ce^{3+} powders are needed.

4.2. NPs surface modification

Previous results shown, that YSO:Ce^{3+} and LSO:Ce^{3+} materials prepared via sol-gel route are not suitable for bioapplications due to their crystallite size in the micrometer range. For this reason, LuAG:Pr^{3+} nanoparticles prepared by photo-induced method were used as a luminescent core of the prepared nanocomposites for PDTX applications due to the average size of the nanocrystallites from 30 nm up to 100 nm (Bárta et al., 2012), depending on the treatment temperature of the precursor, suitable for bioapplications. Moreover, Pr^{3+} emission spectrum in LuAG host (Vondrášková et al., 2016) overlaps with the absorption spectrum of PpIX both in Soret band and Q-bands, which is an important requirement for effective radiative energy transfer for PS excitation and subsequent singlet oxygen production.

Prior to preparation of the luminescent nanocomposites for biomedical applications, a comparative study of three silica surface functionalization methods was made. LuAG:Pr^{3+} nanoparticles treated at 1000 °C were coated with amorphous silica shell using sol-gel, dense-liquid and combined two-step (sol-gel with subsequent dense-liquid) method.

Based on the assumption, that the silica layer formed under the sol-gel and dense-liquid processes should be porous or island-like (Liu et al., 1998), the measurement of specific surface area was performed. Increase in specific surface area of nanoparticles after application of sol-gel and dense-liquid technique was expected, whereas decrease of the value for the combined method is regarded probable. The measured surface areas are listed in Table 4.

Table 4: Comparison of the specific surface area for non-modified LuAG:Pr^{3+} and LuAG:Pr^{3+} modified by different methods.

coating method	specific surface area [m^2/g]
non-modified LuAG:Pr^{3+}	29.6 ± 0.4
sol-gel	34.8 ± 0.2
dense-liquid	33.5 ± 0.7
two-step coating	28.8 ± 0.1

The measurement results confirm the assumptions: sol-gel and dense-liquid methods lead to the increase of specific surface area value as compared to non-modified

LuAG:Pr^{3+} material. Combined method results in the formation of relatively smooth silica layer on the surface; thus, decrease in specific surface area occurs.

Surface texture can be also compared using TEM images (Fig. 34). Formation of amorphous silica layer is visible for sol-gel (Fig. 34B) and two-step coating (Fig. 34D). Dense-liquid leads to growth of non-homogeneous patch-like silica formations (Fig. 34C).

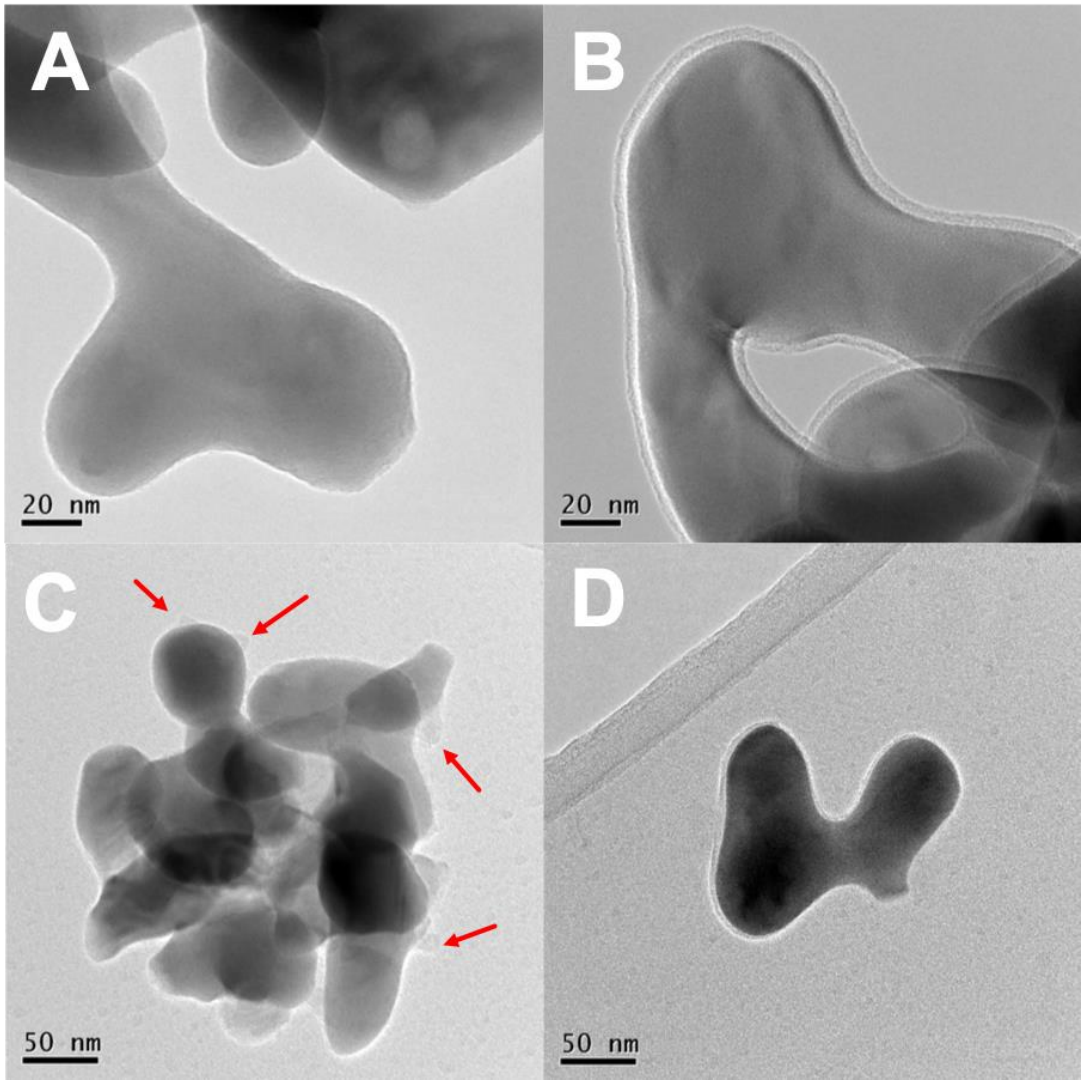

Fig. 34: TEM images of non-modified LuAG:Pr^{3+} (A), and silica-coated LuAG:Pr^{3+} using sol-gel (B), dense-liquid (C) and combined two-step (D) methods.

The results are also supplemented by RT RL measurements (Fig. 35) of the surface-modified samples in comparison with non-coated LuAG:Pr^{3+}. For all surface modification methods the shape of the emission spectra was kept. However, it was observed, that dense-liquid and two-step coating leads to sharp decrease in luminescence intensity with respect to emission of non-modified and sol-gel modified

LuAG:Pr^{3+} nanoparticles. This effect may be caused by formation of surface defects resulting in luminescence quenching.

Summing up the results of all measurements mentioned above, it was shown, that sol-gel technique for SiO_2 coating is more appropriate due to formation of continuous silica layer on the surface of nanoparticles in combination with maintained luminescence intensity. Sol-gel method for nanoparticles surface modification was used for further nanocomposites preparation in this work.

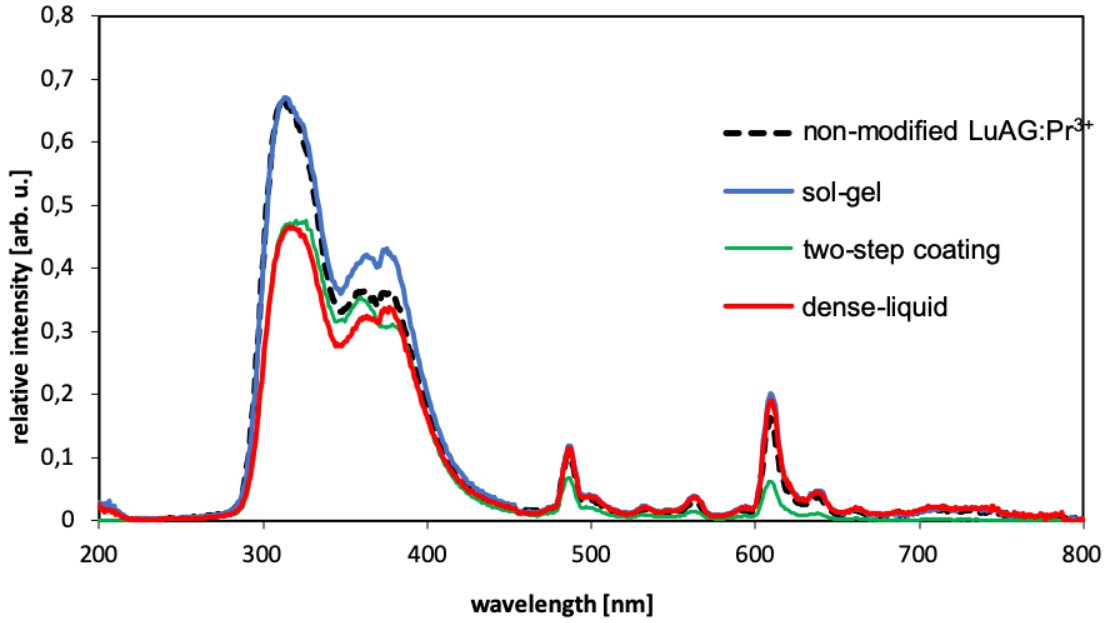

Fig. 35: RT RL spectra of non-modified LuAG:Pr^{3+} and silica-coated LuAG:Pr^{3+} using sol-gel, dense-liquid and combined two-step methods.

4.3. LuAG:Pr^{3+}@SiO_2-PpIX nanocomposite for PDTX

4.3.1. Structure of the nanocomposite

LuAG:Pr^{3+}@SiO_2-PpIX nanocomposite material for application in PDTX was prepared using a three-step process: synthesis of LuAG:Pr^{3+} using photo-induced method with subsequent calcination at 1000 °C, sol-gel technique for silica coating and biofunctionalization by PpIX conjugation.

Diffractograms of the prepared materials after each step of synthesis are illustrated in Fig. 36. All the diffraction patterns are in agreement with that of LuAG standard (dashed lines; card No. 01-073-1368) from ICDD PDF-2 database. Prepared nanoparticles correspond to cubic crystal structure and $Ia\bar{3}d$ space group. The crystallite size of the nanoparticles was also determined (Table 5).

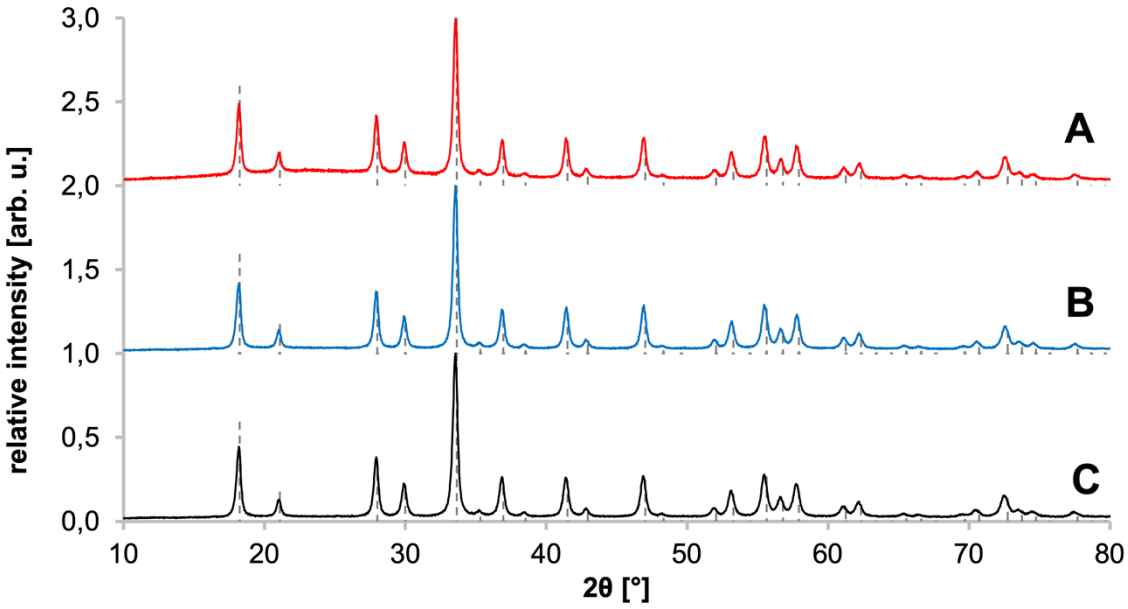

Fig. 36: Diffractograms of LuAG:Pr^{3+}@SiO_2-PpIX (A), LuAG:Pr^{3+}@SiO_2 (B) and LuAG:Pr^{3+} (C) samples compared with standard data from ICDD PDF-2 database (card No. 01-073-1368, dashed lines). Data are offset for clarity.

Table 5: Average size of the LuAG:Pr^{3+}, LuAG:Pr^{3+}@SiO_2 and LuAG:Pr^{3+}@SiO_2-PpIX nanoparticles.

sample	size [nm]
LuAG:Pr^{3+}	28 ± 2
LuAG:Pr^{3+}@SiO_2	29 ± 1
LuAG:Pr^{3+}@SiO_2-PpIX	30 ± 2

The absence of any additional peak in the diffractograms of the LuAG:Pr^{3+}@SiO_2 and LuAG:Pr^{3+}@SiO_2-PpIX samples confirms that the silica layer is amorphous, and crystallinity of the LuAG:Pr^{3+} core was not affected by surface modification and biofunctionalization processes.

The results of specific surface area measurements for non-modified (29.6 ± 0.4) m^2/g and for silica-modified (32.0 ± 0.2) m^2/g material support the assumption that LuAG:Pr^{3+} nanoparticles were successfully coated with the polysiloxane layer. This is further supported by amorphous layers on the surface of silica-modified and PpIX-biofunctionalized nanoparticles shown on TEM images in Fig. 37.

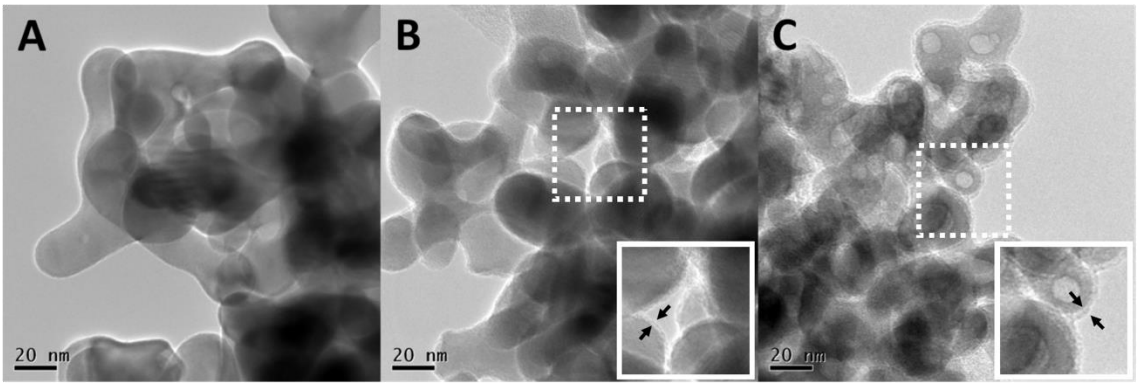

Fig. 37: TEM images of the as-prepared LuAG:Pr^{3+} (A), LuAG:Pr^{3+}@SiO_2 (B) and LuAG:Pr^{3+}@SiO_2-PpIX (C) samples.

The amount of PpIX contained in the prepared LuAG:Pr^{3+}@SiO_2-PpIX sample was determined using TG/DTA analysis. Fig. 38 shows TG/DTA curves of the LuAG:Pr^{3+}@SiO_2-PpIX sample thermally treated in air with temperature gradually increased up to 610 °C at the rate of 20 °C/min. The measured data are in good agreement with conclusions drawn from the thermogravometric analysis of PpIX and its derivatives published earlier in literature (Pop et al., 2013; Tostado-Plascencia et al., 2016). Initial mass loss from 30 °C to 358 °C is caused by breaking of the reactive bonds outside the pyrrole ring (–C=C– or >C=O). The second mass reduction from 358 °C to 547 °C could be assigned to pyrrole ring decomposition. Final mass lost beginning from 547 °C up to 610 °C could be associated with decomposition of the remaining parts with strong single bonds. Due to experimental conditions of heating in air, mass increase in TG curve at 358 °C was found, that was probably caused by the oxidation reactions of the studied sample with gases in the furnace atmosphere. Therefore, future TG/DTA experiments of PpIX decomposition

must be carried out in inert atmosphere with furnace purge and reaction gases exhaust (Pop et al., 2013). Total mass reduction of PpIX in the sample 1.83 g, corresponding to 17% of the PpIX content, was determined.

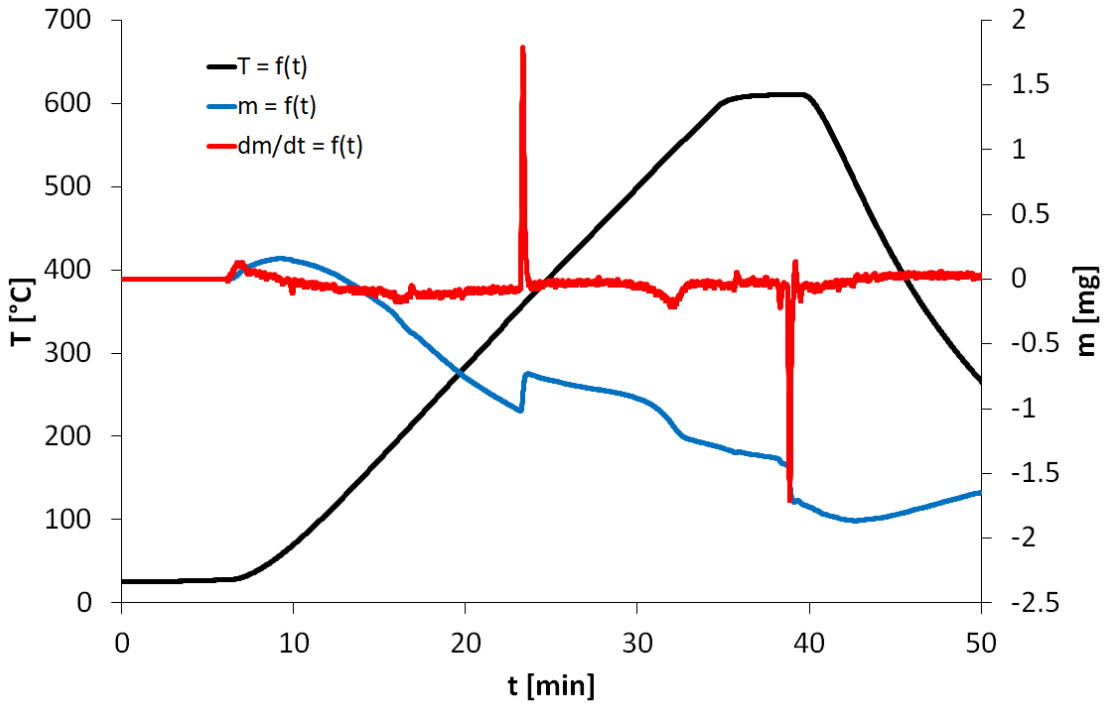

Fig. 38: TG/DTA analysis of the LuAG:Pr^{3+}@SiO_2-PpIX sample.

4.3.2. Luminescent properties and energy transfer

Room temperature radioluminescence spectra of the LuAG:Pr^{3+}, LuAG:Pr^{3+}@SiO_2 and LuAG:Pr^{3+}@SiO_2-PpIX samples are shown in Fig. 39. RT PL spectra manifest emission band associated with 5d – 4f transitions of Pr^{3+} ions in UV region peaking at 315 nm and 370 nm. Characteristic Pr^{3+} lines located in VIS region (480 – 650 nm) are related to the 4f – 4f transitions from the $^3P_0$ and $^1D_2$ levels to the $^3H_4$ and $^3H_6$ ground state levels of Pr^{3+} ions. Overall shape as well as intensity of the spectrum did not change due to surface modification. On the other hand, a dramatic decrease of the emission in LuAG:Pr^{3+}@SiO_2-PpIX spectra was observed compared to LuAG:Pr^{3+}@SiO_2 and LuAG:Pr^{3+} samples.

The absorption spectrum of PpIX overlaps with the emission spectrum of LuAG:Pr^{3+} in both the Soret band and Q-bands (Josefsen and Boyle, 2012). Therefore,

the likely scenario suggests that the quantitative changes in the RL PL spectra in region 350 – 400 nm are due to almost total absorption of energy emitted from LuAG:Pr^{3+} core by conjugated PpIX molecules. Moreover, such dramatic decrease of the RL intensity also indicates highly uniform layer of PpIX covering the silica-coated LuAG:Pr^{3+} core.

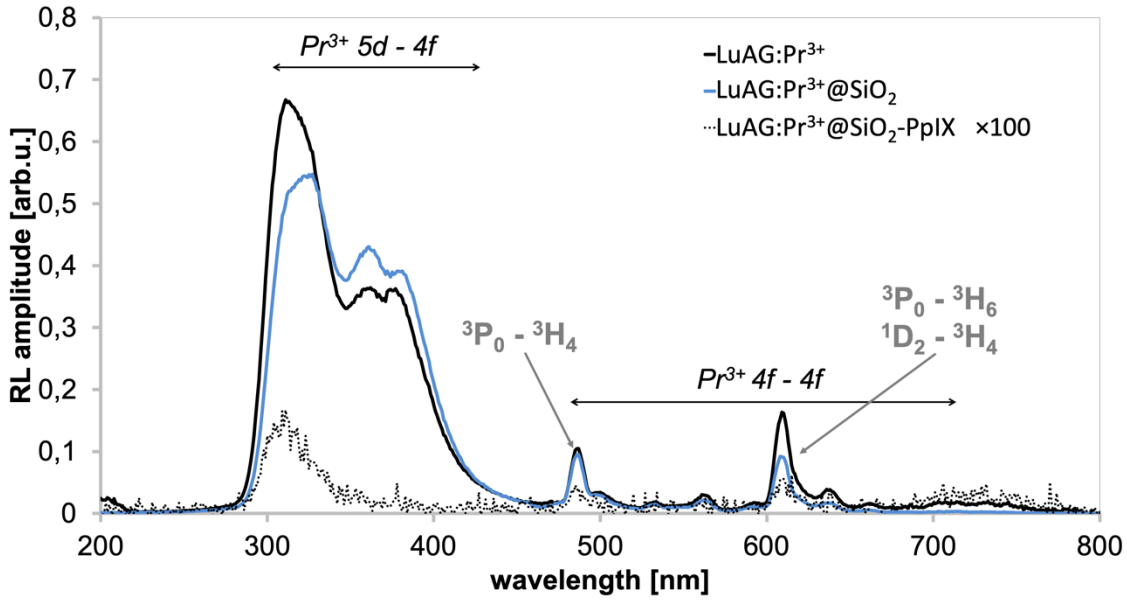

Fig. 39: X-ray excited RT RL spectra of the LuAG:Pr^{3+}, LuAG:Pr^{3+}@SiO_2 and LuAG:Pr^{3+}@SiO_2-PpIX samples.

Photoluminescence (PL) emission spectra of the samples are shown in Fig. 40. The spectra were measured to evaluate possible radiative energy transfer between LuAG:Pr^{3+} core and the attached PpIX molecules. Excitation of 250 nm directly at 4f – 5d absorption band of Pr^{3+} (LuAG:Pr^{3+}, LuAG:Pr^{3+}@SiO_2 and LuAG:Pr^{3+}@SiO_2-PpIX samples) and 410 nm at the Soret band of PpIX (LuAG:Pr^{3+}@SiO_2-PpIX sample) was utilized.

In RT PL spectra in Fig. 40 a broad emission band peaking at 307 nm is attributed to the 5d – 4f transition of Pr^{3+} ions. In the emission spectrum of LuAG:Pr^{3+}@SiO_2-PpIX sample (excited at 250 nm) two emission bands of PpIX at 633 nm and 690 nm (Silva et al., 2010) can be clearly identified. The emission of PpIX was also confirmed by excitation of the sample at the PpIX Soret band at 410 nm, so the similar emission profile can be observed in the range of 590 – 750 nm. Therefore, due to the qualitative changes observed in the PL emission spectra the presence of an energy transfer from LuAG:Pr^{3+} core to the PpIX outer layer is confirmed.

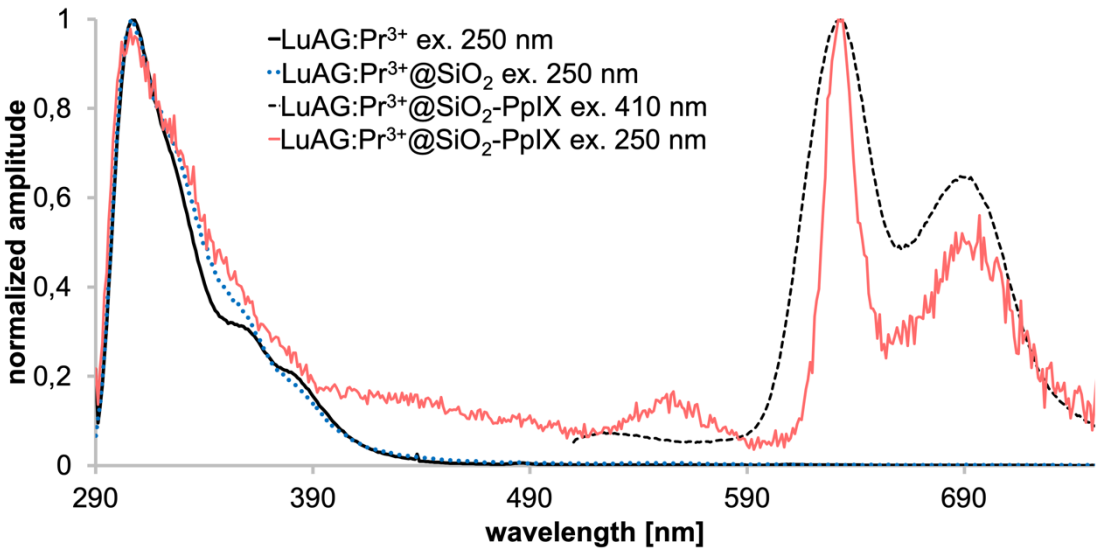

Fig. 40: Normalized to a maximum RT PL emission spectra under excitation λ_{ex} = 250 nm (LuAG:Pr^{3+}, LuAG:Pr^{3+}@SiO_2 and LuAG:Pr^{3+}@SiO_2-PpIX samples) and λ_{ex} = 410 nm (LuAG:Pr^{3+}@SiO_2-PpIX sample).

The decay curves shown in Fig. 41 were measured under excitation in the 4f – 5d transition of Pr^{3+} ions at 281 nm. The measured decay time of Pr^{3+} in LuAG:Pr^{3+} nanopowder was 25.5 ns (Fig. 41A) and it is significantly longer as compared to the 20 ns decay time of Pr^{3+} in LuAG bulk single crystal (Ogino et al., 2006). This result is accompanied by those obtained by monitoring the PpIX decay at 630 nm in the LuAG:Pr^{3+}@SiO_2-PpIX sample under excitation at 281 nm (Fig. 42A; 11.51 ns), and excitation in the Soret band at 389 nm (Fig. 42B; 12.8 ns).

The longer decay time of Pr^{3+} in LuAG:Pr^{3+} nanopowder in Fig. 41A as compared to the decay time of Pr^{3+} in LuAG bulk single crystals well-known for nanoscale materials, and it was earlier discussed by Bárta et al. and Vondrášková et al. (Bárta et al., 2012; Vondrášková et al., 2016). The decay time of Pr^{3+} is also slightly prolongated in LuAG:Pr^{3+}@SiO_2 sample (Fig. 41B; 27.5 ns) which is probably caused by the silica shell on the nanoparticle surface. At the same time, there is a small initial acceleration of the decay in Fig. 41B which might indicate some unwanted non-radiative energy transfer (ET) from Pr^{3+} centers toward defects in SiO_2 and consequently calls for optimization of the technological process. However, significantly faster decay of Pr^{3+} was observed in the PpIX-biofunctionalized sample (Fig. 41C; 4.34 ns and 14.4 ns) suggesting the non-radiative ET from Pr^{3+} donors toward PpIX acceptors.

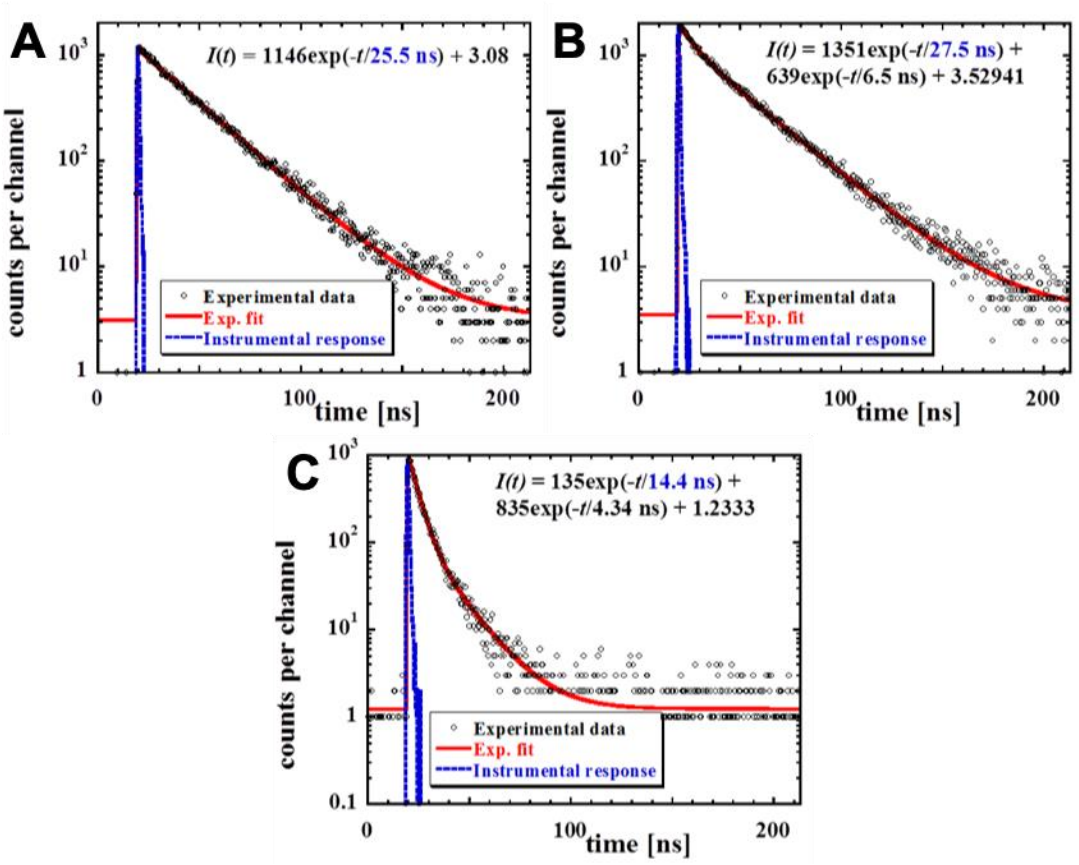

Fig. 41: RT PL decays of the 320 nm emission excited at 280 nm (4f – 5d absorption band of Pr^{3+}) in LuAG:Pr^{3+} (A), LuAG:Pr^{3+}@SiO_2 (B) and LuAG:Pr^{3+}@SiO_2-PpIX (C). Experimental data are approximated by a function I(t) displayed in the figures. Red line is a convolution of I(t) and instrumental response (blue line).

In Fig. 42, the direct excitation of PpIX (Fig. 42B) shows its own decay characteristics approximated by a double exponential function with decay times of 3.2 ns and 12.8 ns. Excitation of PpIX via Pr^{3+} center (Fig. 42A) does not cause any delay in the PpIX decay since 11.51 and 12.8 ns decay times in Fig. 42A and Fig.42B, respectively, can be considered identical due to low intensity of the signal (Fig. 42B) and consequently higher uncertainty in the determination of the decay time. Furthermore, these values are consistent with longer decay time of Pr^{3+} itself in Fig. 41C (14.4 ns). More precise phenomenological modeling of these decays using donor-acceptor interaction based on the dipole-dipole interaction exploiting e.g. classical Dexter model (Dexter, 1953) is disabled by not well defined thickness of SiO_2 layer, which is critical in such modeling. To summarize, the data obtained from the decay measurements confirm the presence of non-radiative energy transfer from the LuAG:Pr^{3+} core to PpIX outer layer, as a prerequisite for singlet oxygen generation and an application potential of the studied nanocomposite in PDTX.

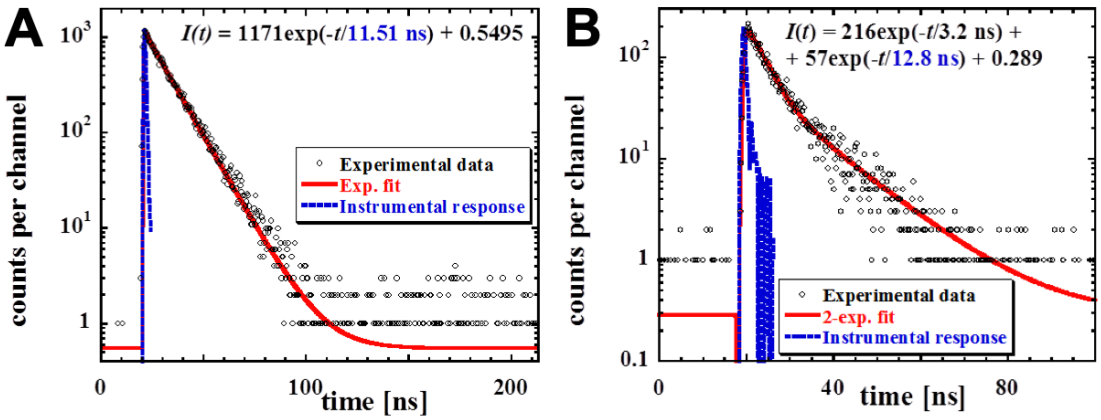

Fig. 42: RT PL decays of the 630 nm emission in LuAG:Pr^{3+}@SiO_2-PpIX. In (A) excitation at 281 nm, in (B) excitation at 389 nm. Experimental data are approximated by a function I(t) displayed in the figures. Red line is a convolution of I(t) and instrumental response (blue line).

4.3.3. Singlet oxygen detection

To demonstrate generation of singlet oxygen by X-ray irradiated LuAG:Pr^{3+}@SiO_2-PpIX nanocomposite, APF chemical probe was used. Reaction of APF with $^1O_2$ leads to formation of fluorescent molecule exhibiting an emission spectrum peaking at approximately 515 nm (Price et al., 2009). The photoluminescence spectra of LuAG:Pr^{3+}@SiO_2-PpIX + APF suspension were collected under excitation at 450 nm. The PL spectra were measured after X-ray irradiation for one hour and two hours. Duration of X-ray irradiation is proportional to the total X-ray dose absorbed by the suspension, which affects the amount of generated singlet oxygen. Increasing intensity of emission with increasing duration of irradiation indicates increased amount of singlet oxygen produced in the system.

The RT PL spectra of the X-ray irradiated suspension of LuAG:Pr^{3+}@SiO_2-PpIX nanocomposite with APF chemical probe (Fig. 43) manifest the formation of singlet oxygen due to which enhanced luminescence with maximum around 530 nm is observed. As a consequence of $^1O_2$ production, an increase on the signal at 515 nm in the spectra in Fig. 43 was expected. Broad bands observed in the range of 500 – 560 nm and 610 – 660 nm belong to the emission of the APF chemical probe and PpIX, respectively. A comparison of the spectra shows increasing PL emission intensity of the APF in the LuAG:Pr^{3+}@SiO_2-PpIX + APF irradiated for one hour and two hours with respect to the band observed in the irradiated sample of pure APF.

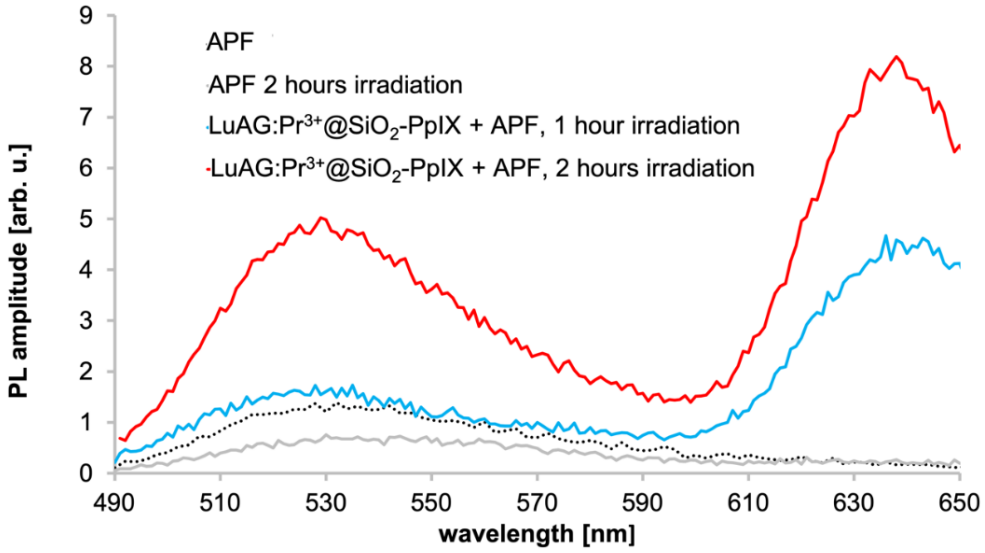

Fig. 43: RT PL emission spectra (λ_{ex} = 450 nm) of pure APF chemical probe (before and after X-ray irradiation) and LuAG:Pr^{3+}@SiO_2-PpIX + APF after X-ray irradiation.

To rule out the reaction of APF with OH radicals (possibly formed due to the radiolysis of a solvent), measurement with addition of NaN_3, which is a selective inhibitor of $^1O_2$, was performed. Quenching studies (Fig. 44) also confirm the presence of $^1O_2$ in the system and rule out the parasitic reaction of APF with OH radicals. It is obvious that the presence of NaN_3 leads to the quenching (Bancirova, 2011) of emission band in the range of 500 – 600 nm. The result further support the assessment that singlet oxygen has indeed been generated in the system.

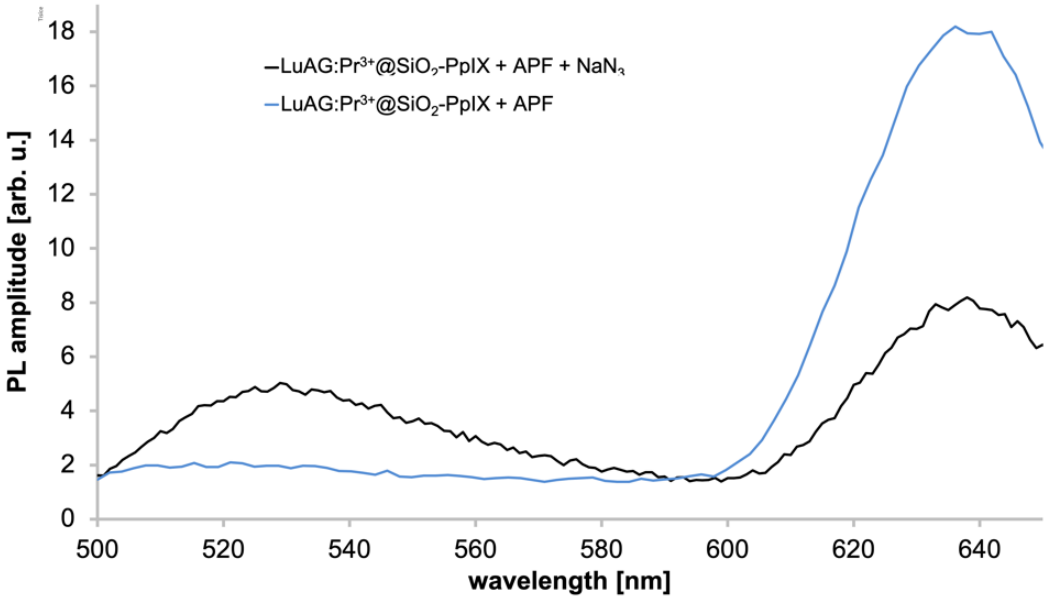

Fig. 44: RT PL. emission spectra (λ_{ex} = 450 nm) of the LuAG:Pr^{3+}@SiO_2-PpIX + APF and LuAG:Pr^{3+}@SiO_2-PpIX + APF + NaN_3 samples.

4.4. LuAG:Ce^{3+}@SiO_2-anti-FasL for CL bioimaging

Multimodal drug preparation concept assumes the use of several functionalities. The functionality studied in this chapter is focused on the concept of bioimaging of living cells using cathodoluminescence of the LuAG:Ce^{3+} scintillating nanoparticles attached to the cells membrane via sorption or bonding to the receptors using antigen-antibody interactions. For these experiments, Ce^{3+} ions were chosen for LuAG doping due to expected intensive luminescence of Ce^{3+} centers in LuAG host under CL beam excitation in green spectral part (Polisadova et al., 2019).

LuAG:Ce^{3+}@SiO_2-anti-FasL nanocomposite material was prepared in three steps: LuAG:Ce^{3+}(0.2%) luminescent core was prepared by the photo-induced method, silica coating with surface carboxylation with subsequent anti-Fas ligand (FasL) antibody attachment using EDC – NHS conjugation reaction was performed. The FasL is a transmembrane protein that triggers the programmed cell death (apoptosis) after binding to its receptor. It is expressed in larger amounts on the surface of T-lymphocytes that use it trigger apoptosis in infected or damaged cells (Andersen et al., 2006).

4.4.1. Structure and luminescent properties

The diffractogram of the prepared LuAG:Ce^{3+} nanopowder after calcination at 1200 °C is shown in Fig. 45. The measured diffraction patterns correspond to the standard data of $Lu_3Al_5O_{12}$ from the ICDD PDF-2 database (card No. 01-073-1368) with the cubic crystal structure and $Ia\bar{3}d$ space group. The solid phase is well-crystallized; the linear crystallite size was determined as (79 ± 8) nm. Generally, the size of the nanoparticles increases with the calcination temperature due to agglomeration and recrystallization. Luminescence intensity also increases with temperature due to the healing of crystalline defects until it reaches its maximum, and then it starts decreasing. For LuAG, such an optimal temperature was found to be 1200 °C by Bárta et al. (Bárta et al., 2012).

Size and shape of the LuAG:Ce^{3+} nanoparticles were also studied by SEM (Fig. 46). The average crystallite size corresponds to the results obtained from XRD measurement. LuAG:Ce^{3+} nanoparticles have rounded shape with a slight grain intergrowth, which can be expected due to relatively high calcination temperature (Bárta et al., 2012). The heat

treatment of the nanoparticles provides healing of the defects, which leads to the improvement of luminescence intensity, however, at the cost of increased particle size and agglomeration. Size of nanoparticles and their agglomeration influence the rapidity of interactions with the cell membrane and intracellular uptake. In general, nanoparticles with an average size of less than 50 nm are captured much faster due to mechanisms of the cellular uptake (Adjei et al., 2014).

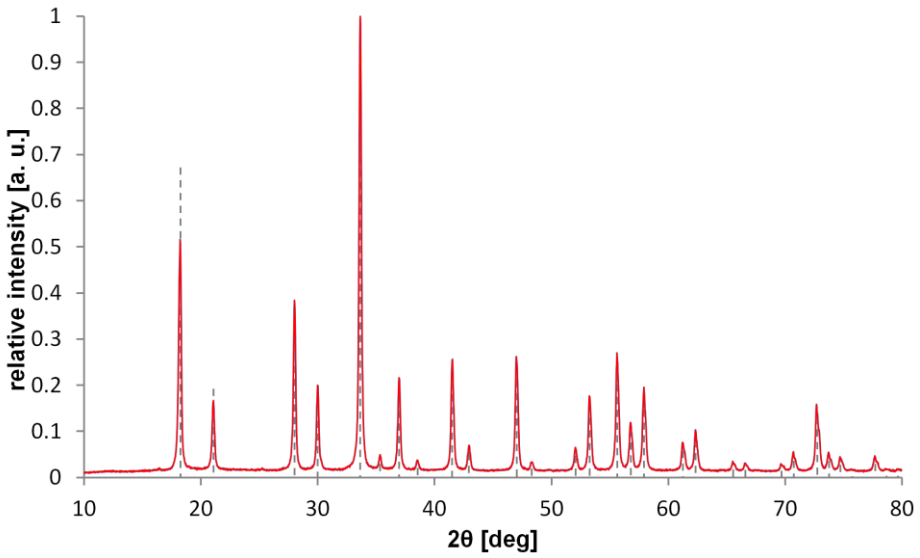

Fig. 45: Diffractogram of the prepared LuAG:Ce^{3+} nanoparticles (solid line) compared to the standard data (dashed lines; card No. 01-073-1368).

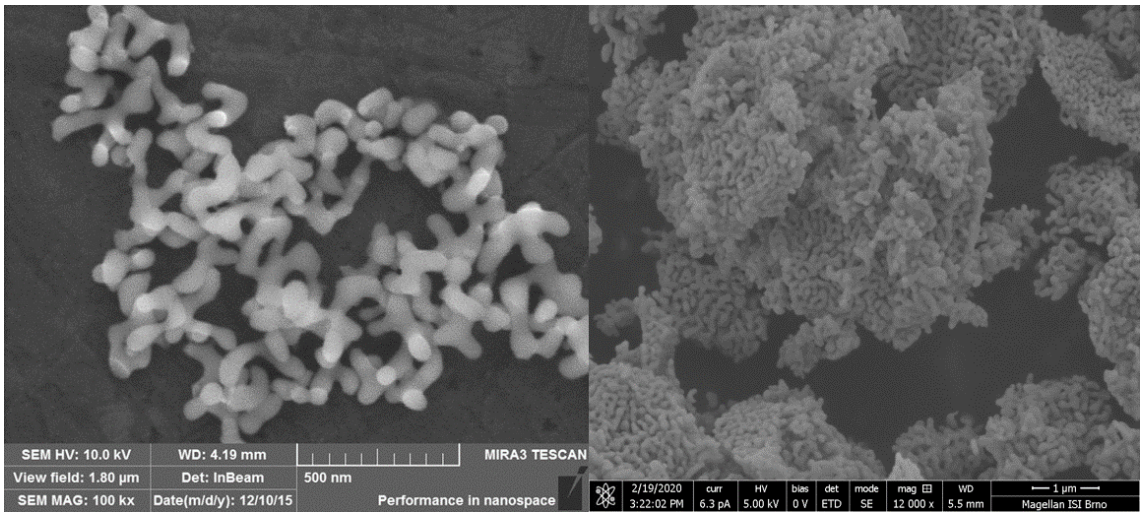

Fig. 46: SEM images of the LuAG:Ce^{3+} nanoparticles after vacuum calcination at 1200 °C.

Additionally, the prepared nanoparticles were characterized using the DLS method (Fig. 47). The volume size distribution profile was determined for the as-prepared LuAG:Ce^{3+} core (Fig. 47A) and for the nanoparticles after silica coating followed

by carboxylation (Fig. 47B). The average size of the nanoparticles prior to the silica surface modification is approximately 80 nm, which is in a good agreement with the results obtained from the XRD and SEM analyses. Surface modification by amorphous SiO_2 shell leads to an increase of the size to approximately 85 nm, indicating the successful formation of the peripheral silica layer. Without SiO_2 shell it would not be possible to bind –COOH groups to the nanoparticles surface, and thus, it would also be impossible to conjugate the nanoparticle with the antibody, and the whole composite would never get attached to the cell surface. In the present case, the thickness of the silica shell may be based only on the DLS measurements. A more precise evaluation of the SiO_2 thickness may be a focus of the future research.

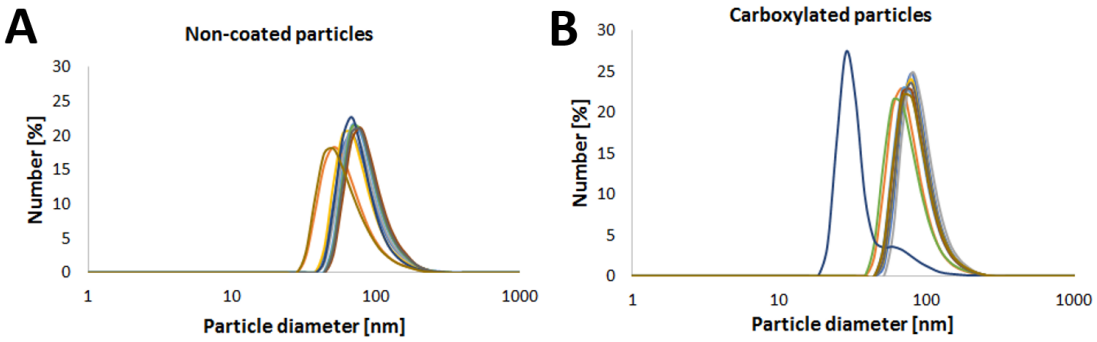

Fig. 47: DLS size distribution obtained from ten repeated measurements for bare LuAG:Ce^{3+} nanoparticles (A) and carboxylated LuAG:Ce^{3+}@SiO_2-COOH nanoparticles (B). The average particle size from the DLS measurements was (80.60 ± 31.19) nm for the bare nanoparticles and (85.34 ± 28.12) nm for the carboxylated nanoparticles.

4.4.2. Luminescent properties

Luminescent characteristics of the LuAG:Ce^{3+} core are presented in Fig. 48. In the RT PL excitation-emission spectra, the excitation (347 nm and 450 nm) and emission (510 nm) maxima correspond to parity-allowed 4f – 5d transitions of Ce^{3+} centers.

Luminescent properties of the material are also supplemented by CL imaging of the pure luminescent core in the SEM: Fig. 49A shows SEM images of the LuAG:Ce^{3+} powder, in Fig. 49B the nanoparticles were mixed with suspension of the yeasts *Saccharomyces cerevisiae* in physiological saline solution. The SEM images show strong green luminescence, which was stable under the 10 kV electron beam irradiation. Even at the acceleration voltage of 20 kV, the nanoparticles exhibited no decrease in CL intensity. During the SEM imaging, no significant decrease of luminescence intensity was

observed even when repeatedly imaging the same position of the sample. The material is quite durable and resistant to destruction by the high energy electron beam. In contrast, other potential CL materials for SEM like CdTe quantum dots are immediately destroyed by the 10 kV electron beam.

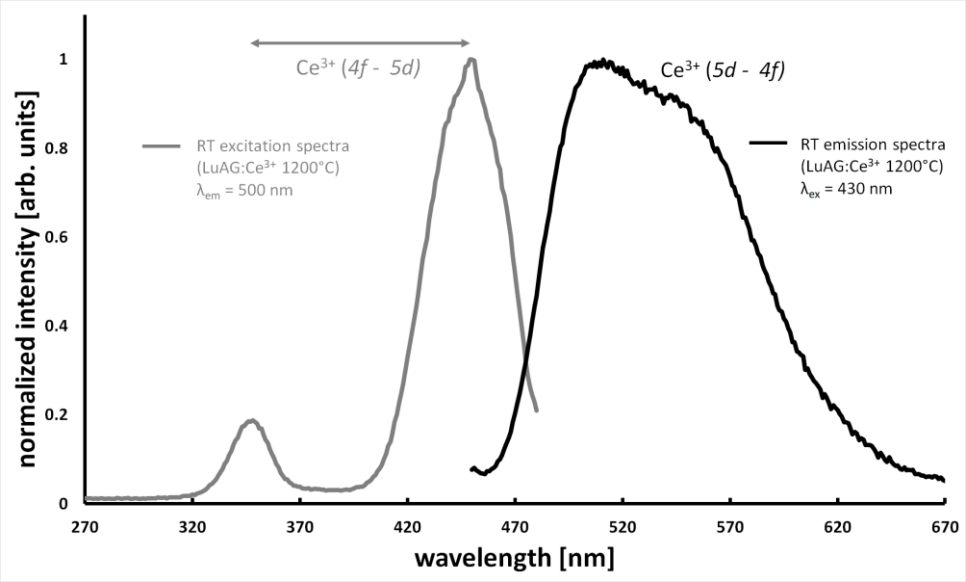

Fig. 48: RT PL excitation spectrum (A) obtained by selecting the emission wavelength at 500 nm, and emission spectrum (B) measured under excitation at 430 nm of the LuAG:Ce^{3+} nanoparticles sample.

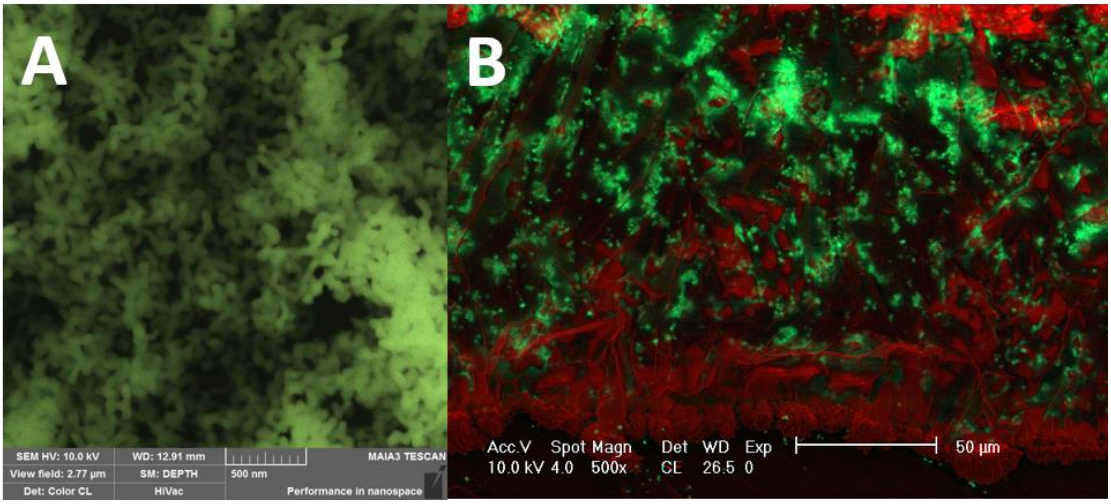

Fig. 49: CL in the SEM of the pure LuAG:Ce^{3+} nanopowder (A) and suspension of the nanopowder with *Saccharomyces cerevisiae* yeast cells in physiological saline solution (B). Strong green emission belongs to the LuAG:Ce^{3+} nanoparticles; red emission belongs to organic substrate in the sample. Accelerating voltage 10 kV was utilized.

4.4.3. CL bioimaging

The applicability of the LuAG:Ce^{3+} nanoparticles for CL bioimaging was demonstrated on the common yeast line *Saccharomyces cerevisiae*. The rigid yeast cell wall can withstand the extreme vacuum conditions in the SEM and maintain its shape without fixation otherwise needed for other biological samples. The yeasts were cultured in sugar-containing medium and mixed with nanoparticles to achieve non-specific absorption of the nanoparticles on their surface. Fig. 50 shows nanoparticles randomly adsorbed on the surface of the budding yeast cell, as evidenced by random distribution of the luminescent spots. The image was acquired using SEM with panchromatic CL detector (Fig. 50A and B) and InBeam secondary electron detector (Fig. 50C).

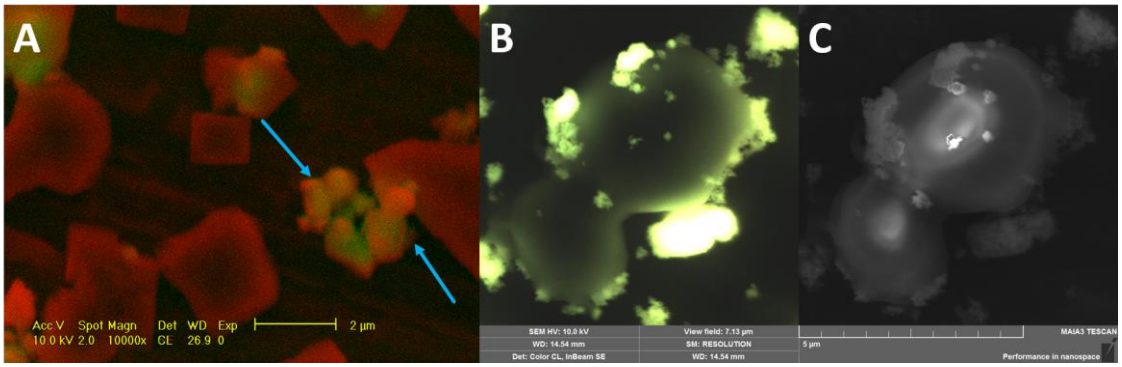

Fig. 50: Yeast cell imaging with LuAG:Ce^{3+} as a contrast agent using panchromatic CL detector (A,B) and InBeam secondary electron detector (C).

For increasing the number of nanoparticles on the cells surface and achieving specific binding, the nanoparticles were coated with a carboxylated silica layer to provide crosslinker for subsequent anti-FasL antibody conjugation. To verify binding specificity of the LuAG:Ce^{3+}@SiO_2-anti-FasL bioconjugate, the T-lymphocytes were incubated with the bioconjugate and subsequently washed to remove the excess of unbound nanoparticles. The labeled cells were then observed first on a fluorescence microscope and then in the SEM.

Fig. 51(A) shows the fluorescence microscope image of the T-lymphocyte specifically labeled with the LuAG:Ce^{3+}@SiO_2-anti-FasL bioconjugate. Due to its inorganic nature, the nanoparticles exhibit no photobleaching in the fluorescence microscope and can be excited using the UV light filters commonly used for DAPI (4',6-diamidino-2-phenylindole) or Hoechst 33 342 nuclei staining fluorophores. Thus,

fluorescence microscopy could be another potential application of these nanoparticles. Fig. 51 shows the SEM images of the FasL on the plasma membrane of T-lymphocytes from the InBeam secondary electron detector (Fig. 51B) and CL detector (Fig. 51C). Since the excess of the unbound luminophore was removed by washing process, it is highly probable that the majority of the luminescent spots in Fig. 51 belongs to the bioconjugate linked to the FasL via antibody-antigen interactions. Bioconjugation significantly improves distribution, and the luminescent spots are evenly distributed across the cell membrane. The proof of the chemical bond formation between LuAG:Ce^{3+}@SiO_2-anti-FasL bioconjugate and living cell receptor is, however, the subject of future research.

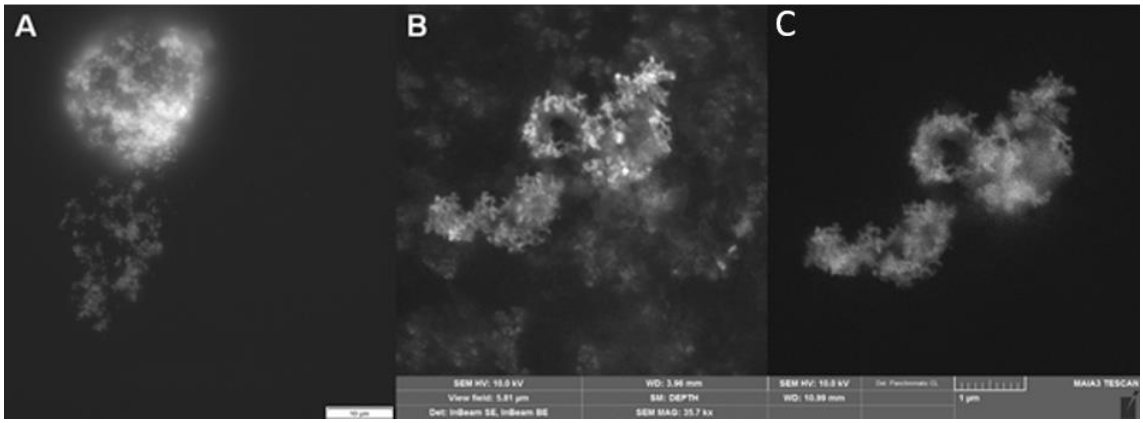

Fig. 51: Fluorescence microscope image of a T-lymphocyte labeled with LuAG:Ce^{3+}@SiO_2-anti-FasL bioconjugate (A) and SEM images of the labeled T-lymphocytes from the InBeam secondary electron detector (B) and CL detector (C).

4.5. Biocompatibilization of LuAG:Ce^{3+}@mesoSiO_2 NPs

For *in vivo* application, the outer shell of the nanocomposite should contain molecules increasing its biocompatibility in order to avoid unwanted interferences with metabolism or immune system. To increase biocompatibility of LuAG:Ce^{3+}@mesoSiO_2 nanoparticles, the nanocomposite was conjugated with PEG molecules. The design of the nanocomposite included three main steps: photo-induced synthesis of LuAG:Ce^{3+} nanoparticles, mesoporous silica encapsulation, providing both binding sites for PEG molecules attachment and pores for feasible photosensitizer loading, and, finally, PEGylation.

TEM micrographs in Fig. 52 show the results of the first and the second steps of the synthesis – the LuAG:Ce^{3+} nanoparticles treated at 1200 °C (Fig. 52A) and nanoparticles after surface coating with mesoporous silica shell (Fig. 52B). It is obvious, that after surface modification, a porous silica shell was formed. Fig. 52B was analyzed using the ImageJ software (Schneider et al., 2012), and the size of the pores was determined to be approximately 3 nm, and therefore it can be assumed, that the vacancies due to pores may be used for incorporation of, e.g., photosensitizer molecules for application in PDTX. On the other hand, the coating process leads to the formation of nanoparticle aggregates; therefore, further modification of technological process to segregate the grains in needed.

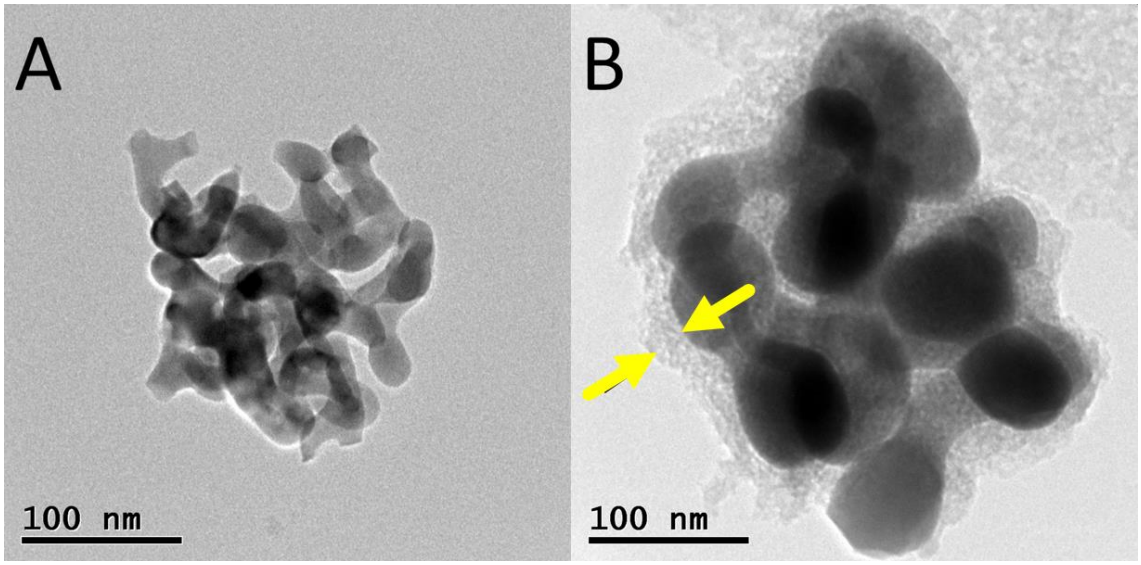

Fig. 52: TEM images of the as-prepared LuAG:Ce^{3+} nanoparticles calcined at 1200 °C (A), and nanoparticles coated with a mesoporous silica shell (B).

For confirming the formation of the chemical bond between LuAG:Ce^{3+}@mesoSiO_2 and PEG molecules, ss-NMR spectra were measured. Fig. 53 displays results for ^{29}Si ss-NMR of the LuAG:Ce^{3+}@mesoSiO_2 (Fig. 53A) and PEGylated LuAG:Ce^{3+}@mesoSiO_2-PEG (Fig. 53B) samples. In both spectra, silicon environment Q^2 appears around –90 ppm, Q^3 around –100 ppm and Q^4 around –110 ppm (Steel et al., 1995). Chemical shift peaking at –66 ppm in Fig. 53A corresponds to primary amines (Maciel, 1998) provided by APTES molecules after polycondensation reactions. Considerable intensity change of the peak is explained by the bonding of PEG molecules to the –NH_2 functional groups.

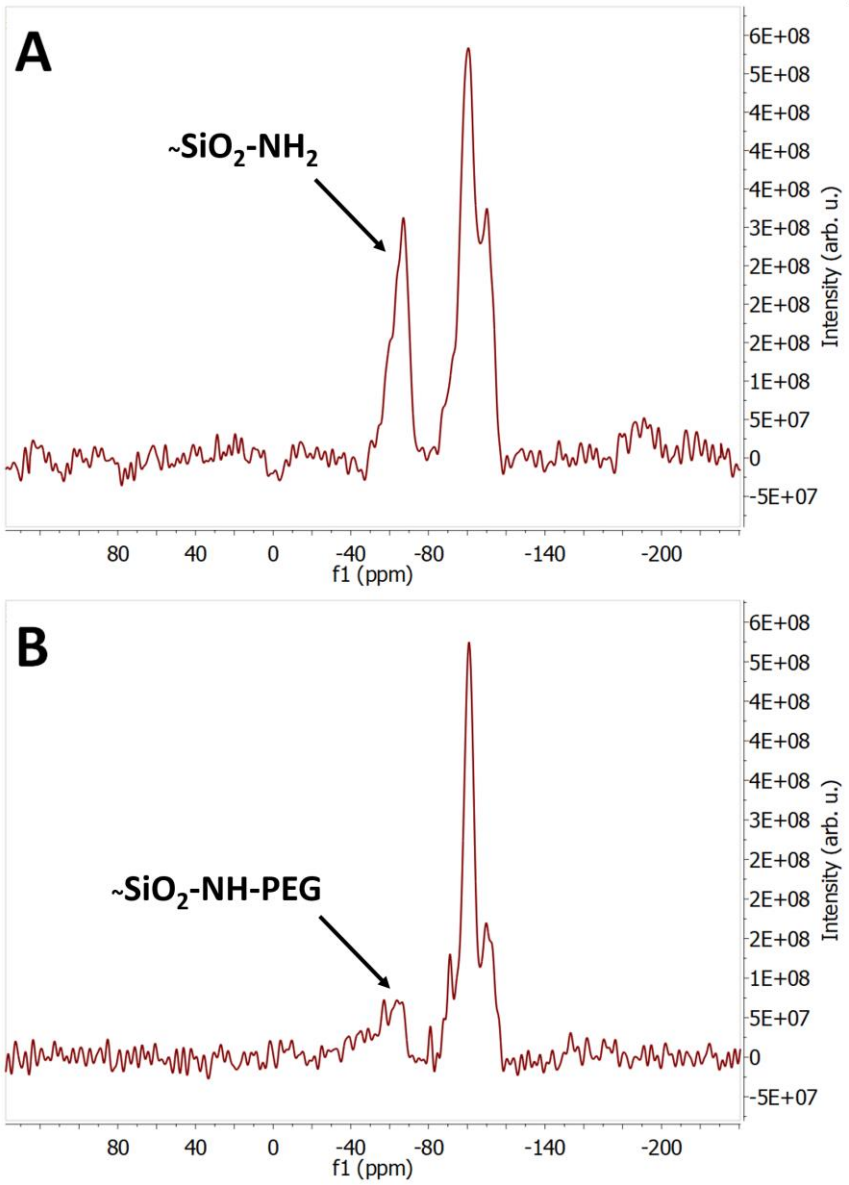

Fig. 53: ^{29}Si ss-NMR spectra of the LuAG:Ce^{3+}@mesoSiO_2 (A) and LuAG:Ce^{3+}@mesoSiO_2-PEG (B) samples.

5. Conclusions

Preparation of YSO:Ce^{3+}(1%) and YSO:Ce^{3+}(1%), as a potential scintillating core of the luminescent nanocomposites, was carried out using room temperature sol-gel route, yielding pure powder materials with good luminescent properties. Using TG/DTA method, the temperature required to form the oxyorthosilicates from their prepared precursors was determined as 1040 °C and 1300 °C for X1-type and X2-type YSO, in the case of LSO, 1050 °C and 1150 °C for A- and B-LSO, respectively.

Measured RT RL spectra of both materials show higher luminescence intensity of the samples, as compared to the BGO powder standard. Reduction of the faster component decay was observed in the YSO:Ce^{3+} sample after grinding and separation of the small particle fraction. Comparison of the measured decay times for YSO:Ce^{3+} and LSO:Ce^{3+} prepared samples also indicates acceleration in the decay, as compared to the data for the bulk single crystal. Nevertheless, the average particles size determined from the TEM measurements was in micrometer range that excludes *in vivo* applications of the prepared YSO:Ce^{3+} and LSO:Ce^{3+}. However, the materials may be good candidates for fast-timing composite detectors.

A highly prospective drug for PDTX, LuAG:Pr^{3+}@SiO_2-PpIX luminescent nanocomposite, was successfully prepared using a three-step process: photo-induced synthesis of the LuAG:Pr^{3+}(1%) core, modification of the nanoparticles with amorphous silica shell with subsequent covalent conjugation of PpIX molecules. Prior to the PDTX nanocomposite synthesis, a comparison of sol-gel, dense-liquid and combined two-step process was made. The results revealed priority of sol-gel technique, which seems to be the easiest and leads to formation of relatively uniform coating with minimal interfering in nanoparticles luminescent properties.

Room temperature radioluminescence as well as photoluminescence steady-state and time-resolved spectra of the LuAG:Pr^{3+}@SiO_2-PpIX nanocomposite material confirm radiative energy transfer from the core to the PpIX outer shell, which is important for further $^1O_2$ generation in PDTX. The singlet oxygen generation in the system was demonstrated using APF chemical probe. RT PL spectra of the LuAG:Pr^{3+}@SiO_2-PpIX with addition of APF exhibit enhanced luminescence band at 530 nm, confirming formation of luminescent complex of APF with $^1O_2$ and presence of

singlet oxygen in the irradiated system. Reaction of APF with parasitic –OH radicals was ruled out by RT PL measurements with addition of NaN_3, acting as an inhibitor of $^1O_2$.

LuAG:Ce^{3+}@SiO_2-anti-FasL nanocomposite for cathodoluminescence bioimaging modality was also synthesized. Surface modification with carboxylated amorphous silica shell of the LuAG:Ce^{3+}(0.2%) core, which was obtained by photo-induced precipitation, was performed. LuAG:Ce^{3+}@SiO_2-COOH nanocomposite was further biofunctionalized with anti-FasL antibody ensuring specific targeting to the cells trans-membrane proteins. Results from the CL SEM show that LuAG:Ce^{3+} core maintains good stability and exhibits strong green luminescence without photobleaching after 10 kV high energy electron beam excitation. CL bioimaging was demonstrated by either non-specific adsorption of the LuAG:Ce^{3+} nanoparticles on the cells surface or by specific targeting of trans-membrane protein by the LuAG:Ce^{3+}@SiO_2-anti-FasL bioconjugate.

Preliminary study of biocompatibilization of nanocomposites on LuAG:Ce^{3+}@mesoSiO$_2$ material indicates that biocompatibility of luminescent nanocomposites can be achieved by binding of PEG molecules on the mesoporous silica-modified surface binding sites. ^{29}Si ss-NMR confirms formation of the bonds between LuAG:Ce^{3+}@mesoSiO$_2$ and PEG molecules. Moreover, it was observed, that mesoporous silica shell provides 3 nm pores suitable for e.g. photosensitizer loading.

Summing up the results, the obtained materials can be assumed to be good candidates for multimodal biocompatible drug preparation and application in X-ray induced photodynamic therapy and cathodoluminescence bioimaging.

References

Abliz, E., Collins, J.E., Bell, H., Tata, D.B., **2011**. *Novel applications of diagnostic X-rays in activating a clinical photodynamic drug: Photofrin II through X-ray induced visible luminescence from "rare-earth" formulated particles*. J. X-ray Sci. Technol. 19, 521 – 530.

Adamiano, A., Iafisco, M., Sandri, M., Basini, M., Arosio, P., Canu, T., Sitia, G., Esposito A., Iannotti, V., Ausanio, G., Fragogeorgi, E., Rouchota, M., Loudos, G., Lascialfari, A., Tampieri, A., **2018**. *On the use of superparamagnetic hydroxyapatite nanoparticles as an agent for magnetic and nuclear in vivo imaging*. Acta Biomater. 73, 458 – 469.

Adjei, I.M., Sharma, B., Labhasetwar, V., **2014**. *Nanoparticles: cellular uptake and cytotoxicity*. Adv. Exp. Med. Biol. 811, 73 – 91.

Andersen, M.Z., Schrama, D., Thor Straten, P., Becker, J.C., **2006**. *Cytotoxic T cells*. J. Invest. Dermatol. 126 (1), 32 – 41.

Ansari, A.A., **2018**. *Silica-modified luminescent $LaPO_4$:Eu@$LaPO_4$@SiO_2 core/shell nanorods: Synthesis, structural and luminescent properties*. Luminescence 33, 112 – 118.

Arruebo, M., Fernández-Pacheco, R., Ibarra, M.R., Santamaría, J., **2007**. *Magnetic nanoparticles for drug delivery.* Nano Today 2 (3), 22 – 32.

Arruebo, M., Galán, M., Navascués, N., Téllez, C., Marquina, C., Ibarra, M.R., Santamaría, J., **2006**. *Development of magnetic nanostructured silica-based materials as potential vectors for drug-delivery applications*. Chem. Mater. 18 (7), 1911 – 1919.

Arruebo, M., Valladares, M., González-Fernández, A., **2009**. *Antibody-conjugated nanoparticles for biomedical applications.* J. Nanomater. 2009, Art. No. 439389.

Asiaei, S., Smith, B., Nieva, P., **2015**. *Enhancing conjugation rate of antibodies to carboxylates: Numerical modeling of conjugation kinetics in microfluidic channels and characterization of chemical over-exposure in conventional protocols by quartz crystal microbalance*. Biomicrofluidics 9 (6), Art. No. 064115.

Auffray, E., Borisevitch, A., Gektin, A., Gerasymov, Ia., Korjik, M., Kozlov, D., Kurtsev, D., Michinsky, V., Sidletskiy, O., Zoueyski, R., **2015**. *Radiation damage effect in Y_2SiO_5:Ce scintillation crystals under γ-quanta and 24 GeV protons.* Nucl. Instrum. Methods Phys. Res. A 783, 117 – 120.

Babin, V., Blazek, K., Krasnikov, A., Nejezchleb, K., Nikl, M., Savikhina, T., Zazubovich, S., **2005**. *Luminescence of undoped LuAG and YAG crystals*. Phys. Stat. Sol. (c) 2 (1), 97 – 100.

Balasubramanyam, S., Merkx, M.J.M., Verheijen, M.A., Kessels, W.M.M., Mackus, A.J.M., Bol, A.A., **2020**. *Area-selective atomic layer deposition of two-dimensional WS_2 nanolayers*. ACS Mater. Lett. 2 (5), 511 – 518.

Bamrungsap, S., Zhao, Z., Chen, T., Wang, L., Li, C., Fu, T., Tan, W., **2012**. *Nanotechnology in therapeutics: a focus on nanoparticles as a drug delivery system.* Nanomedicine 7 (8), 1253 – 1271.

Bancirova, M., **2011**. *Sodium azide as a specific quencher of singlet oxygen during chemiluminescent detection by luminol and Cypridina luciferin analogues*. Luminescence 26, 685 – 688.

Baptista, M.S., Cadet, J., Di Mascio, P., Ghogare, A.A., Greer, A., Hamblin, M.R., Lorente, C., Nunez, S.C., Ribeiro, M.S., Thomas, A.H., Vignoni, M., Yoshimura, T.M., **2017**. *Type I and II photosensitized oxidation reactions: guidelines and mechanistic pathways*. Photochem. Photobiol. 93 (4), 912 – 919.

Bárta, J., Čuba, V., Pospíšil, M., Jarý, V., Nikl, M., **2012**. *Radiation-induced preparation of pure and Ce-doped lutetium aluminium garnet and its luminescent properties*. J. Mater. Chem. 22, 16590-16597.

Bárta, J., **2015**. *Radiation and photo-induced preparation of synthetic garnets based on LuAG ($Lu_3Al_5O_{12}$)*. Ph.D. dissertation, Czech Technical University in Prague, Czech Republic.

Bentzen, E.L., Tomlinson, I.D., Mason, J., Gresch, P., Warnement, M.R., Wright, D., Sanders-Bush, E., Blakely, R., Rosenthal, S.J., **2005**. *Surface modification to reduce nonspecific binding of quantum dots in live cell assays.* Bioconjug. Chem. 16 (6), 1488 – 1494.

Blahuta, S., Bessière, A., Viana, B., Dorenbos, P., Ouspenski, V., **2013**. *Evidence and consequences of Ce in LYSO:Ce,Ca and LYSO:Ce,Mg single crystals for medical imaging applications*. IEEE Trans. Nucl. Sci. 60 (4), 3134 – 3140.

Blasse, G., Grabmaier, B.C., **1994**. *Luminescent materials*. Springer-Verlag, Berlin, Germany.

Boukerika, A., Guerbous, L., **2015**. *Investigation of the structural and photoluminescence properties of Ce^{3+}-doped LuAG nanopowders prepared via sol–gel method*. Opt. Mater. 40, 14 – 19.

Boyer, J.-C., Manseau, M.-P., Murray, J.I., van Veggel, F.C.G.M., **2010**. *Surface modification of upconverting $NaYF_4$ nanoparticles with PEG–phosphate ligands for NIR (800 nm) biolabeling within the biological window.* Langmuir 26 (2), 1157-1164.

Bulin, A.-L., Truillet, C., Chouikrat, R., Lux, F., Frochot, C., Amans,D., Ledoux, G., Tillement, O., Perriart, P., Barberi-Heyob, M., Dujardin, C., **2013**. *X-ray-induced singlet oxygen activation with nanoscintillator-coupled porphyrins.* J. Phys. Chem. C 117 (41), 21583 – 21589.

Bulin, A.-L., Vasil'ev, A., Belsky, A., Amans, D., Ledoux, G., Dujardin, C., **2015**. *Modelling energy deposition in nanoscintillators to predict the efficiency of the X-ray-induced photodynamic effect.* Nano 7 (13), 5744 – 5751.

Bulin, A.-L., Broekgaarden, M., Simeone, D., Hasan, T., **2019**. *Low dose photodynamic therapy harmonizes with radiation therapy to induce beneficial effects on pancreatic heterocellular spheroids.* Oncotarget 10 (27), 2625 – 2643.

Burešová, H., Procházková, L., Turtos, R.M., Jarý, V., Mihóková, E., Beitlerová, A., Pjatkan, R., Gundacker, S., Auffray, E., Lecoq, P., Nikl, M., Čuba, V., **2016**. *Preparation and luminescence properties of ZnO:Ga – polystyrene composite scintillator.* Opt. Express 24 (14), 15289 – 15298.

Cai, W.,Chen, Q.,Cherepy, N., Dooraghi, A., Kishpaugh, D., Chatziioannou, A., Payne, S., Xiang, W.,Pei, Q., **2013**. *Synthesis of bulk-size transparent gadolinium oxide-polymer nanocomposites for gamma ray spectroscopy*. J. Mater. Chem. C 1 (10), 1971 – 1976.

Caruso, F., **2001**. *Nanoengineering of Particle Surfaces*. Adv. Mater. 13 (1), 11 – 22.

Catauro, M., Bollino, F., Papale, F., **2018**. *Surface modifications of titanium implants by coating with bioactive and biocompatible poly (ε-caprolactone)/SiO_2 hybrids synthesized via sol–gel.* Arabian J. Chem. 11 (7), 1123 – 1126.

Chai, W., Chen, Q., Cherepy, N., Dooraghi, A., Kishpaugh, D., Chatziioannou, A., Payne, S., Xiang, W., Pei, Q., **2013**. *Synthesis of bulk-size transparent gadolinium oxide - polymer nanocomposites for gamma ray spectroscopy*. J. Mater. Chem. C 1, 1970 – 1976.

Chandler, D.E., Roberson, R.W., **2009**. *Bioimaging: current concepts in light and electron microscopy*. Jones and Bartlett Publishers, Sudbury, Massachusetts, USA.

Chen, B., Evans, J.R.G., Greenwell, C.H., Boulet, P., Coveney, P.V., Bowden, A.A., Whiting, A., **2008**. *A critical appraisal of polymer–clay nanocomposites*. Chem. Soc. Rev. 37, 568 – 594.

Chen, F., Ehlerding, E.B., Cai, W., **2014**. *Theranostic nanoparticles.* J. Nucl. Med. 55 (12), 1919 – 1922.

Chen, H., Wang, G.D., Chuang, Y.J., Zhen, Z., Chen, X., Biddinger, P., Hao, Z., Liu, F., Shen, B., Pan, Z., Xie, J., **2015**. *Nanoscintillator-mediated X-ray inducible photodynamic therapy for in vivo cancer treatment*. Nano Lett. 15 (4), 2249 – 2256.

Chen, W., **2008a**. *Nanoparticle fluorescence based technology for biological applications*. J. Nanosci. Nanotechnol. 8, 1019-1051.

Chen, W., **2008b**. *Nanoparticle self-lighting photodynamic therapy for cancer treatment*. J. Biomed. Nanotechnol. 4, 369 – 376.

Chen, W., Zhang, J., **2006**. *Using nanoparticles to enable simultaneous radiation and photodynamic therapies for cancer treatment.* J. Nanosci. Nanotechnol. 6 (4), 1159 – 1166.

Cheng, S.-H., Lo, L.-W., **2011**. *Inorganic nanoparticles for enhanced photodynamic cancer therapy.* Curr. Drug Discov. Technol. 8 (3), 250 – 268.

Chiriu, D., Stagi, L., Carbonaro, C.M., Corpino, R., Ricci, P.C., **2016**. *Energy transfer mechanism between Ce and Tb ions in sol–gel synthesized YSO crystals*. Mater. Chem. Phys. 171, 201 – 207.

Christian, P., Von der Kammer, F., Baalousha M., Hofmann, Th., **2008**. *Nanoparticles: structure, properties, preparation and behaviour in environmental media.* Ecotoxicology 17, 326 – 343.

Clement, S., Deng, W., Camilleri, E., Wilson, B.C., Goldys, E.M., **2016**. *X-ray induced singlet oxygen generation by nanoparticle-photosensitizer conjugates for photodynamic therapy: determination of singlet oxygen quantum yield*. Sci. Rep. 6, Art. No. 19954.

Colombeau, L., Acherar, S., Baros, F., Arnoux, P., Mohd Gazzali, A., Zaghdoudi, K., Toussaint, M., Vanderesse, R., Frochot, C., **2016**. *Inorganic nanoparticles for photodynamic therapy.* Top Curr. Chem. 370, 113 – 134.

Conde, J., Dias, T., Grazú, V., Moros, M., Baptista, P.V., de la Fuente, J.M., **2014**. *Revising 30 years of biofunctionalization and surface chemistry of inorganic nanoparticles for nanomedicine*. Frontiers Chem. 2, Art. No. 48.

Crivianu-Gaita, V., Romaschin, A., Thompson, M., **2015**. *High efficiency reduction capability for the formation of Fab' antibody fragments from F(ab)$_2$ units*. Biochem. Biophys. Rep. 2, 23 – 28.

Cui, M., Liu, S., Song, B., Guo, D., Wang, J., Hu, G., Su, Y., He, Y., **2019**. *Fluorescent silicon nanorods-based nanotheranostic agents for multimodal imaging-guided photothermal therapy*. Nano-Micro Lett. 11 (1), Art. No. 73.

DeRosa, M.C., Crutchley, R.J., **2002**. *Photosensitized singlet oxygen and its application.* Coord. Chem. Rev. 233 – 234, 351 – 371.

Dexter, D.L., **1953**. *A theory of sensitized luminescence in solids*. J. Chem. Phys. 21, 836 – 850.

Edwards, P.R., Martin, R.W., **2011**. *Cathodoluminescence nano-characterization of semiconductors.* Semicod. Sci. Technol. 26, Art. No. 064005.

Estephan, Z.G., Jaber, J.A., Schlenoff, J.B., **2010**. *Zwitterion-stabilized silica nanoparticles: Toward nonstick nano*. Langmuir 26 (22), 16884 – 16889.

Furukawa, T., Fukushima, S., Niioka, H., Yamamoto, N., Miyake, J., Araki, T., Hashimoto, M., **2015**. *Rare-earth-doped nanophosphors for multicolor cathodoluminescence nanobioimaging using scanning transmission electron microscopy*. J. Biomed. Opt. 20 (5), Art. No. 056007.

Gallardo-Villagrán, M., Leger, D.Y., Liagre, B., Therrien, B., **2019**. *Photosensitizers used in the photodynamic therapy of rheumatoid arthritis*. Int. J. Mol. Sci. 20, Art. No. 3339.

Guerrero-Martínez, A., Pérez-Juste, J., Liz-Marzán, L.M., **2010**. *Recent progress on silica coating of nanoparticles and related nanomaterials.* Adv. Mater. 22, 1182 – 1195.

Gustafsson, T., Klintenberg, M., Derenzo, S. E., Weber, M. J., Thomas, J. O., **2001**. *Lu_2SiO_5 by single-crystal X-ray and neutron diffraction*. Acta Crystallogr. C 57, 668 – 669.

Halder, N.C., Wagner, C.N.J., **1966**. *Separation of particle size and lattice strain in integral breadth measurements.* Acta Cryst. 20, 312 – 313.

Hanemann, T., Szabó, D.V., **2010**. *Polymer-nanoparticle composites: from synthesis to modern applications.* Materials 3, 3468 – 3517.

Hehir, J.P., Henry, M.O., Larkin, J.P., Imbusch, G.F., **1974**. *Nature of the luminescence from YAG:Cr^{3+}*. J. Phys. C: Solid State Phys. 7, 2241-2248.

Hermanson, G.T., **2013**. *Bioconjugate techniques*. Academic Press, London, UK.

Hu, H., Xiong, L., Zhou, J., Li, F., Cao, T., Huang, C., **2009**. *Multimodal-luminescence core-shell nanocomposites for targeted imaging of tumor cells*. Chem. Eur. J. 15, 3577 – 3584.

Hu, X., Gao, X., **2011**. *Multilayer coating of gold nanorods for combined stability and biocompatibility.* Phys. Chem. Chem. Phys. 13 (21), 10028 – 10035.

Iler, R.K., **1996**. *Multilayers of colloidal particles*. J. Colloid Interface Sci. 21, 569 – 594.

Issa, A.A., El-Azazy, M., Luyt, A.S., **2019**. *Kinetics of alkoxysilanes hydrolysis: An empirical approach.* Sci. Rep. 9, Art. No. 17624.

Ito, J., Johnson, H., **1968**. *Synthesis and study of yttralite*. Am. Miner. 53, 1940 – 1952.

Jansons, J., Rachko, Z., Valbis, J., Andriessen, J., Dorenbos, P., van Eijk, C.W.E., Khaidukov, N.M., **1992**. *Cross-luminescence of complex halide crystals*. J. Phys. Condens. Matter 5 (10), 1589 – 1596.

Jeevanandam, J., Barhoum, A., Chan, Y.S., Dufresne, A., Danquah, M.K., **2018**. *Review on nanoparticles and nanostructured materials: history, sources, toxicity and regulations.* Beilstein J. Nanotech. 9, 1050 – 1074.

Josefsen, L.B., Boyle, R.W., **2012**. *Unique diagnostic and therapeutic roles of porphyrins and phthalocyanines in photodynamic therapy, imaging and theranostics*. Theranostics 2 (9), 916 – 966.

Key, J., Leary, J.F., **2014**. *Nanoparticles for multimodal in vivo imaging in nanomedicine*. Int. J. Nanomed. 9, 711 – 726.

Kim, J., Kim, H.S., Lee, N., Kim, T., Kim, H., Yu, T., Song, I.C., Moon, W.K., Hyeon, T., **2008**. *Multifunctional uniform nanoparticles composed of a magnetite nanocrystal core and a mesoporous silica shell for magnetic resonance and fluorescence imaging and for drug delivery.* Angew. Chem. Int. Ed. Engl. 47 (44), 8438 – 8441.

Knoll, G.F., **2010**. *Radiation detection and measurement.* John Wiley & Sons, Inc., Hoboken, USA.

Kobayashi, H., Watanabe, R., Choyke, P.L., **2014**. *Improving conventional enhanced permeability and retention (EPR) effect; What is the appropriate target?* Theranostics 4 (1), 81 – 89.

Kochevar, I.E., Lynch, M.C., Zhuang, S., and Lambert, C.R., **2008**. *Singlet oxygen, but not oxidizing radicals, induces apoptosis in HL-60 cells.* Photochem. Photobiol. 72 (4), 548 – 553.

Kong, D.Y., Wang, Z.L., Lin, C.K., Quan, Z.W., Li, Y.Y., Li, C.X., Lin, J., **2007**. *Biofunctionalization of $CeF_3:Tb^{3+}$ nanoparticles*. Nanotechnology 18, Art. No. 075601.

Kömpe K., Borchert, H., Storz, J., Lobo, A., Adam, S., Möller, T., Haase, M., **2003**. *Green-emitting $CePO_4:Tb/LaPO_4$ core-shell nanoparticles with 70% photoluminescence quantum yield.* Angew. Chem. Int. Ed. Engl. 42 (44), 5513 – 5516.

Kuhn, H.J., Braslavsky, S.E., Schmidt, R., **2004**. *Chemical actinometry (IUPAC technical report)*. Pure Appl. Chem. 76 (12), 2105 – 2146.

Labrador-Páez, L., Ximendes, E.C., Rodríguez-Sevilla, P., Ortgie, D.H., Rocha, U., Jacinto, C., Rodríguez, E.M., Haro-González, P., Jaque, D., **2018**. *Core–shell rare-earth-doped nanostructures in biomedicine*. Nanoscale 10, 12935 – 12956.

Langford, J.I., Wilson, A.J.C., **1978**. *Scherrer after sixty years: a survey and some new results in the determination of crystallite size.* J. App. Cryst. 11, 102 – 113.

Lee, D.-E., Koo, H., Sun, I.-C., Ryu, J.H., Kim, K., Kwon, I.C., **2012**. *Multifunctional nanoparticles for multimodal imaging and theragnosis.* Chem. Soc. Rev. 41 (7), 2656 – 2672.

Li, J.J., **2002**. *Schotten-Baumann reaction*. In: Name Reactions. Springer, Berlin, Heidelberg.

Li, C., Lin, J., **2010**. *Rare earth fluoride nano-/microcrystals: synthesis, surface modification and application*. J. Mater. Chem. 20, 6831-6847.

Li, X., Zhang, X.-N., Li, X.-D., Chang, J., **2016***. Multimodality imaging in nanomedicine and nanotheranostics.* Cancer Biol. Med. 13 (3), 339 – 348.

Liu, Q., Xu, Z., Finch, J.A., Egerton, R., **1998**. *A novel two-step silica-coating process for engineering magnetic nanocomposites.* Chem. Mater. 10, 3936 – 3940.

Liu, Y., Zhang, S., Wang, S., Pope, C., Chen, W., **2008a**. *Optical behaviors of ZnO-porphyrin conjugates and their potential applications for cancer treatment*. Appl. Phys. Lett. 92 (14), Art. No. 143901.

Liu, Y., Chen, W., Wang, S., Joly, A.G., **2008b**. *Investigation of water-soluble X-ray luminescence nanoparticles for photodynamic activation.* Appl. Phys. Lett. 92 (4), Art. No. 043901.

Liu, Z., Kiessling, F., Gätjens, J., **2010**. *Advanced nanomaterials in multimodal imaging: design, functionalization, and biomedical applications*. J. Nanomater. 2010, Art. No. 894303.

Lu, H., Yi, G., Zhao, S., Chen, D., Guo, L.-H., Cheng, J., **2004**. *Synthesis and characterization of multi-functional nanoparticles possessing magnetic, up-conversion fluorescence and bio-affinity properties*. J. Mater. Chem. 14, 1336 – 1341.

Maciel, G.E., **1998**. *NMR characterization of functionalized polysiloxanes*. Stud. Phys. Theor. Chem. 84, 923 – 984.

Maeda, H., **2001**. *SMANCS and polymer-conjugated macromolecular drugs: advantages in cancer chemotherapy*. Adv. Drug Deliv. Rev. 46 (1-3), 169 – 185.

Mares, J.A., Beitlerova, A., Nikl, M., Solovieva, N., D'Ambrosio, C., Blazek, K., Maly, P., Nejezchleb, K., de Notaristefani, F., **2004**. *Scintillation response of Ce-doped or intrinsic scintillating crystals in the range up to 1 MeV*. Radiat. Meas. 38 (4 – 6), 353 – 357.

Masciangioli, T., Zhang, W.-X., **2003**. *Nanotechnology could substantially enhance environmental quality and sustainability through pollution prevention, treatment, and remediation*. Environ, Sci. Technol. 37 (5), 108A – 130A.

McKigney, E.A., Del Sesto, R.E., Jacobsohn, L.G., Santi, P.A., Muenchausen, R.E., Ott, K.C., Mark McCleskey, T., Bennett, B.L., Smith, J.F., Wayne Cooke, D., **2007**. *Nanocomposite scintillators for radiation detection and nuclear spectroscopy.* Nucl. Instr. Meth. Phys. Res. A 579 (1), 15 – 18.

McMurdie, H., Morris, M., Evans, E., Paretzkin, B., Wong-Ng, W., Hubbard, C., **1986**. *New X-Ray Powder Diffraction Patterns from the JCPDS Associateship*. Powder Diffr. 1, 77 - 99.

Melcher, C.L., Schweitzer, J.S., **1992**. *Cerium-doped lutetium oxyorthosilicate: a fast efficient new scintillator.* IEEE Trans. Nucl. Sci. 39 (4), 502 – 505.

Miranda, M.A.R., Sasaki, J.M., **2018**. *The limit of application of the Scherrer equation.* Acta Cryst. A 74, 54 – 65.

Misawa, M., Takahashi, J., **2011**. *Generation of reactive oxygen species induced by gold nanoparticles under X-ray and UV irradiations*. Nanomed.-Nanotechnol. 7 (5), 604 – 614.

Mohammadi, Z., Sazgarnia, Rajabi, O., Seilanian Toosi, M., **2017**. *Comparative study of X-ray treatment and photodynamic therapy by using 5-aminolevulinic acid conjugated gold nanoparticles in a melanoma cell line.* Artif. Cells Nanomed. Biotechnol. 45 (3), 467 – 473.

Mueller-Bunz, H., Schleid, T., **1999**. *Ueber die oxidsilicate $M_2O(SiO_4)$ der schweren lanthanoide (M = Dy - Lu) im A-Typ*. Z. Anorg. Allg. Chem. 625, 613 – 618.

Muresan, L.E., Karabulut, Y., Cadis, A.I., Perhaita, I., Canimoglu, A., Guinea, J.G., Tudoran, L.B., Silipas, D., Ayvacikli, M., Can, N., **2016**. *Tunable luminescence of broadband-excited and narrow line green emitting $Y_2SiO_5:Ce^{3+}$, Tb^{3+} phosphor*. J. Alloy. Comp. 658, 356 – 366.

Nikl, M., **2006**. *Scintillation detectors for x-rays*. Meas. Sci. Technol. 17, R37 – R54.

Nowostawska, M., Corr, S.A., Byrne, S.J., Conroy J., Volkov, Y., Gun'ko, Y.K., **2011**. *Porphyrin-magnetite nanoconjugates for biological imaging*. J. Nanobiotechnol. 9, Art. No. 13.

Ogiegło, J.M., Zych, A., Jüstel, T., Meijerink, A., Ronda, C.R., **2013**. *Luminescence and energy transfer in $Lu_3Al_5O_{12}$ scintillators co-doped with Ce^{3+} and Pr^{3+}*. Opt. Mater. 35 (3), 322 – 331.

Ogino, H., Yoshikawa, A., Nikl, M., Kamada, K., Fukuda, T., **2006**. *Scintillation characteristics of Pr-doped $Lu_3Al_5O_{12}$ single crystals*. J. Cryst. Growth 292, 239 – 242.

Ogino, H., Yoshikawa, A., Nikl, M., Kucerkova, R., Shimoyama, J.-I., Kishio, K., **2009**. *Suppression of defect related host luminescence in LuAG single crystals*. Phys. Procedia 2, 191-205.

Omanović-Mikličanin, E., Badnjević, A., Kazlagić, A., Hajlovac, M., **2020**. *Nanocomposites: a brief review.* Health Technol. 10, 51 – 59.

Pepin, C.M., Bérard, P., Perrot, A.-L., Houde, D., Lecomte, R., Melcher, C.L., Dautet, H., **2004**. *Properties of LYSO and recent LSO scintillators for phoswich PET detectors*. IEEE Trans. Nucl. Sci. 51 (3), 769 – 795.

Peterson, D.S., **2014**. *Sol-gel technique*. Encyclopedia of microfluidics and nanofluidics. Springer, Boston, USA.

Pierce, M., Reiners, J.J., Santiago, A.M., Kessel, D., **2009**. *Monitoring singlet oxygen and hydroxyl radical formation with fluorescent probes during photodynamic therapy.* Photochem. Photobiol. 85, 1177 – 1181.

Polisadova, E., Valiev, D., Vaganov, V., Oleshko, V., Han, T., Zhang, C., Burachenko, A., Popov, A.I., **2019**. *Time-resolved cathodoluminescence spectroscopy of YAG and YAG:Ce^{3+} phosphors*. Opt. Mater. 96, Art. No. 109289.

Pop, S.F., Ion, R.M., Corobea, M.C., Raditoiu, V., **2013**. *Spectral and thermal investigations of porphyrin and phthalocyanine nanomaterials*. J. Optoelectron. Adv. Mater. 13 (7), 906 – 911.

Popovich, K., Procházková, L., Pelikánová, I.T., Vlk, M., Palkovský, M., Jarý, V., Nikl, M., Múčka, V., Mihóková, E., Čuba, V., **2016**. *Preliminary study on singlet oxygen production using $CeF_3:Tb^{3+}@SiO_2$-PpIX*. Radiat. Meas. 90, 325 – 328.

Prior,D.J., Boyle, A.P., Brenker, F., Cheadle, M.C., Day, A., Lopez, G., Peruzzo, L., Potts, G.J., Reddy, S., Spiess, R., Timms, N.E., Trimby, P., Wheeler, J., Zetterström, L., **1999**. *The application of electron backscatter diffraction and orientation contrast imaging in the SEM to textural problems in rocks.* Amer. Miner. 84, 1741 – 1759.

Procházková, L., **2018**. *Nanocomposite scintillators based on zinc oxide with band gap modulation.* Ph.D. dissertation, Czech Technical University in Prague, Czech Republic.

Procházková, L., Vaněček, V., Čuba, V., Pjatkan, R., Martinez-Turtos, R., Jakubec, I., Buryi, M., Omelkov, S., Auffray, E., Lecoq, P., Mihóková, E., Nikl, M., **2019**. *Core–shell ZnO:Ga-SiO_2 nanocrystals: limiting particle agglomeration and increasing luminescence via surface defect passivation.* RSC Adv. 9, 28946 – 28952.

Pucci, A., Boccia, M., Galembeck, F., de Paula Leite, C.A., Tirelli, N., Ruggeri, G., **2008**. *Luminescent nanocomposites containing CdS nanoparticles dispersed into vinyl alcohol based polymers*. React. Funct. Polym. 68 (7), 1144 – 1151.

Qiao, J., Zhao, J., Liu, Q., Xia, Z., **2019**. *Recent advances in solid-state LED phosphors with thermally stable luminescence.* J. Rare Earths 37 (6), 565 – 572.

Quang, A.Q.L., Hierle, R., Zyss, J., Ledoux, I., Gusmai, G., Costa, R., Barberis, A., Pietralunga, S.M., **2006**. *Demonstration of net gain at 1550 nm in an erbium-doped polymer single mode rib waveguide.* Appl. Phys. Lett. 89, Art. No. 141124.

Raevskaya, A.E., Panasiuk, Y.V., Stroyuk, O.L., Kuchmiy, S.Y., Dzhagan, V.M., Milekhin, A.G., Yeryukov, N.A., Svechnikova, L.A., Rodyakina, E.E., Plyushin, V.F., Zahn, D.R.T., **2014**. *Spectral and luminescent properties of ZnO-SiO_2 core-shell nanoparticles with size-selected ZnO cores.* RSC Adv. 4, 63393 – 63401.

Refit, P., Pinel, S., Toussaint, M., Frochot, C., Chouikrat, R., Bastogne, T., Barberi-Heyob, M., **2015**. *Nanoparticles for radiation therapy enhancement: the key parameters.* Theranostics 5 (9), 1030 – 1044.

Roduner, E., **2006**. *Size matters: why nanomaterials are different*. Chem. Soc. Rev. 35, 583 – 592.

Sadasivam, M., Avci, P., Gupta, G.K., Lakshmanan, S., Chandran, R., Huang, Y.-Y., Kumar, R., Hamblin, M.R., **2013**. *Self-assembled liposomal nanoparticles in photodynamic therapy*. Eur. J. Nanomed 5 (3), 115 – 129.

Sahi, S., Chen, W., **2013**. *Luminescence enhancement in CeF_3/ZnO nanocomposites for radiation detection.* Radiat. Meas. 59, 139 – 143.

Sahi, S., Magill, S., Ma, L., Xie, J., Chen, W., Jones, B., Nygren, D., **2018**. *Wavelength-shifting properties of luminescence nanoparticles for high energy particle detection and specific physics process observation*. Sci. Rep. 8 (1), 1 – 9.

Salata, O.V., **2004**. *Applications of nanoparticles in biology and medicine*. J. Nanobiotechnol. 2 (1), Art. No. 3.

Saravanan, R., **2016**. *Nano semiconducting materials.* Materials Research Foundations, vol. 3. Materials Research Forum LLC, Millersville, USA.

Schäferling, M., **2012**. *The art of fluorescence imaging with chemical sensors.* Angew Chem. Int. Ed. Engl. 51 (15), 3532 – 3554.

Schneider, C.A., Rasband, W.S., Elicieri, K.W., **2012**. *NIH image to ImageJ: 25 years of image analysis*. Nature Methods 9 (7), 671 – 675.

Sen, S., Tyagi, M., Sharma, K., Sarkar, P.S., Sarkar, S., Basak, C.B., Pilate, S., Ghosh, M., Gadkari, S.C., **2017**. *Organic-Inorganic Composite Films Based on $Gd_3Ga_3Al_2O_{12}$:Ce Scintillator Nanoparticles for X-ray Imaging Applications*. ACS Appl. Mater. Interfaces 9 (42), 37310 – 37320.

Siegel, R.W., **1993**. *Synthesis and processing of nanostructured materials*, in: Nastasi, M., Parkin, D.M., Gleiter, H. (Eds.), Mechanical Properties and Deformation Behavior of Materials Having Ultra-Fine Microstructures. NATO ASI Series (Series E: Applied Sciences), vol. 233. Springer, Dordrecht.

Silva, F.R.O., Bellini, M.H., Tristao, V.R., Schor, N., Vieira, N.D., Courrol, L.C., **2010**. *Intrinsic fluorescence of protoporphyrin IX from blood samples can yield information on the growth of prostate tumors*. J. Fluoresc. 20 (6), 1159 – 1165.

Son, Y., Yeo, J., Moon, H., Woo Lim, T., Hong, S., Hyun Nam, K., Yoo, S., Grigoropoulos, C.P., Yang, D.-Y., Hwan Ko, S., **2011**. *Nanoscale electronics: digital fabrication by direct femtosecond laser processing of metal nanoparticles*. Adv. Mater. 28 (28), 3176 – 3181.

Steel, A., Carr, S.W., Anderson, M.W., **1995**. *^{29}Si solid-state NMR study of mesoporous M41S materials*. Chem. Mater. 7 (10), 1829 – 1832.

Sugiyama, M., Fujimoto, Y., Yanagida, T., Yokota, Y., Pejchal, J., Furuya, Y., Tanaka, H., Yoshikawa, A., **2011**. *Crystal growth and scintillation properties of Nd-doped $Lu_3Al_5O_{12}$ single crystals with different Nd concentrations*. Opt. Mater. 33, 905 – 908.

Skovsen, E., Snyder, J.W., Lambert, J.D.C., Ogilby, P.R.J., **2005**. *Lifetime and diffusion of singlet oxygen in a cell.* J. Phys. Chem. B 109 (18), 8570 – 8573.

Sperling, R.A., Parak, W.J., **2010**. *Surface modification, functionalization and bioconjugation of colloidal inorganic nanoparticles*. Philos. Trans. Roy. Soc. A 368 (1915), 1333 – 1383.

Stange, S., Esch, E.I., Bacrania, M.K., Brown, L.O., Couture, A.J., Del Sesto, R.E., Golbertson, R.D., Jacobsohn, L.G., Mark McCleskey, T., McKigney, E.A., Muenchausen, R.E., Reifarth, R., **2008**. *Development and characterization of nanocomposite scintillators for gamma-ray detection.* 2008 IEEE Nuclear Science Symposium Conference Record, 3529 – 3532.

Sun, W., Zhou, Z., Pratx, G., Chen, X., Chen, H., **2020**. *Nanoscintillator-mediated X-ray induced photodynamic therapy for deep-seated tumors: from concept to biomedical applications.* Theranostics 10 (3), 1296 – 1318.

Tan, T.T.Y., **2012**. *Rare earth nanotechnology*. Pan Stanford Publishing Pte. Ltd., Singapore, Republic of Singapore.

Thierry, B., Zimmer, L., McNiven, S., Finnie, K., Barbé, C., Griesser, H.J., **2008**. *Electrostatic self-assembly of PEG co-polymers onto porous silica nanoparticles*. Langmuir 24 (15), 8143 – 8150.

Tostado-Plascencia, M.M., Sanchez-Tizapa, M., Zamudio-Ojeda, A., Suárez-Gómez, A., Castañeda-Valderrama, R., Carreón-Alvarez, M.A., Morán-Lázaro, J.P., Joseph-Sebastian, P., Salgado-Transito, I., **2016**. *Synthesis and characterization of multiwalled carbonnanotubes-protoporphyrin IX composites using acid functionalized ornitrogen doped carbon nanotubes.* Diam. Relat. Mater. 70, 65 – 75.

Trequesser, Q.L., Seznec, H., Delville, M.-H., **2013**. *Functionalized materials: Their use as contrast agents in bioimaging: Mono- and multimodal approaches.* Nanotechnol. Rev. 2 (2), 125 – 169.

Uhlich, D., Huppertz, P., Wiechert, D.U., Jüstel, T., **2007**. *Preparation and characterization of nanoscale lutetium aluminium garnet (LuAG) powders doped by* Eu^{3+}. Opt. Mater. 29 (11), 1505 – 1509.

Vollath, D., Szabó, D.V., **1999**. *Coated nanoparticles: A new way to improved nanocomposites.* J. Nanopart. Res. 1, 235 – 242.

Vondrášková, A., Bárta, J., Beitlerová, A., Jarý, V., Čuba, V., Nikl, M., **2016**. *Pr-doped* $Lu_3Al_5O_{12}$ *scintillation nanopowders prepared by radiation method*. J. Lumin. 179, 21 – 25.

Wang, J.-G., Tian, S.-J., Li, G.-B., Liao, F.-H., Jing, X.-P., **2001**. *Preparation and x-ray characterization of low-temperature phases of* R_2SiO_5 *(R = rare earth elements)*. Mater. Res. Bull. 36, 1855 – 1861.

Wang, S.F., Lv, H.B., Zhou, X.S., Fu, Y.Q., Zu, X.T., **2014**. *Magnetic nanocomposites through polyacrylamide gel route.* Nanosci. Nanotech. Let. 6 (9), 758 – 771.

Wang, Y., Rhodes, W.H., Baldoni, G., van Loef, E., Glodo, J., Brecher, C., Nguyen, L., Shah, K.S., **2009**. *Lu_2SiO_5:Ce optical ceramic scintillator*. Proc. SPIE 7393, Art. No. 73930H.

Wang, Z.L., Quan, Z.W., Jia, P.Y., Lin, C.K., Luo, Y., Chen, Y., Fang, J., Zhou, W., O'Connor, C.J., Lin, J., **2006**. *A facile synthesis and photoluminescent properties of redispersible CeF_3, $CeF_3:Tb^{3+}$, and $CeF_3:Tb^{3+}/LaF_3$ (core/shell) nanoparticles*. Chem. Mater. 18 (8), 2030-2037.

Weishaupt, K.R., Gomer, C.J., Doughertz, T.J., **1976**. *Identification of singlet oxygen as cytotoxic agent in photo-inactivation of a murine tumor.* Cancer Res. 36 (7), 2326 – 2329.

Wilhelm, S., Hirsch, T., Patterson, W.M., Scheucher, E., Mayr, T., Wolfbeis, O.S., **2013**. *Multicolor upconversion nanoparticles for protein conjugation*. Theranostics 3 (4), 239-248.

Wilson,K.J., Alabd, R., Abolhasan, M., Safavi-Naeini, M., Franklin, D.R., **2020**. *Optimisation of monolithic nanocomposite and transparent ceramic scintillation detectors for positron emission tomography*. Sci. Rep. 10, Art. No. 1409.

Wright, J.D., Sommerdijk, N.A.J.M., **2001**. *Sol-gel materials: chemistry and applications*. CRC Press, Boca Raton, USA.

Wu, Y.T., Zhang, G.Q., Ren, G.H., **2014**. *Band-gap engineering in $Lu_3Al_5O_{12}$:Pr by Sc^{3+} or In^{3+} substitution.* J. Lumin. 145 (1), 371 – 378.

Xing, L., Wang, C., Wang, X., Ding, X., **2018**. *One-step synthesis and characterisation of LuAG nanoparticles via solvothermal route.* Micro Nano Lett. 13 (3), 411 – 414.

Xu, J., Shi, Y., Xie, Lei, F., **2013**. *Fabrication, microstructure, and luminescent properties of Ce^{3+} -doped $Lu_3Al_5O_{12}$ (Ce:LuAG) transparent ceramics by low-temperature vacuum sintering*. J. Am. Ceram. Soc. 96 (6), 1930-1936.

Yefimova, S.L., Tkacheva, T.N., Maksimchuk, P.O., Bespalova, I.I., Hubenko, K.O., Klochkov, V.K., Sorokin, A.V., Malyukin, Y.V., **2017**. *$GdVO_4:Eu^{3+}$ nanoparticles – Methylene Blue complexes for PDT: electronic excitation energy transfer study*. J. Lumin. 192, 975 – 981.

Yun, P., Shi, Y., Zhou, D., Xie, J., **2009**. *Hydrothermal synthesis of Ce:Lu_2SiO_5 scintillator powders*. J. Rare Earth. 27 (5), 801 – 805.

Zhang, H., Aharonovich, I., Glenn, D.R., Schalek, R., Magyar, A.P., Lichtman, J.W., Hu, E.L., Walsworth, R.L., **2014**. *Silicon-vacancy color centers in nanodiamonds: cathodoluminescence imaging markers in the near infrared*. Small 10 (10), 1908 – 1913.

Zhao, W.R., Gu, J.L., Zhang, X., Chen, H.R., Shi, J.L., **2005**. *Fabrication of uniform magnetic nanocomposite spheres with a magnetic core/mesoporous silica shell structure.* J. Am. Chem. Soc. 127 (25), 8916 – 8917.

Zorenko, Y., Gorbenko, V., Savchyn, V., Zorenko, T., Grinyov, B., Sidletskiy, O., Fedorov, A., Mares, J.A., Nikl, M., Kucera, M., **2013**. *Lu_2SiO_5:Ce and Y_2SiO_5:Ce single crystals and single crystalline film scintillators: comparison of the luminescent and scintillation properties.* Radiat. Meas. 56, 84 – 89.

List of Publications

Publications in journals with impact factor

Popovich, K., Procházková, L., Pelikánová, I.T., Vlk, M., Palkovský, M., Jarý, V., Nikl, M., Múčka, V., Mihóokvá, E., Čuba, V., **2016**. *Preliminary study on singlet oxygen production using CeF_3:Tb^{3+}@SiO_2-PpIX*. Radiat. Meas. 90, 325 – 328.

Popovich, K., Tomanová, K., Čuba, V., Procházková, L., Pelikánová, I.T., Jakubec, I., Mihóková, E., Nikl, M., **2018**. *LuAG:Pr^{3+}-porphyrin based nanohybrid system for singlet oxygen production: Toward the next generation of PDTX drugs.* J. Photochem. Photobiol. B, 179, 149 – 155.

Mihóková, E., Babin, V., Pejchal, J., Čuba, V., Bárta, J., Popovich, K., Schulman, L.S., Yoshikawa, A., Nikl, M., **2018**. *Afterglow and quantum tunneling in Ce-doped lutetium aluminum garnet.* IEEE Trans. Nucl. Sci. 65 (8), 2085 – 2089.

Fišera, O., Kareš, J., Procházková, L., Popovich, K., Bárta, J., Čuba, V., **2018**. *Sorption properties of selected oxidic nanoparticles for the treatment of spent decontamination solutions based on citric acid*. J. Radioanal. Nucl. Chem. 318 (3), 2443 – 2448.

Popovich, K., Šípková, M., Čuba, V., Procházková, L., Bárta, J., Nikl, M., **2019**. *Highly luminescent cerium-doped YSO/ LSO microcrystals prepared via room temperature sol-gel route*. Radiat. Meas. 122, 84 – 90.

Popovich, K., Klepárník, K., Ledvina, V., Neužilová, B., Fleišmann, J., Škodová, M., Kobera, L., Mihóková, E., Múčka, V., Čuba, V., **2020**. *Luminescent nanocomposites for biomedical applications*. IEEE Trans. Nucl. Sci. 67 (6), 962 – 968.

Applied results

Procházková, L., Čuba, V., Bárta, J., Pavelková, T., Popovich, K., **2015**. Functional sample: *NiO-based sorbent prepared using UV light.*

Bárta, J., Čuba, V., Pavelková, T., Procházková, L., Popovich, K., **2015**. Functional sample: *Yttrium aluminium garnet (YAG) luminophore host matrix prepared using UV light.*

Čuba, V., Bárta, J., Procházková, L., Popovich, K., **2016**. Functional sample: *Experimental construction of photochemical pilot plant.*

Čuba, V., Bárta, J., Popovich, K., Procházková, L., **2017**. Functional sample: *Inorganic powder scintillator for LSC.*

Popovich, K., Čuba, V., Bárta, J., Procházková, L., **2018**. Utility Model CZ 31858: *An automated device for the continuous photochemical preparation of nanoparticles of metals or metal oxides from aqueous solutions.*